Research Square

Preprints are preliminary reports that have not undergone peer review.
They should not be considered conclusive, used to inform clinical practice,
or referenced by the media as validated information.

Dual-Stage Artificial Neural Network (Ann) Model for Sequential Lbmm-µedm Based Micro Drilling

Wazed Ibne Noor
International Islamic University Malaysia
Tanveer Saleh (tanveers@iium.edu.my)
International Islamic University Malaysia https://orcid.org/0000-0002-9606-2323
Mir Akmam Noor Rashid
International Islamic University Malaysia
Azhar Bin Mohd Ibrahim
International Islamic University Malaysia
Mohamed Sultan Mohamed Ali
Universiti Teknologi Malaysia - Main Campus Skudai: Universiti Teknologi Malaysia

Research Article

Keywords: Artificial Neural Network, Laser, µEDM, micromachining, Sequential

Posted Date: April 7th, 2021

DOI: https://doi.org/10.21203/rs.3.rs-385339/v1

License: This work is licensed under a Creative Commons Attribution 4.0 International License.
Read Full License

DUAL-STAGE ARTIFICIAL NEURAL NETWORK (ANN) MODEL FOR SEQUENTIAL LBMM-μEDM BASED MICRO DRILLING

Wazed Ibne Noor[1], Tanveer Saleh[1]*, Mir Akmam Noor Rashid[1], Azhar Bin Mohd Ibrahim[2], Mohamed Sultan Mohamed Ali[3]

[1] Autonomous Systems and Robotics Research Unit (ASRRU), Department of Mechatronics Engineering, International Islamic University Malaysia, Kuala Lumpur, 53100, Malaysia

[2] Department of Mechatronics Engineering, International Islamic University Malaysia, Kuala Lumpur, 53100, Malaysia

[3] School of Electrical Engineering, Universiti Teknologi Malaysia, 81310 UTM Johor Bahru, Johor, Malaysia

* E-mail: tanveers@iium.edu.my

Abstract

A sequential process combining laser beam micromachining(LBMM) and micro electro-discharge machining (μEDM) for the micro-drilling purpose was developed to incorporate both methods' benefits. In this sequential process, a guiding hole is produced through LBMM first, followed by μEDM applied to that same hole for more fine machining. This process facilitates a more stable, efficient machining regime with faster processing (compared to pure μEDM) and much better hole quality (compared to LBMMed holes). Studies suggest that strong correlations exist between the various input and output parameters of the sequential process. However, a mathematical model that maps and simultaneously predicts all these output parameters from the input parameters is yet to be developed. Our experimental study observed that the μEDM finishing operation's various output parameters are influenced by the morphological condition of the LBMMed holes. Hence, an artificial neural network(ANN) based dual-stage modelling method was developed to predict the sequential process's outputs. The first stage of the dual-stage model was utilized to predict various LBMM process outputs from different laser input parameters. Furthermore, in the second stage, LBMM predicted outputs (such as pilot hole entry area, exit area, recast layer, and heat affected zone) were used for the final prediction of the sequential process outputs (i.e. machining time by μEDM, machining stability during μEDM in terms of short circuit count and tool wear during μEDM). The model was evaluated based on the average RMSE (Root Mean Square Errors) values for the individual output parameters' complete set data, i.e. μEDM time, short circuit count and tool wear. The values of Average RMSE for the parameters as mentioned earlier were found to be 0.1272(87.28% accuracy), 0.1085(89.15% accuracy), 0.097 (90.3% accuracy), respectively.

Keywords: Artificial Neural Network, Laser, μEDM, micromachining, Sequential

Introduction

Micromachining refers to one kind of fabrication methods of micro parts with intricate shapes and features, whose dimensions often fall between 1μm to 500μm [1]. It is generally defined as a subtractive process that can accurately produce minuscule size parts, which is difficult to accomplish via traditional methods. The accuracy achieved by the most precise machining method is as low as 0.0003 μm [2]. Micromachining technologies have drawn significant interest from the researchers due to the massive demands of ultra-precise and miniatured products in various sectors. The emergence of materials and metamaterials with unique properties has opened a new frontier of possibilities in micromachining. Conventional micromachining processes cannot offer the solution for some of the modern materials such as different nitroalloy, hastalloy, nimonics, carbides, heat resistant steel, wasp-alloy, etc. due to the level of difficulties associated with machining of these materials [2]. Hence, non-conventional machining processes provide the solution for machining difficult to cut materials [2].

Laser beam micromachining (LBMM) and micro electro-discharge machining (μ-EDM) are both non-conventional, contactless machining process. LBMM removes material through a focused laser beam which melts and vaporizes the material selectively as heated by the laser spot. This phenomenon of simultaneous melting and vaporization is called laser ablation [3]. LBMM offers ultra-fast machining of holes, but it produces a high heat-affected zone(HAZ) and recast layer surrounding the resultant holes [4]. HAZ and recast layer are undesirable surface properties that need to be removed for the sake of quality. Although ultrashort laser technology helps produce micro-holes with acceptable accuracy and structural integrity [5]; yet one of the bottlenecks of ultrashort laser technology is its very high initial cost [6]. Moreover, the ultrashort laser is mainly applicable for thinner workpiece with a range of less than 250 μm of thickness [6]. The various laser input parameters, such as scanning speed and laser power, affect the LBMM process's output [7]. Several studies have been conducted to investigate and model the relationships between the inputs and outputs of the LBMM process. The modelling approach for the LBMM process consists of both analytical and empirical. Teixidor et al.[8] developed an analytical model for predicting the depth of micro-channels formed by nanosecond laser micromachining process on polymethylmethacrylate (PMMA) polymer. Yang et al.[9] formulated a three-dimensional finite element model (FEM) to predict and compare the HAZ depth and width in the Ti6Al4V alloy workpiece produced during the LBMM process. Response surface methodology(RSM) based empirical modelling was used for predicting mark width, mark depth and mark intensity for pulsed Nd: YAG laser marking process of gallium nitride [10]. Tsai et al.[11] successfully implemented an artificial neural network (ANN) to develop a predictive model for various laser-cutting qualities (diode-pumped solid-state laser), namely the width and depth of the machined line and the width of the HAZ for cutting Quad Flat Non-lead (QFN) package. They also utilized a genetic algorithm for optimizing the output parameters [11]. Vagheesan et al. [12] also applied a neural network and particle swarm optimization (PSO) based modelling and optimization approach for the study of laser cutting (CO_2 laser) of aluminium alloys. Norkey et al. [13] also attempted an ANN-based modelling technique for studying the HAZ for laser machining of aerospace material like duralumin.

Micro electro-discharge machining (μEDM) facilitates frequent electric discharges between a negatively charged electrode and workpiece surface to remove material[14]. The μEDM process removes material much slower than LBMM [15] and suffers from frequent disruption due to short-circuits occurring during machining [16]. Nevertheless, the HAZ and recast layer associated with μEDM is almost insignificant compared to that of LBMM. Various electrical and non-electrical input variables have been found to affect the process outcome of μEDM. Tiwary et al.[17] demonstrated and characterized the effect of various electrical parameters such as pulse on time, peak current, gap voltage and flushing pressure on the material removal rate (MRR), tool wear ratio (TWR), overcut (OC), and taper of μEDM based micromachining of Ti–6Al–4V alloy. Mehfuz et al.[18] discussed the impact of feed rate(non-electrical parameter), capacitance, and voltage on μEDM milling of beryllium-copper alloy. The output parameters investigated in this study [18] were average surface roughness (Ra), maximum peak-to-valley roughness height(Ry), TWR and MRR. The input parameters were found to have significantly impacted the process outputs, both individually and in terms of interaction factors [18]. Yildiz [19] used the finite element modelling technique to predict various output parameters such as recast (white) layer thickness and tool wear for micro electro-discharge machining (μEDM) of copper alloy. D'Urso et al. [20] studied machining time and tool wear for μEDM drilling of stainless steel workpiece using a copper electrode. Authors [20] also used a regression-based modelling technique to formulate a correlation between the input and the output parameters. Nonlinear regression models [20] gave much better accuracy in predicting the experimental findings. It is seen from various studies that standalone or hybrid artificial neural networks (ANN) coupled with genetic algorithm for optimization over multiple objective criteria can accurately model the complex relations between the inputs and outputs of the μEDM process. Ming et al.[21] used multi-variable regression model, backpropagation neural network (BPNN) and a radial basis neural network (RBNN) to predict material removal rate (MRR) and average surface roughness (Ra) for EDMing of SiC/Al composites. The model was further optimized with the genetic algorithm (GA) assistance to find the optimum cutting parameters for the best surface roughness. Kumar et al.[22] studied and optimized electro-discharge machining of titanium alloys using hybrid Taguchi-ANN approach. At first, researchers [22] identified the pertinent input variables for optimizing surface roughness using the Taguchi method and then using those variables, the prediction of Ra was achieved using feed forward backpropagation networks. Suganthi et al.[23] reported the comparison between adaptive neuro-fuzzy inference system (ANFIS) based hybrid model and ANN for prediction of process outcomes such as material removal rate (MRR), average surface roughness (Ra) and tool wear ratio (TWR) for the micro EDM process. ANFIS model exceeded the performance ANN model in terms of prediction accuracy [23]. Abhilash et al. [24] studied the failure of wire-EDM (a variant of EDM) using ANN based classification method. Moghaddam et al. [25] combined ANN and particle swarm optimization (PSO) algorithm to model and optimize the EDM process.

Hybrid machining is a method that combines the effect of two or more standalone machining processes concurrently or sequentially[26]. It aims to synthesize a new technique that combines the individual processes' advantages and negates the undesirable effects[27]. LBMM and μEDM both come with inherent process advantages and disadvantages. To maximize the incentives of both processes, Rashid et al.[28] experimentally evaluated the hybrid micromachining process of sequentially applying LBMM and μEDM. Al-Ahmari et al.[29] reported 50-65% reduced machining time and 40% to 65% increment in material removal rate

(MRR) for the machined holes by their proposed hybrid LBMM-μEDM micro-drilling process. Moreover, the holes were free from adverse effects on the surface as caused by the precursor LBMM [29]. Other researchers also investigated the synergic fusion of LBMM and μEDM experimentally to improve the machining rate significantly without compromising the quality of the machined feature [15, 30].

Both empirical and analytical based modelling techniques have been applied for various types of the hybrid machining process. Pajak et al.[31] studied laser-assisted jet electrochemical machining (LAJECM) and developed an empirical model for predicting volume removal rate (VRR) and taper angle. Bhondwe et al.[32] implemented and validated FEM based model for studying MRR for compound electrochemical spark machining(ECSM). Feng et al.[33] demonstrated that ANOVA analysis could identify the dominant process parameters for laser-waterjet based hybrid micromachining of silicon carbide wafer. They [33] used response surface methodology-based models to describe microgroove depth, width, and MRR for the process mentioned above.

The numerical and analytical models are often problematic in approximating different processes' outcomes when subjected to real-life experimentation. The experimental investigation of the said sequential micromachining (LBMM-μEDM) yielded complex, highly nonlinear relationships that map the inputs to the outputs. As the two different micromachining process are applied sequentially, the quality of the first process has been observed to have affected the overall quality of the combined process. To the authors' best knowledge, no analytical or empirical model has been devised for the laser- μEDM process yet. Sometimes, for a broad range of experimental values and conditions, analytical models fail to capture the governing relationship between input and output data. In contrast, numerical models can be computationally expensive and constrained to the exact value available [34].

Moreover, the artificial neural network-based modelling technique is regarded as a potential soft computing tool for predicting stochastic process like EDM [22, 23, 24], which is one of the machining techniques involved in this research. Therefore, in this paper, we report a dual-stage modelling technique based on an artificial neural network (ANN) for the said LBMM-μEDM micromachining technique. In this phase of our modelling, we did not vary various μEDM parameters during the experimentation; instead, LBMM parameters were varied, and their effects were analyzed for the overall process performance.

Materials and Methods

Preliminary experimental investigation and data analysis were required for the modelling to be carried out for LBMM-μEDM based sequential micromachining process. This section discusses the experimental method that was implemented and subsequently describes the approach to modelling. The experimental method section gives a detailed description of the phases to collect and create the dataset. The modelling section lays out the various steps of the dual-stage modelling procedure and the justification of our approach.

Experimental and Characterization Method

This section focuses heavily on the experimental setup and characterization techniques that have been implemented to collect the data. The micro-holes produced via the sequential micromachining process were examined using scanning electron microscopy (SEM), as discussed at the end of this section.

First, holes with dimensions less than a millimetre were made by LBMM with an intended diameter of 200µm, followed by precise finishing through the application of µEDM. The workpiece material used for this research was stainless steel SS304 with a thickness of 0.2mm. The LBMM micro-drilling was carried out on a 20 W (rated power) desktop fibre laser machine (Ytterbium Doped) that utilizes a pulsed laser with a wavelength and focal length of 1060 nm and 200 mm, respectively. The spot size of the laser was 40µm. The X/Y galvanometer (maximum scan angle ±15°, and resolution 12 µrad) was used to scan the laser beam to engrave the desired patterns on the workpiece. The laser spot scanned the workpiece first horizontally, and then the spot was shifted vertically 10µm to scan horizontally in the opposite direction. The process was continued until the entire intended area was fully scanned. The scanning was repeated according to the loop count as decided during the experimentation. An integrated graphical user interface (GUI) facilitates selecting desired machining parameters of the LBMM setup. For a pre-programmed feature, the parameters that can be varied from the GUI are the laser power, the pulse repetition rate, the scanning speed and the loop count. The range of variation for various LBMM parameter is tabulated in Table 1. However, the detail experimental plan with the parametric variation is attached as supplementary material with this manuscript. After performing the micro-drilling operation using the LBMM process, the workpiece and the fixture were transferred to the µEDM machine (DT110). The translational motion of the µEDM machine is controlled by CNC (computer numerical control) programs. The µEDM machine has positional repeatability of ±1 µm per 100 mm of travelling distance, whereas its programming resolution is 0.1 µm. An RC pulse generator is the primary source of power for the machine's µEDM operation. Table 1 also summarizes the µEDM parameters that were chosen for the experimentation. For this research, various control parameters for µEDM were kept constant, and the scope of the modelling and experimentation for this research is limited to 1-D machining (i.e. drilling) on SS304 workpiece. Further, the programmed diameter of the hole for the LBMM was 200 µm. Therefore, choosing a 500 µm diameter of Tungsten(W) electrode was deemed necessary for the following finishing operation.

In the beginning, an array of micro holes was drilled in a square lattice shape on the workpiece using the LBMM method. The machining time of the holes was recorded simultaneously using the stopwatch with a resolution of 0.01 second. After that, fine finishing was carried out on the µEDM (DT110) machine. Figure 1 shows the LBMM setup alongside the µEDM machine. For precisely situating the tungsten tool above the LBMMed holes, an on-machine measurement (OMM) technique was implemented that comprises a variable lens optical microscope fitted with a high-resolution digital camera. Illustrated in Figure 1, the OMM was positioned close to the µEDM spindle.

Table 1: Various important parameters for LBMM and µEDM process

LBMM process	
Parameter name	Value
Laser spot size (µm)	40
Laser pulse duration (ns)	100
Laser scanning speed (mm/s)	50-1400
Laser average power (%)	15-90
Laser average power (W)	6.4-15.5
Laser pulse repetition rate (kHz)	5-20
µEDM process	
Parameter name	Value
µEDM applied voltage (V)	80
µEDM discharge capacitor (nF)	1
µEDM system's stray capacitance (nF)	0.6
µEDM feed speed (µm/s)	5
µEDM electrode diameter (mm)	0.5
µEDM electrode material	Tungsten (W)

At the start of the µEDM machining, the electrode needs to be positioned on the exact centre of the LBMMed holes. Therefore, a reference hole was machined close to the arrays of the LBMMed holes. The reference hole coordinates were made known using the linear scale feedback of the DT110 µEDM machine. Next, with the OMM's help, the positional deviations (both in X and Y direction) of the reference hole from each of the LBMMed hole on the array were calculated. Lastly, these deviations were added to the reference hole's coordinate to position the tungsten tool right on the LBMMed hole centre. The theoretical positional accuracy of this positioning system is within 2µm. During the µEDM process, the DT110 controller can detect the short circuit (when the electrode touches the workpiece without any discharge [35]) by monitoring the process's electrical characteristics in real-time. A sharp beeping tone was emanated from the machine every time there was an incident of a short circuit that helped us record the number of short circuit occurrences during the whole µEDM process. As the µEDM of each LBMMed hole was completed, the machine recorded the total machining time, which was later used for the analysis. The DT110 machine controller has a function that can be used to automatically detect the conductive surface by touching the electrode with the conductive workpiece. Before starting each µEDM process, the electrode was moved down until it detected the workpiece and the Z coordinate was recorded. The same step was repeated

after the machining process, and the difference between the two Z coordinate was recorded as the vertical tool wear. It is to note that before the start of every μEDM operation, the bottom of the tool was flattened using reverse μEDM [36] to remove any bias during the experimental study.

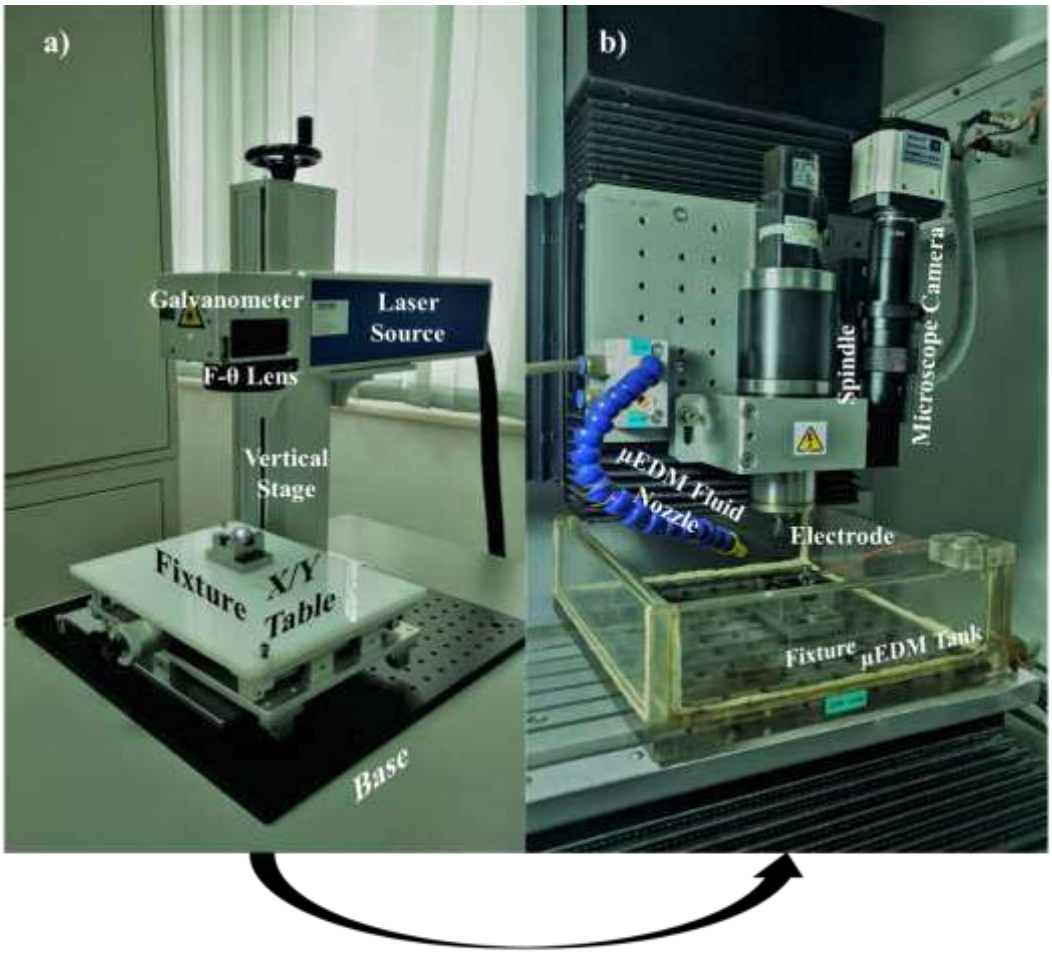

Figure 1: Illustration of the sequential LBMM-μEDM machining setups a) the fibre laser system, and b) the μEDM setup.

The holes' characterization after the LBMM operation was performed with scanning electron microscopy (SEM: JSM-IT100 InTouch Scope™). With all the SEM-generated images being available for measurement, a third-party image analysis software (ImageJ)[37] was utilized for computing the entry area, exit area, HAZ and recast layer associated with each hole as described in Figure 2. The HAZ was measured by subtracting the combination of entry and recast layers' area from the total heat affected zone spanning from the hole's centre.

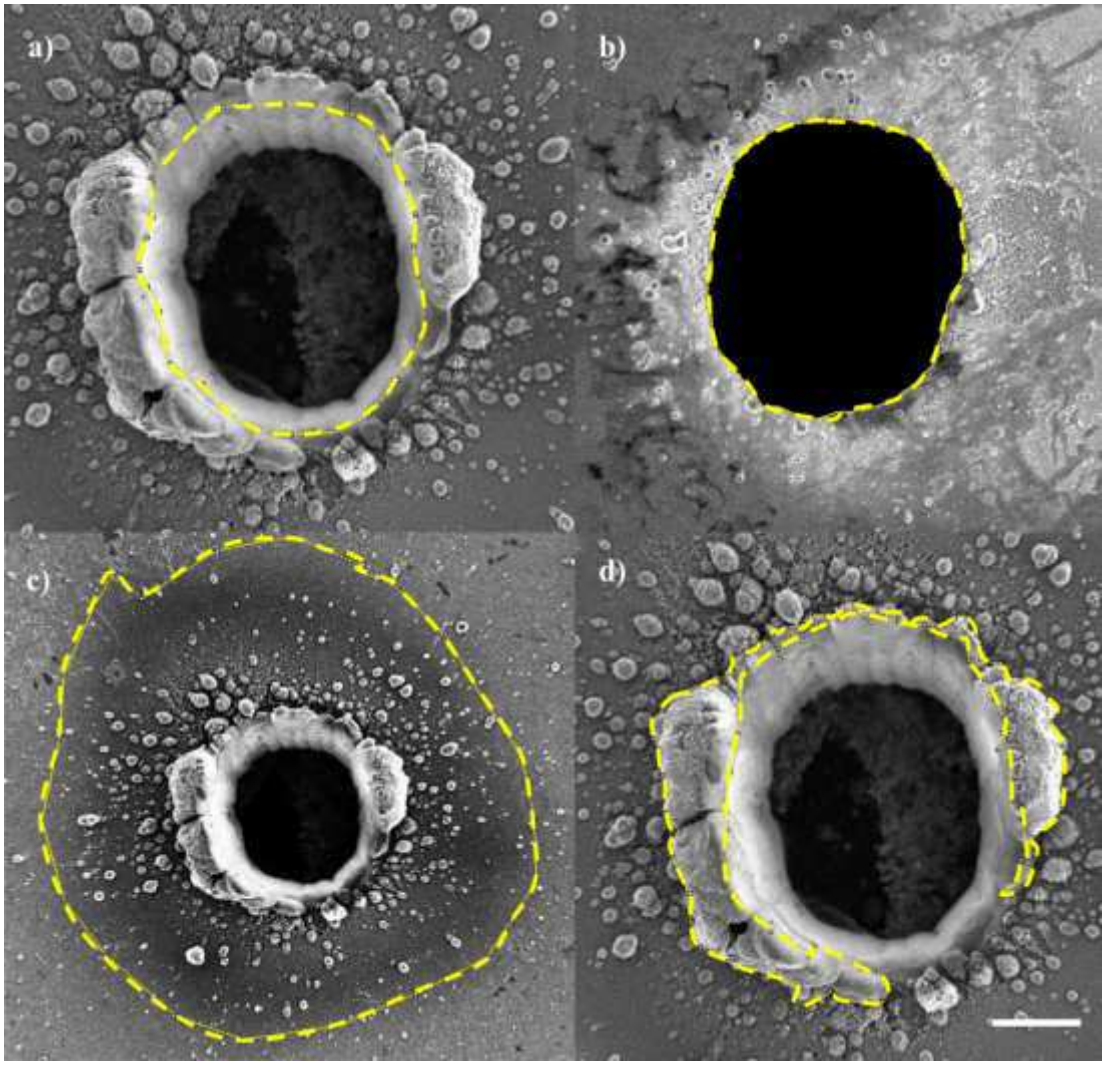

Figure 2: Measurement of LBMMed holes from the SEM images (a) measurement of the entry area, (b) measurement of the exit area, (c) measurement of the recast layer and (d) measurement of the HAZ. Scale bar = 100µm.

Modelling Approach

With the completion of experimentation and characterization, the final dataset containing all the inputs and output parameters of the LBMM-µEDM based sequential micromachining process was prepared. As understood from our literature survey ANNs are widely used in various micromachining related studies because of their efficiency in reducing computational cost with good predictability [22, 34]. Hence, we decided to use an artificial neural network (ANN) model to describe the LBMM-µEDM machining.

From our experimental observation, we noticed that the second stage µEDM finishing operation's performance is remarkably influenced by the output of the LBMM, such as the entry and exit area of the LBMMed hole, etc. Hence, the overall modelling was conducted in two stages; at first, we developed an ANN model to predict various LBMM outputs. A second stage model was subsequently developed, which takes input from the previous stage's prediction and estimates the final µEDM process's various outputs such as machining time, short circuit count, and tool wear. It is to be noted that the µEDM process parameters such as

discharge energy, feed speed etc., were kept constant as the aim of this research to investigate how the LBMM process influences the outcome of the LBMM-µEDM process. Moreover, we found that the LBMM does not influence other µEDM performance indicators such as spark gap and hole taper; hence they were not considered in this modelling process.

The process of machine learning-based modelling such as ANN essentially maps the input and output parameters according to the function that defines the relationship. It is a decent strategy to quantify the correlation between the input and output variables in a high dimensional(n>2) dataset to understand the machining process better. The correlation study will help us select suitable predictors for modelling the LBMM-µEDM process. Hence, Figure 3 shows how various LBMMed holes' characteristics are related to the final finishing process's performance indicators, i.e. µEDM. More intensely coloured blocks of the matrices (Figure 3) denote more substantial correlations between a given pair of variables. Blue and red signify negative and positive correlation, respectively. It can be understood from Figure 3 that the entry/exit area, HAZ and recast layer has a significant influence on the various performance measures of the subsequent µEDM process. The above-stated findings were further verified with the scatter plot, as shown in Figure 4. It is clear from Figure 4(a-l) that the four major quality factors of the LBMM drilling process (entry area, exit area, recast layer and HAZ) have a significant nonlinear and negative correlation with different quality factors of the following µEDM fine drilling process such as machining time, short circuit count and tool wear. Hence, in this modelling approach, we have considered all the four LBMMed holes' characteristics (entry area, exit area, HAZ and recast layer) as the input for our second stage model to predict the various output of the final µEDM process. However, for the first stage model, all possible inputs (LBMM) varied according to Table 1 were considered input during the modelling process (first stage).

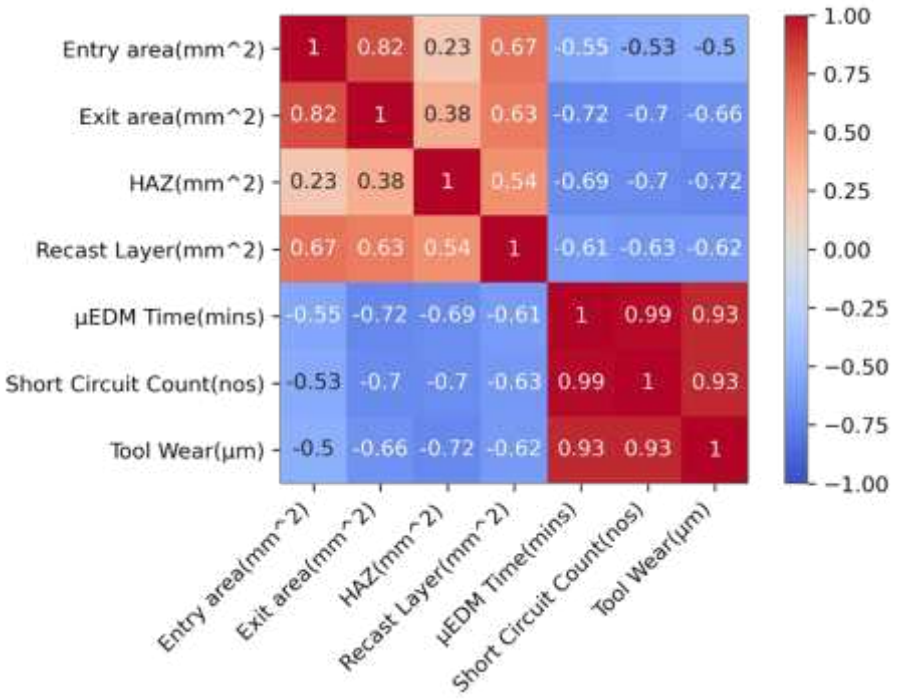

Figure 3: Correlation between various LBMM output and µEDM output.

The procedure of ANN involves learning the function that governs the input-output relationship of the training dataset. The trained model is subsequently asserted on the test dataset in terms of its prediction accuracy. For a robust model, the accuracy or estimation of the model's error is roughly the same for training and test dataset.

Regularization is a technique that adjusts various parameters of the model to ensure that the model does not suffer from overfitting. Bayesian regularized ANN are more advantageous than various other training algorithms as this can eliminate the necessity for a lengthy cross-validation process, yet it can maintain the robustness by getting rid of chances of being overfitted [38]. Considering all factors, we have chosen Bayesian Regularization (BR) training algorithm for training our ANN as we have a limited 119 experimental dataset to build and test the model. The proposed model is a multi-input multi-output (MIMO) that predicts the multiple target variables via a combined model, termed in this paper as "dual-stage ANN model". As mentioned earlier, in this proposed model, LBMM outputs are predicted first from various LBMM inputs at the first stage. In the second stage, various LBMM outputs are fed into the model as inputs to estimate µEDM machining time, short circuit occurrence and tool wear etc.

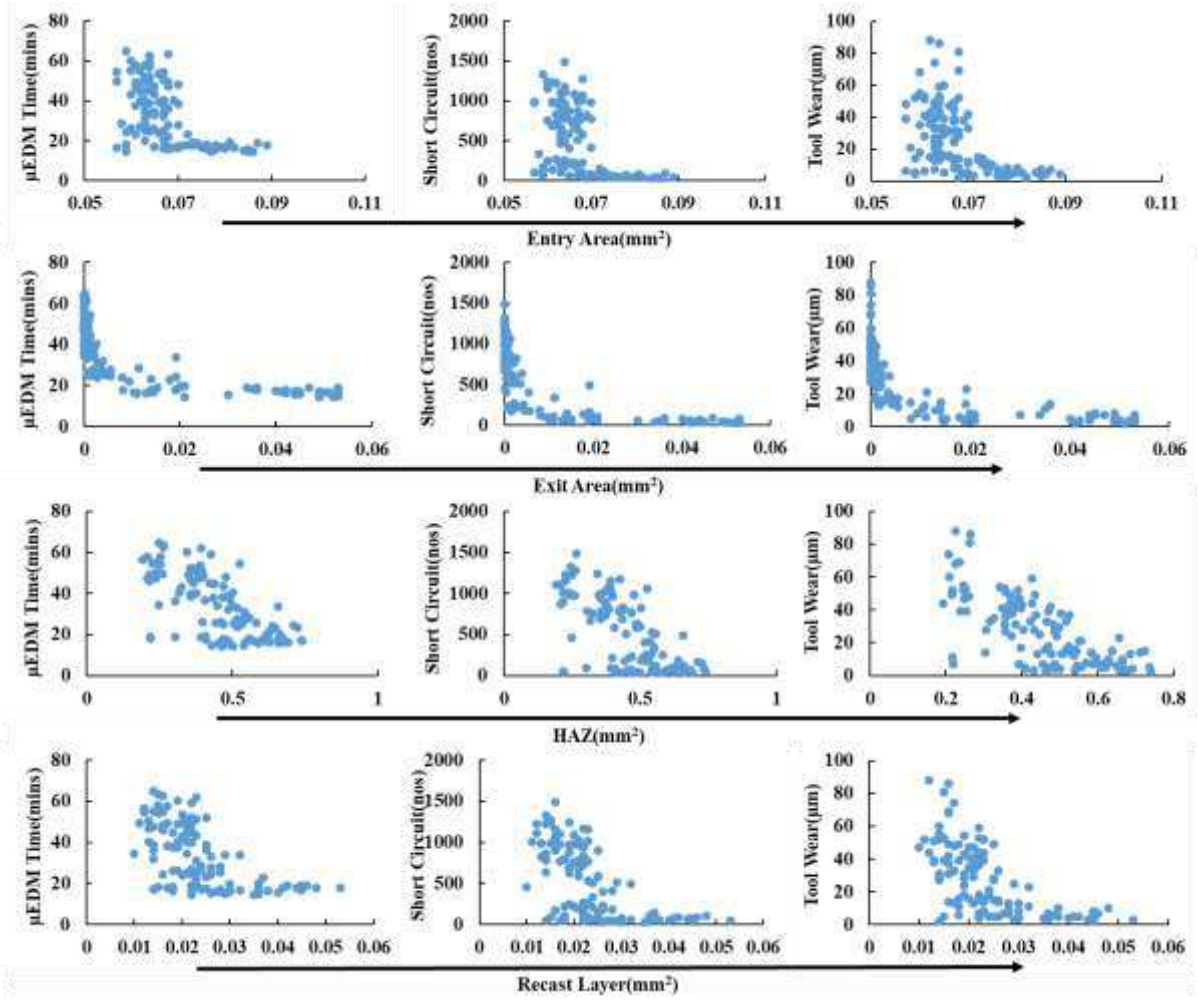

Figure 4: Scatter plot to show the relationship between LBMM output and µEDM output (a) entry area of the LBMMed holes vs µEDM time (b) exit area of the LBMMed holes vs µEDM time (c) HAZ of the LBMMed holes vs µEDM time (d) recast layer of the LBMMed holes vs µEDM time (e) entry area of the LBMMed holes vs short circuit count (f) exit Area of the

LBMMed holes vs short circuit count (g) HAZ of the LBMMed holes vs short circuit count (h) recast layer of the LBMMed hole vs short circuit count (i) entry area of the LBMMed holes vs tool wear (j) exit area of the LBMMed holes vs tool wear (k) HAZ of the LBMMed holes vs tool wear, and (l) recast layer of the LBMMed holes vs tool wear.

The dataset was pre-processed using normalization based on each variable's minimum and maximum value before training the sequential modelling process. The equation below ((1) and (2)) gives the transformation of the raw data to the normalized data.

$$x(i) = \frac{x(i)-\min(x)}{\max(x)-\min(x)} \quad \text{----------(1)}$$

$$y(i) = \frac{y(i)-\min(y)}{\max(y)-\min(y)} \quad \text{----------(2)}$$

The x(i) and y(i) indicate each member of every input and output variables, respectively, for i=1, 2, …… ,119. The terms min(x) and min(y) signify each variable's minimum value. Similarly, the terms max(x) and max(y) indicate each variable's maximum values in the datasets. According to equations (1) and (2), the normalization was carried out for both modelling stages. Further, in the second stage, square-root transformation was applied to the normalized output dataset; namely, normalized values of short circuit count and tool wear to remove the skewness in their distribution. The squared root transformation helped the network to be trained better with higher estimation accuracy. With the dataset fully prepared for modelling, it was split into training and test datasets for both stages of the model. 98 randomly selected data were chosen to be the training set, and the rest 21 were left for evaluating the performance of the model for the unseen data.

Figure 5 illustrates the complete flow and the architecture of the proposed dual-stage sequential model for the LBMM-μEDM process. The model was implemented using MATLAB software. It can be seen from Figure 5 that the first stage of the model (for LBMM) has two layers with 3 and 10 neurons, respectively, in the first and second layer. For the second stage (for μEDM), the number of layers was two with 2 and 5 neurons in the layers. The activation function used in the hidden layers, and the output layer was the sigmoid function and linear function. The option for two layers was selected as we observed from our preliminary training that a network deeper than two layers did not improve the network performance much in terms of prediction accuracy for training and test data set. Next, the hidden layers' size was optimized by iterating the model from 1-1 topology to 20-20 topology. For every combination of hidden layer size, the root mean square error (RMSE) value of each of the predicted variables was computed, and the average RMSE of all variables was calculated for both the training and test dataset. The average RMSE for the training data was decreased with a more complicated (with a high number of neurons) topology. However, the average RMSE for the test dataset was found to have the lowest value for a certain number of neurons in each of the hidden layers selected for deciding the network's topology, as stated above. Using the optimized hidden layer size, the MIMO model was iteratively trained 100 times. During the training, the average RMSE of all the output variables (both for training and the test dataset) was computed and stored in an array. The model was then chosen with a low and similar average RMSE for the train and the test

dataset. Both the stages of ANN modelling applied the strategy mentioned above for selecting the best-fitted model.

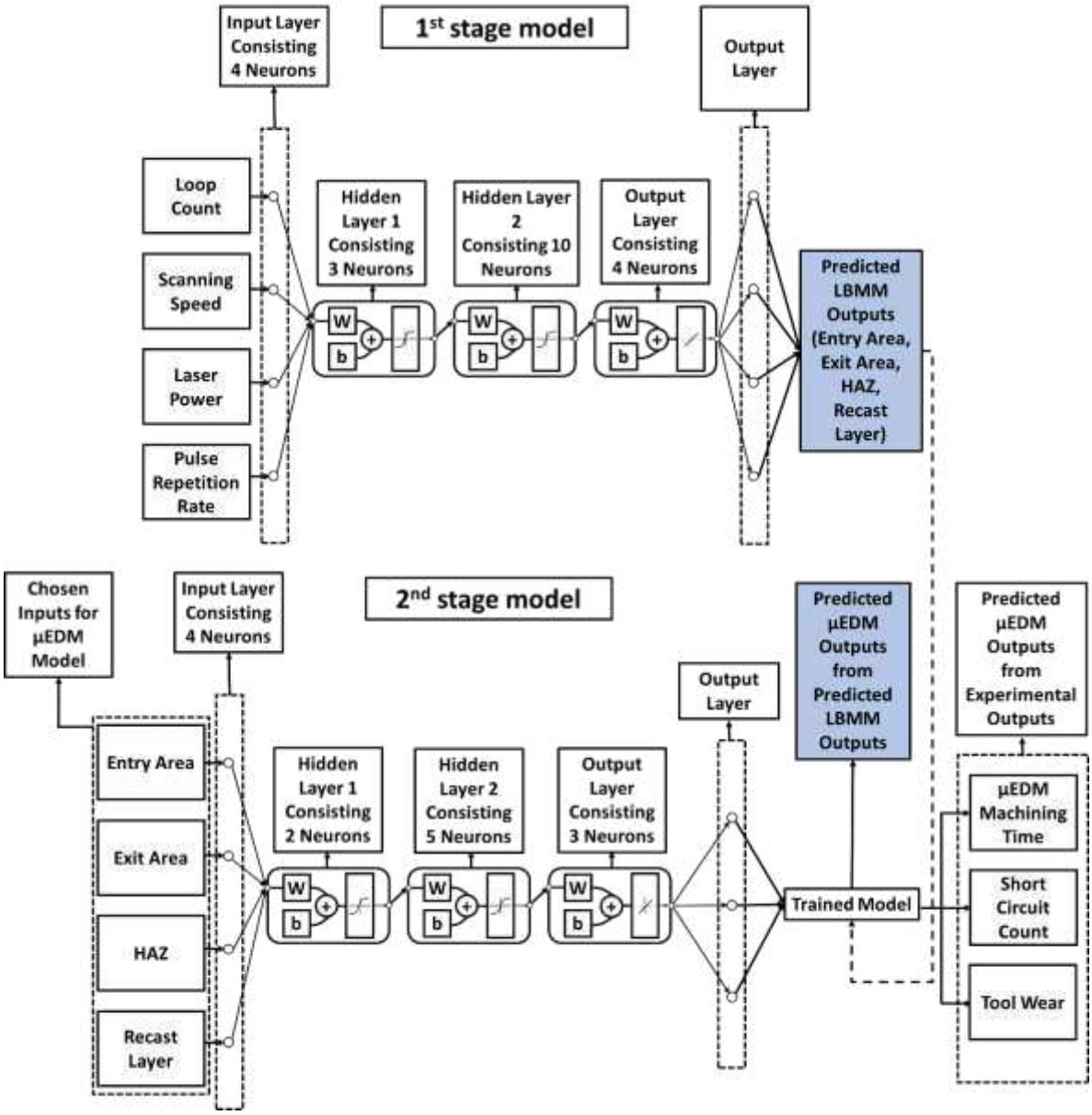

Figure 5: Flow and architecture of the proposed dual-stage ANN model for the LBMM-µEDM process. The dotted line shows that the predicted LBMM output goes as input to the trained second stage model to estimate µEDM outputs, namely µEDM machining time, short circuit count and tool wear.

Results and Discussions

This section focuses on the performance of modelling as well as the interpretation of the results. The validity of the model has been tested and discussed. The predicted outputs' overall trend has been interpreted and discussed to reveal the physics behind the findings.

Modelling Performance

The modelling performance of the dual-stage ANN model has been measured for both stages. The experimental response variables were plotted against the predicted responses. The prediction accuracy of the first stage of the model affects the model's overall accuracy; hence, this section discusses the performance of the individual stages of the model and the holistic performance of the model. The model's performance criterion used in this research is the root mean square error defined by equation (3) and (4).

$$y_{i_{RMSE}} = \frac{\sum_{j=1}^{N}(y_{i_{j_{actual}}} - y_{i_{j_{predicted}}})^2}{N} \text{ ----------(3)}$$

$$N_{RMSE} = \frac{\sum_{i=1}^{n} y_{i_{RMSE}}}{n} \text{ ----------(4)}$$

Here, $y_{i_{RMSE}}$ is the root mean square error for each modelled variable. $y_{i_{j_{actual}}}$ is the experimental output of the i_{th} variable of j_{th} observation. On the other hand $y_{i_{j_{predicted}}}$ is the predicted output (from the developed ANN model) of the i_{th} variable of j_{th} observation. N_{RMSE} is the overall network RMSE as calculated from the arithmetic average of the RMSE of all the variables of interest, and n is the number of variables. The accuracy is defined by equation (5) and (6), where $P_{accuracy_i}$ is the prediction accuracy for the i_{th} variable and $P_{accuracy_N}$ is the overall network accuracy.

$$P_{accuracy_i} = (1 - y_{i_{RMSE}}) \times 100\% \text{ ----------(5)}$$

$$P_{accuracy_N} = (1 - N_{RMSE}) \times 100\% \text{ ----------(6)}$$

The above four equations have been used for both stages of the model. In the first stage, the model's input variable was average laser power, scanning speed, pulse repetition rate, and loop count, whereas the prediction variables were LBMMed holes entry area, exit area, recast layer, and HAZ. Similarly, for the second stage model, the input variables were the outputs of the first stage model, i.e. entry area, exit area, recast layer and HAZ and µEDM time, tool wear and number of short circuits were the final output variables from the proposed dual-stage ANN model.

Study of the performance of the first stage model

In the first stage model, the LBMM input parameters (i.e. loop count, scanning speed, laser power and pulse repetition rate) were used to predict the output parameters at the end using the

most favourable network architecture. The optimum topology of the model for the first stage ANN model was 4-3-10-4. This network had two hidden layers, with the first and second hidden layer having 3 and 10 neurons, respectively. Figure 6 shows the contrast between the actual experimental values and predicted result from the first stage model for all four variables of interest: entry area, exit area, HAZ, and recast layer. It can be inferred from Figure 6 (a-d) that for the case of the exit area, the model prediction fits the most with the experimental output. The individual RMSE values for entry area, exit area, HAZ, and recast layer for the training dataset was 0.0763, 0.0266, 0.0649 and 0.0966, respectively, while for the test set, it was 0.0995, 0.0208, 0.0689 and 0.0721, respectively. Figure 7 summarizes the prediction accuracy of the first stage model for both training and test dataset. Figure 7 also reaffirms that the variable exit area shows better predictability than the other variables (~ 97% for the exit area and ~92% for the remaining variables). The reason for higher predictability for the variable LBMMed holes' exit area could be explained by studying the correlation coefficient between various LBMM input variable and LBMM output parameters as described in Table 2. The LBMMed holes' exit area is highly correlated with most of the LBMM input than the other LBMMed holes' parameters, as seen from Table 2. However, the pulse repetition rate did not show any significant correlation between any of the output parameters of LBMM.

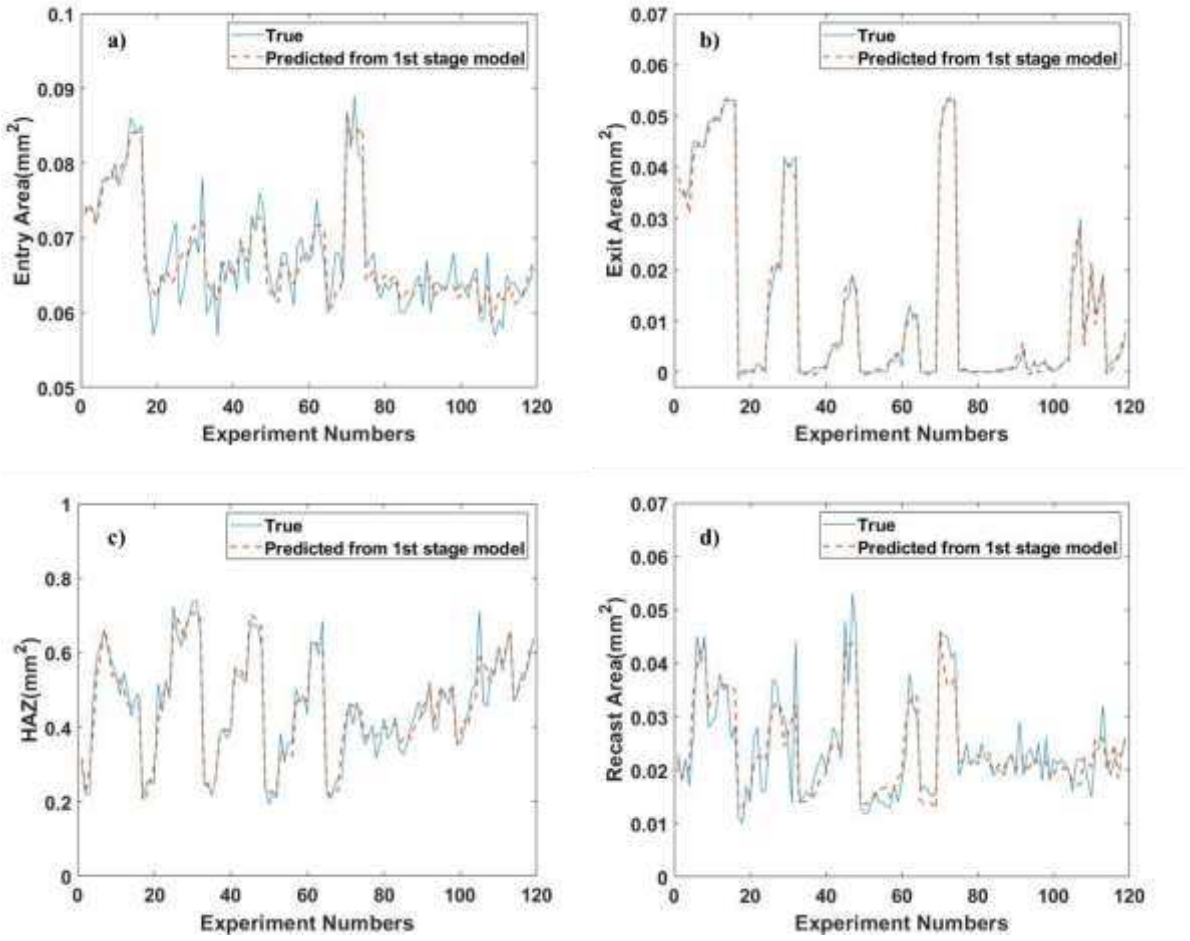

Figure 6: Comparison between the actual output and predicted output for the first stage of the model, (a) Entry Area (b) Exit Area, (c) HAZ and (d) Recast layer.

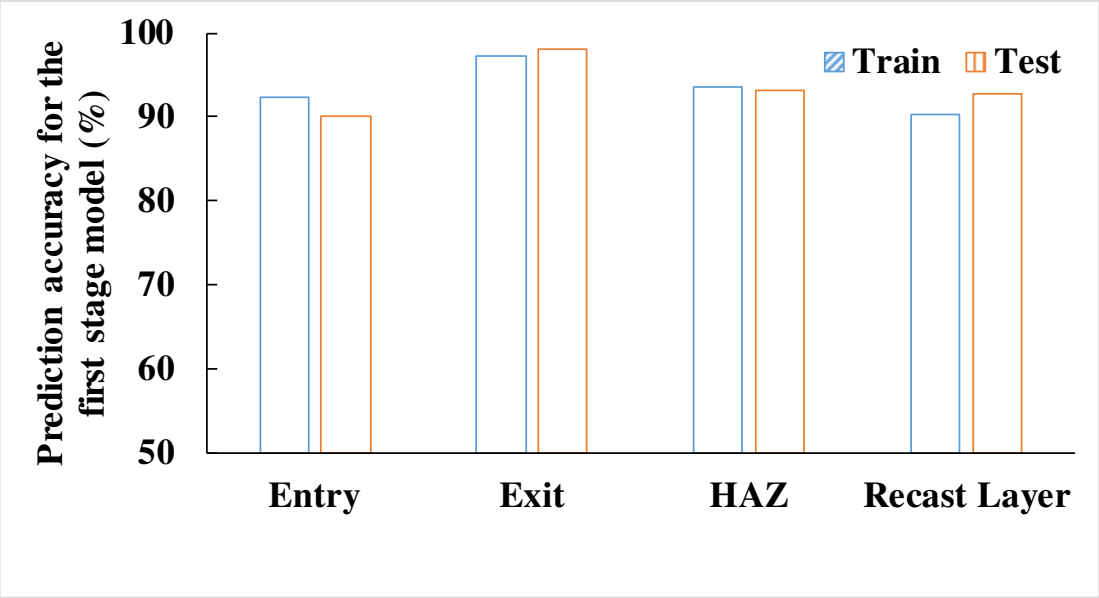

Figure 7: Prediction accuracy of the four variables from the first stage model, namely Entry Area, Exit Area, HAZ and Recast layer.

Table 2: Correlation coefficient between various LBMM inputs and outputs

Correlation Table				
	Output →			
Variable ↓	Entry Area	Exit Area	HAZ	Recast layer
Laser Power	0.83	0.92	0.82	0.71
Scanning Speed	-0.66	-0.86	-0.34	-0.57
Loop Count	-0.09	0.98	0.93	0.09
Pulse repetition rate	-0.13	0.13	-0.14	0.12

Study of the performance of the second stage model

The second stage of the model act as a link to describe how the LBMMed pilot holes' characteristics affect the output parameters of the µEDM method, thereby predicting the final outcome of the LBMM-µEDM based sequential micromachining process. The LBMM output parameters' experimental values (i.e. entry area, exit area, HAZ and recast layer) were used for training the model. The optimum topology of the model after the second stage ANN was 4-2-5-3. This network had two hidden layers, with the first and second hidden layers having 2 and 5 neurons. The individual RMSE values for µEDM machining time, short circuit count, and tool wear for the training dataset was 0.1269, 0.1094 and 0.1001, respectively, while for the

test set, it was 0.0932, 0.0677 and 0.0775, respectively. The corresponding prediction accuracy for each of the variable is shown in Figure 8.

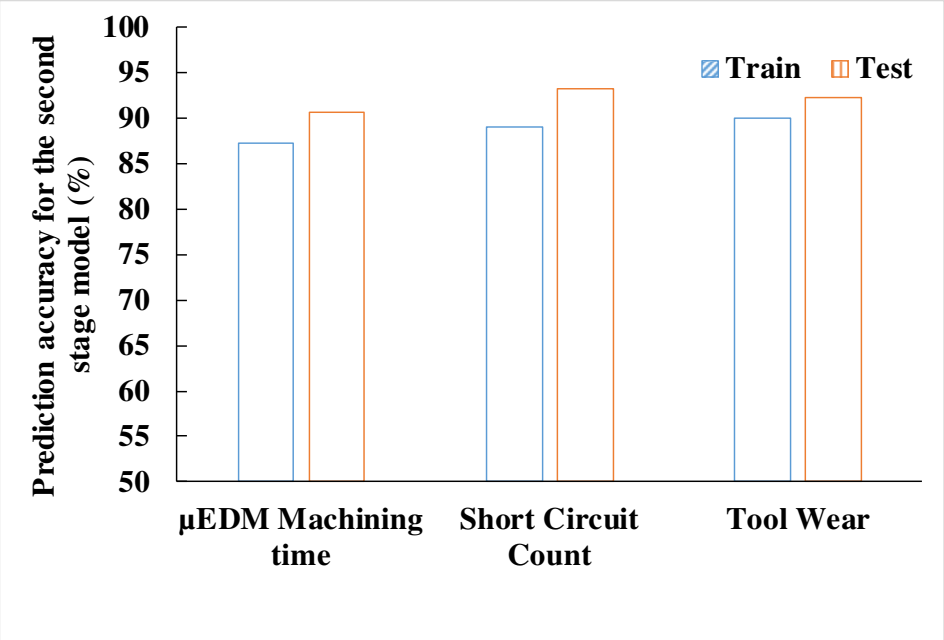

Figure 8: Prediction accuracy of the three variables from the second-stage model, namely µEDM machining time, short circuit count and tool wear.

It can be understood from Figure 8 that the predictability for all the variables is of a similar range (~89% to ~90%). Figure 9 (a-c) compares the actual values of different variables and the predicted ones for the second-stage model, which further confirms that the predictability of all the variables for the second stage model is of comparable range.

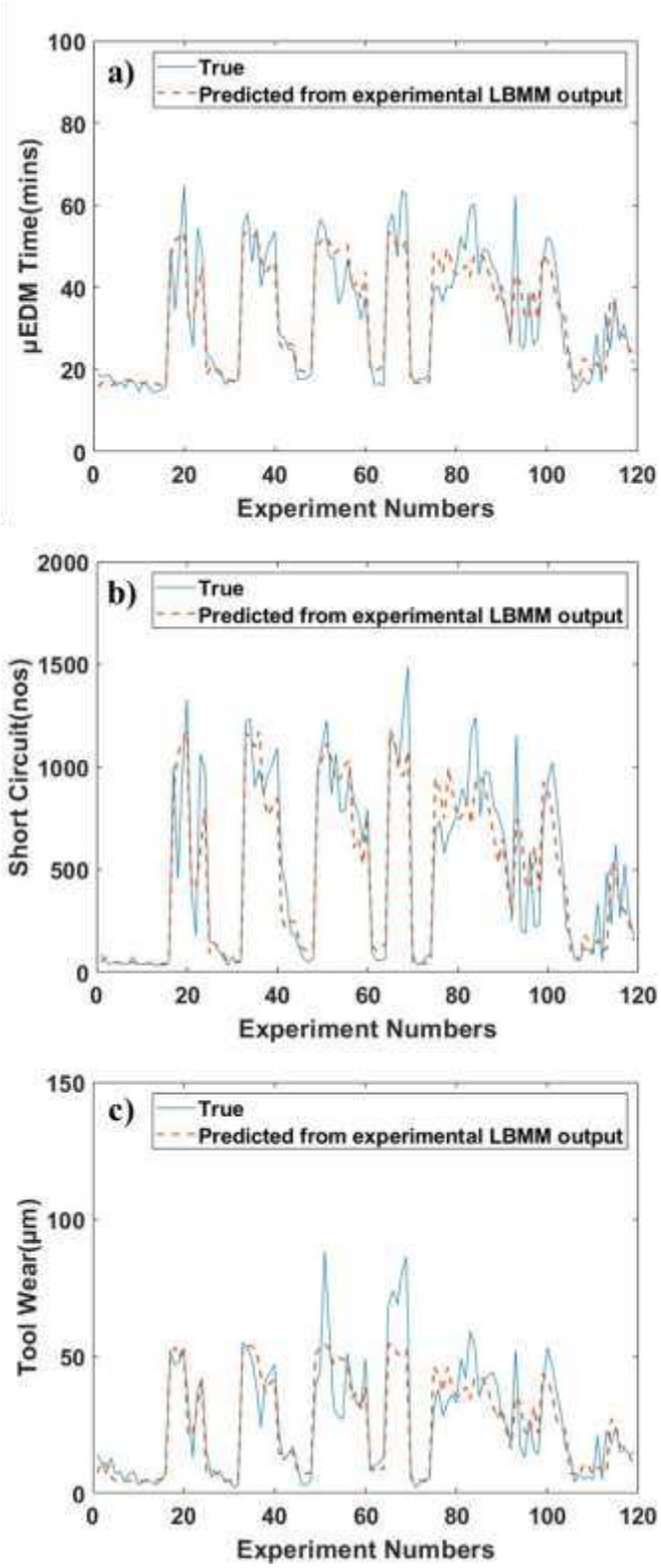

Figure 9: Comparison between the actual output and predicted output for the second stage of the model, (a) µEDM machining time (b) short circuit count, and (d) tool wear.

Study of the holistic performance of the dual-stage ANN model

For the holistic performance, the LBMM inputs (power, scanning speed, loop count, and pulse repetition rate) were used to predict the first stage's outputs (entry area, exit area, HAZ and

recast layer). Then these outputs were fed into the second stage model to estimate the overall performance parameter of the LBMM-µEDM process, namely µEDM machining time, short circuit count and toot wear. Finally, the model estimated values of the µEDM machining time, short circuit count and toot wear were compared with the actual experimental findings and the RMSE for each of the variables was calculated, which were found to be 0.1272, 0.1085, 0.097 for µEDM machining time, short circuit count and toot wear respectively. The corresponding prediction accuracy is shown in Figure 10, which is in a range of (~87% to ~90%). The experimental output of the µEDM machining time, short circuit count and toot wear compared with the predicted value by the dual-stage ANN model as described in Figure 11. Figure 12 further compares the overall network performance (between 1st stage, 2nd stage and holistic performance) by calculating the lumped accuracy described by equation (6). It can be seen that the performance of the 1st stage model is better than the second stage model as the causality between the input and output is more dominant for the 1st stage model as compared to the 2nd stage one. Further, the dual-stage ANN model's holistic performance is lower than the 1st and 2nd stage because the prediction inaccuracy of the 1st stage model influences the whole model's estimation accuracy.

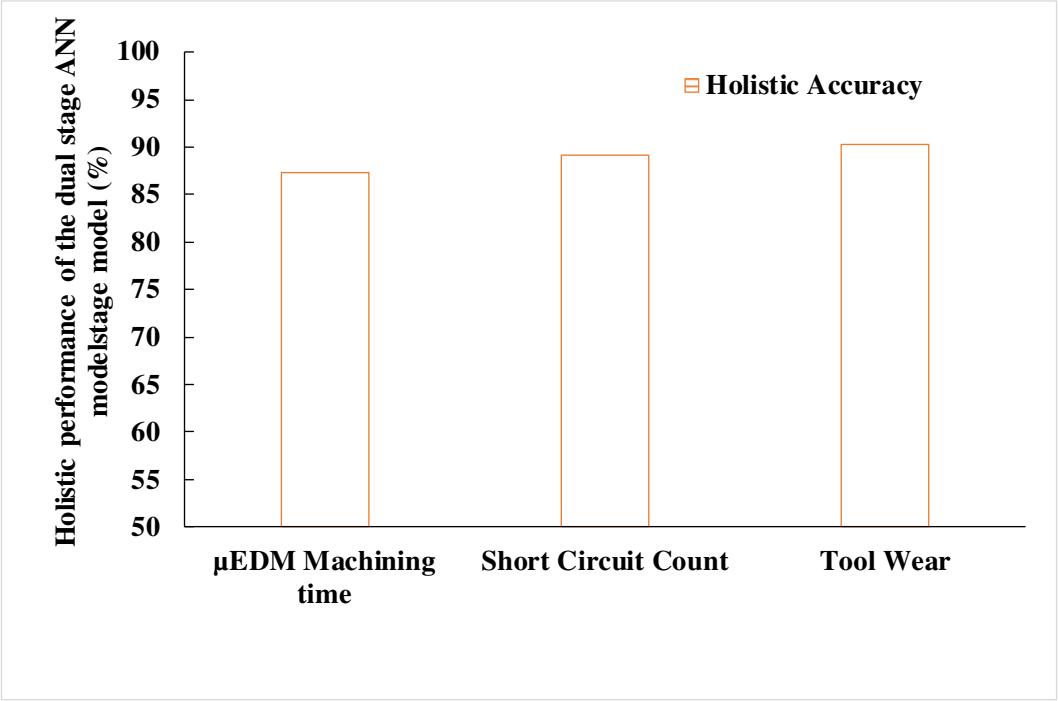

Figure 10: Holistic performance of the dual-stage ANN model for µEDM machining time, short circuit count and toot wear.

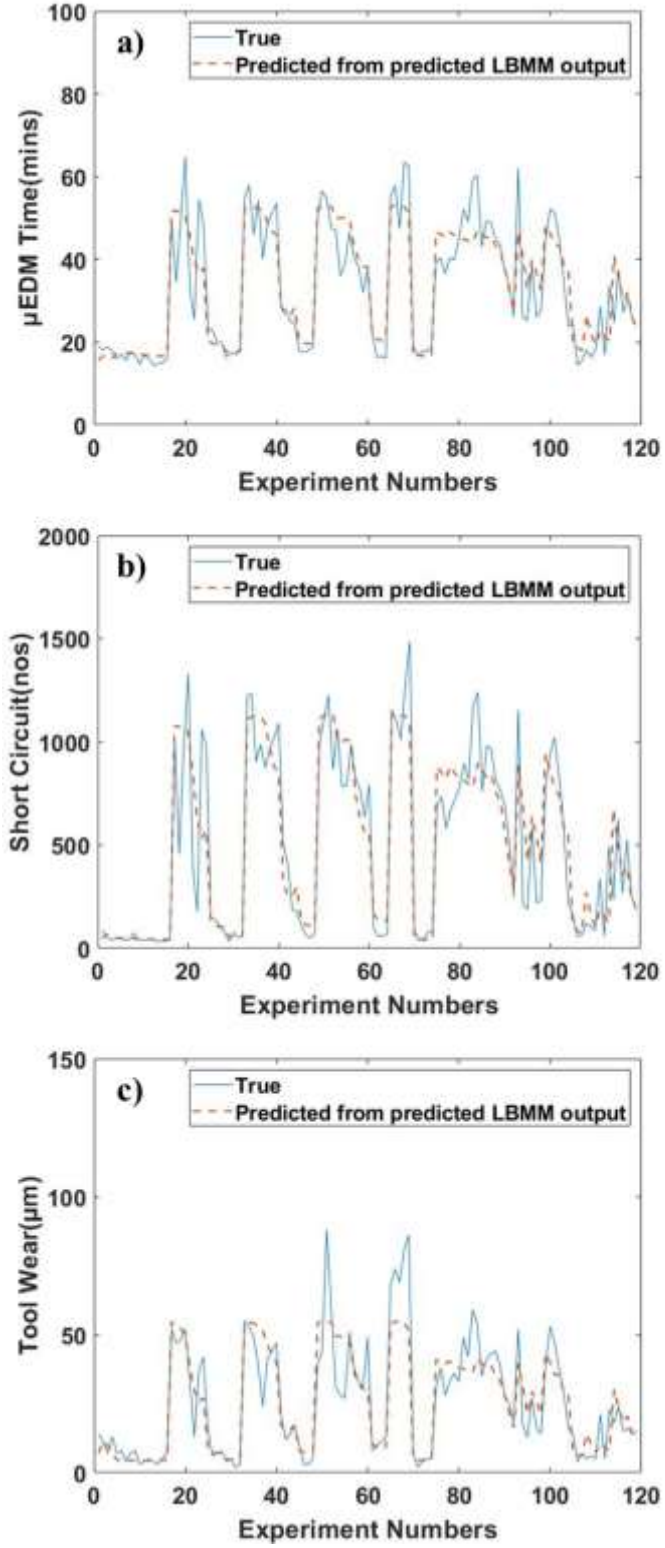

Figure 11: Comparison between experimental values and estimated values by the dual-stage ANN model (a) µEDM Machining Time (b) Short Circuit Count, and (d) Tool Wear.

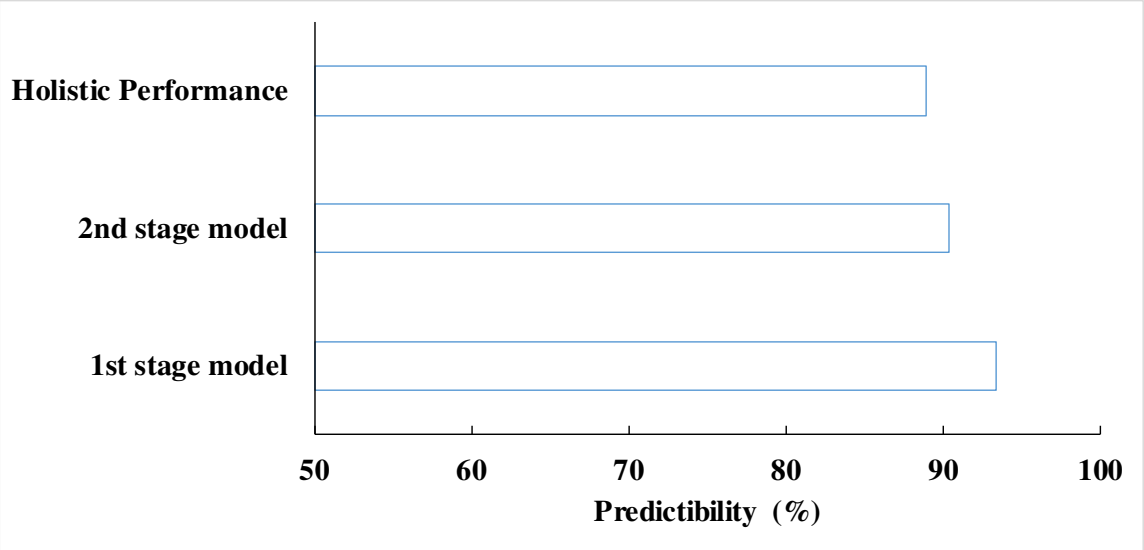

Figure 12: Comparison of the performance between 1st stage model, 2nd stage model and the holistic performance.

Parametric Study

The variation of different input parameters has a different effect on the output parameters of the LBMM-μEDM based sequential process. The parametric study of the said sequential micromachining process helped us understand various interrelated phenomena. This section outlines the parametric variation of various outputs using experimental data and predicted data from the ANN model. The predicted data were inverse transformed before they were used for the analysis.

Study of the LBMM method

This section describes the effect of different LBMM input parameters, mainly loop count, scanning speed and laser power, on the LBMM output variables such as entry area, exit area, HAZ and recast layer. The effect of the pulse repetition rate was found to be irregular; hence was not considered for detail discussion for the current study.

Effect of Laser Power

Figure 13 (a-d) illustrates the effect of laser power on various parameters of the LBMMed pilot holes such as entry area, exit area, HAZ and recast layer for both experimental and predicted dataset (an average trend for various pulse repetition rate). All the output parameters were found to have a rising tendency with the increment of incident laser power, as seen in Figure 13, which is consistent with our correlation analysis as described in Table 2. Moreover, the predicted values were found to match the actual experimental values, and the parameter exit area performed the best, as indicated in the earlier section. Higher incident power values indicate higher energy density, which results in high levels of thermal interaction between the laser beam and the workpiece. Hence, the incident laser removed a high-level material from the bulk portion of the initial LBMMed holes. Increased energy density allowed the heat to flow across the material cross-section, and therefore the LBMMed holes formed by higher power exhibits a much larger exit Area. HAZ [39] also increased with incident power as the heat interaction is much larger. However, it was observed that at the lowest scanning speed (50

mm/s), HAZ tends to decrease as incident laser power increased from 9.4W to 15.5W. The reason could be because at the lowest scanning speed; the heat may have penetrated more towards the depth direction instead of transmitting radially. As for the recast layer, the molten material was ejected much at a higher rate with the increase in laser power; that is why the recast layer was increased, which is in line with the previous findings as reported in [40]. Both the highest HAZ, 0.741mm^2 (for the entire dataset) and highest recast layer, 0.053mm^2 ((for the entire dataset) was formed at the highest power of 15.5W. The estimated values of various output parameters show the same trend validating the first stage model's accuracy.

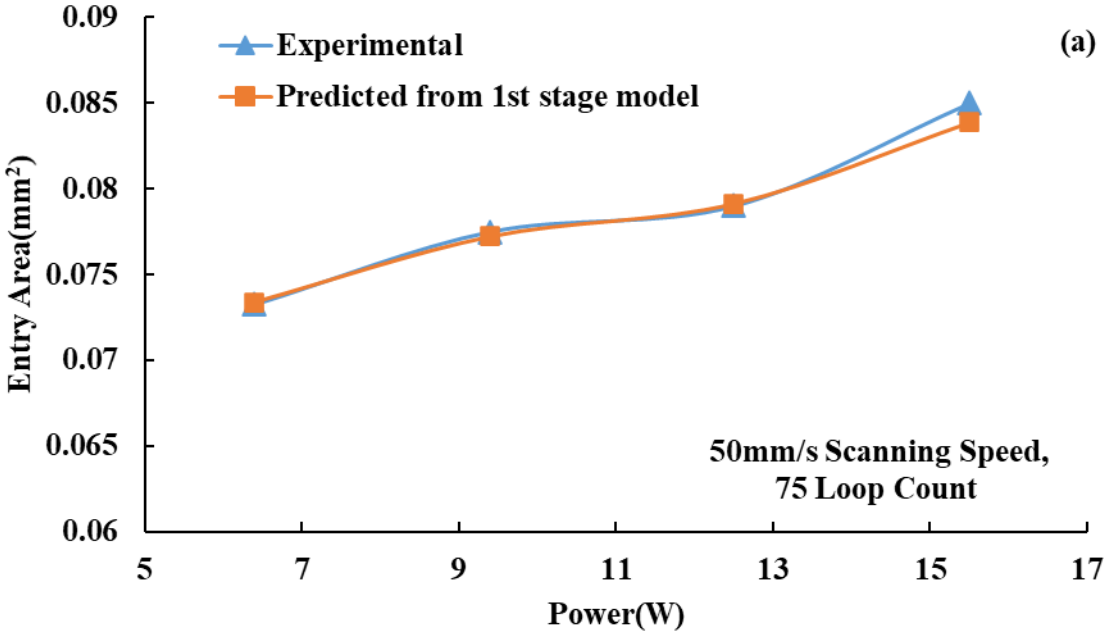

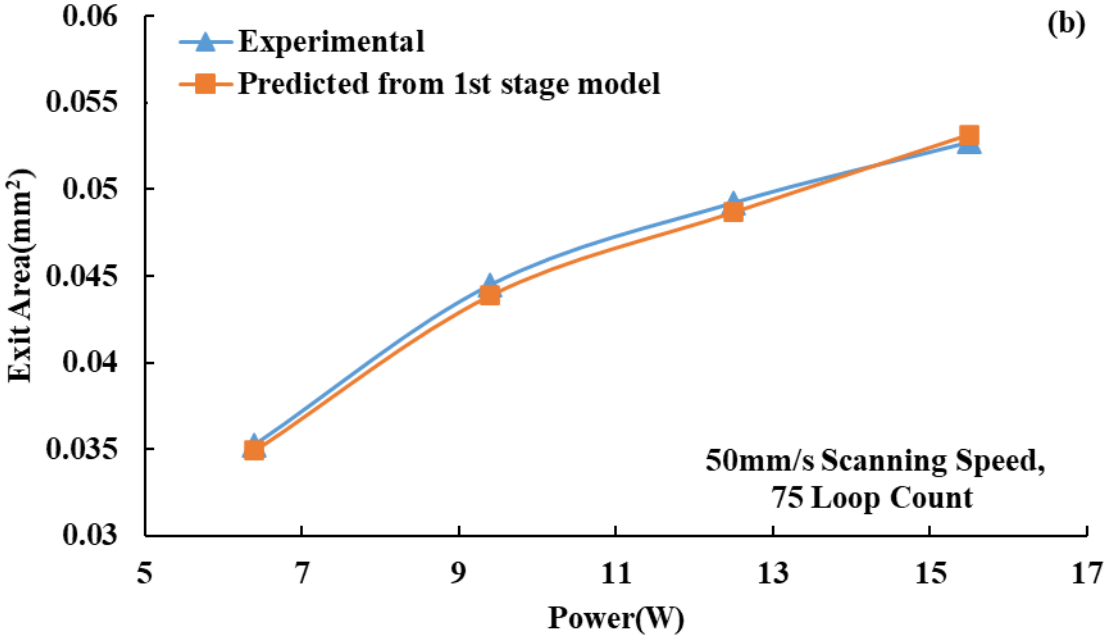

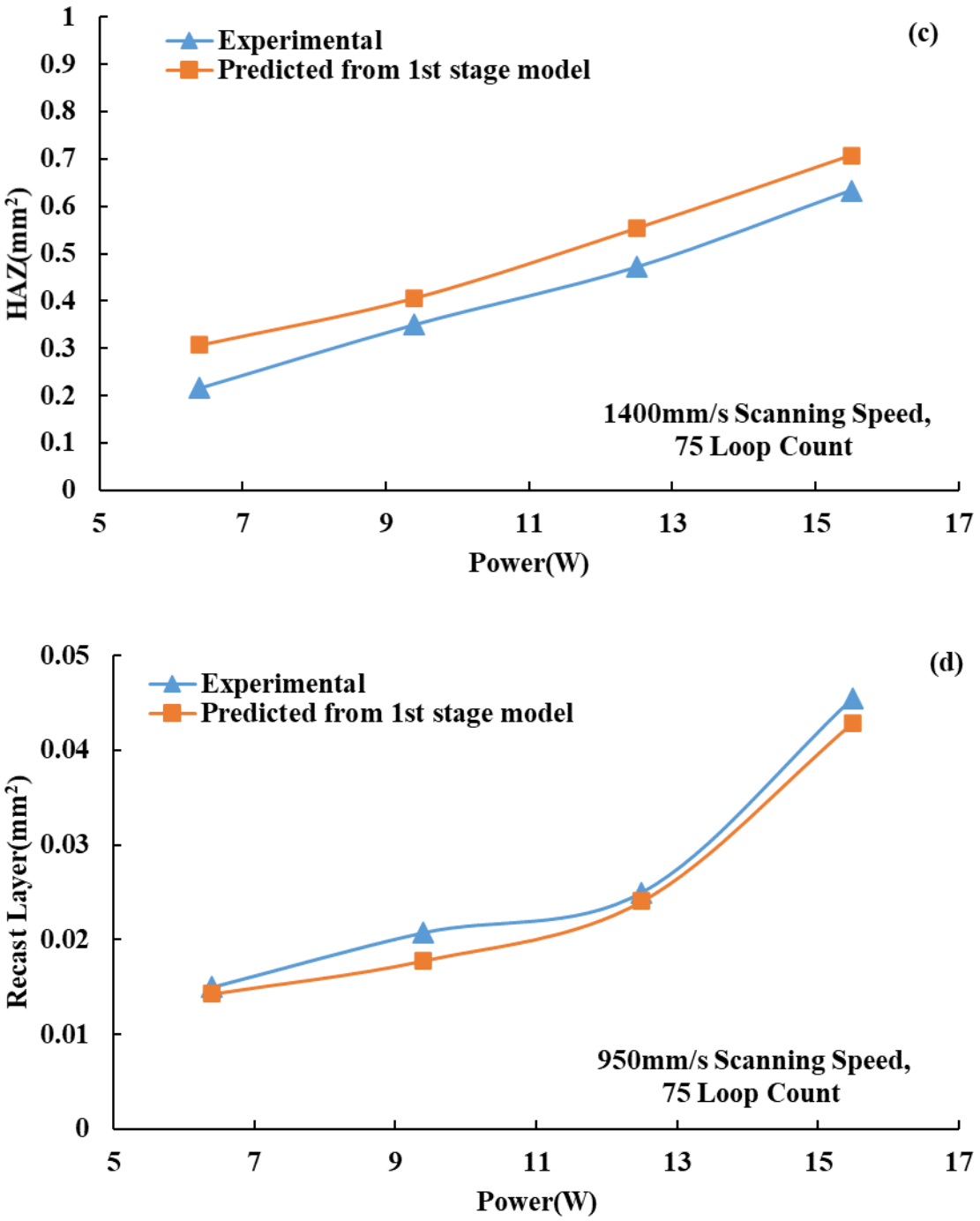

Figure 13: Effect of laser power on LBMM output parameters. LBMM output parameters were averaged for various pulse repetition rate. The data in the graph is from experimental values and predicted values from the first stage model, (a) laser power effect on the entry area at 50 mm/s scanning speed, (b) laser power effect on the exit area at 50 mm/s scanning speed, (c) laser power effect on the HAZ at 1400 mm/s scanning speed and d) laser power effect on the recast layer at 950 mm/s scanning speed.

Effect of Scanning Speed

Figure 14 (a-d) describes how laser scanning speed influences the LBMMed holes' characteristics, namely entry area, exit area, HAZ and recast layer (an average trend for various pulse repetition rate). With the increase of scanning speed, the entry area and the exit area both decreases (Figure 14(a) and Figure 14(b)) as incident energy is lesser due to shorter thermal interaction between the laser beam and the material.

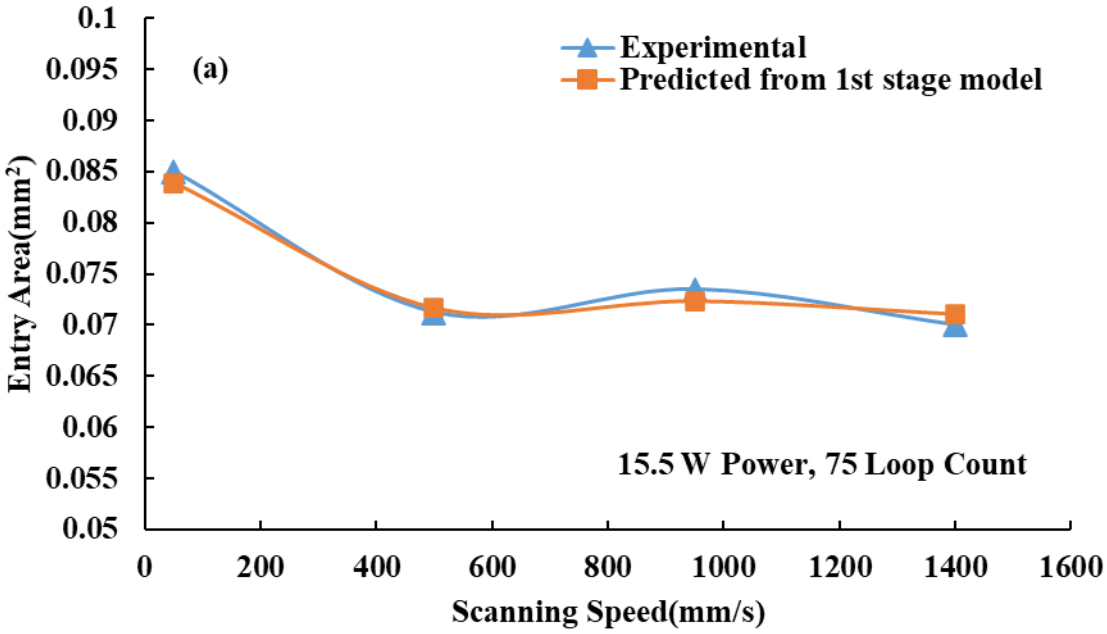

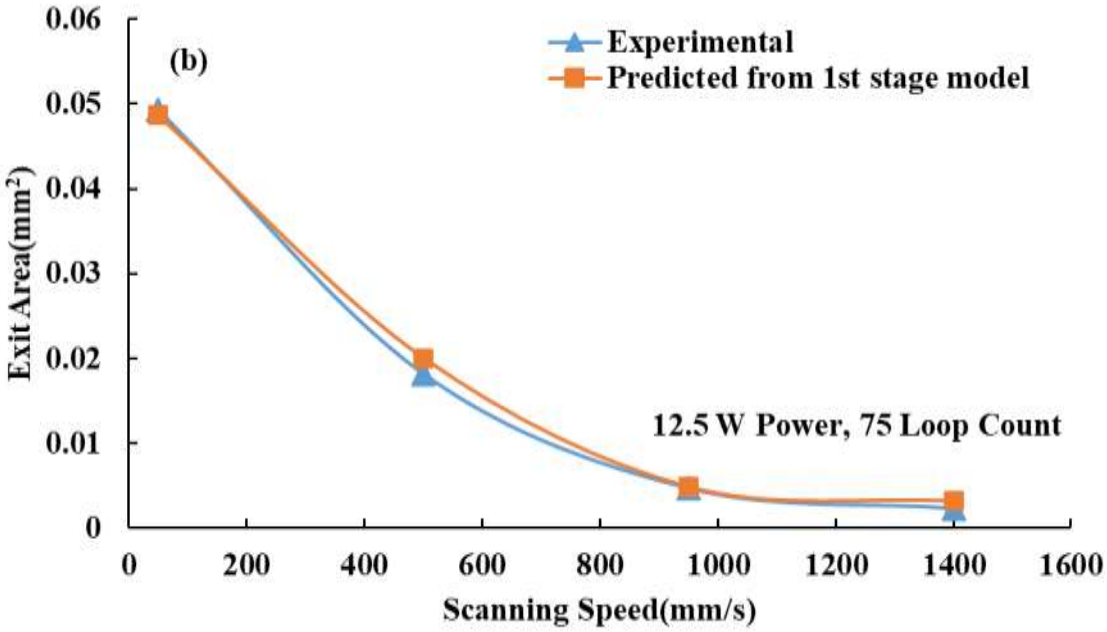

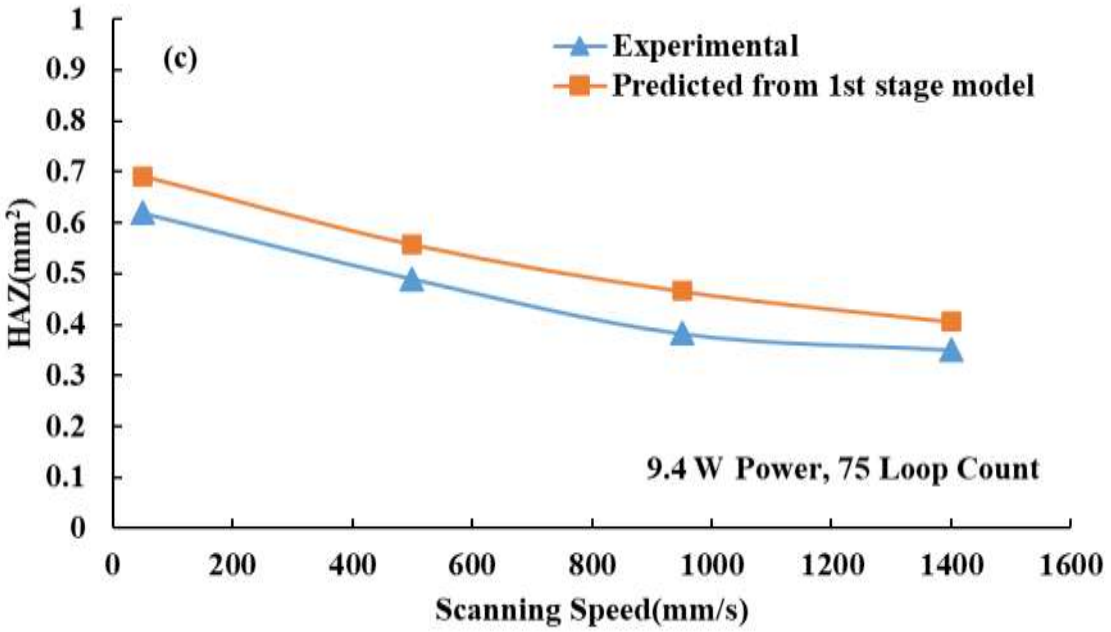

Figure 14: Effect of scanning speed on LBMM output parameters. LBMM output parameters were averaged for various pulse repetition rate. The data in the graph is from experimental values and predicted values from the first stage model, (a) scanning speed effect on entry area at 15.5W laser power (b) scanning speed effect on the exit area at 12.5W laser power, and (c) scanning speed effect on HAZ at 9.4W laser power and d) scanning speed effect on recast layer at 12.5W laser power.

Negarestani et al. [41] provided an equation for energy density for the laser machining process, which shows that incident energy density decreases with higher scanning speed. As a result, this would result in low material removal from the workpiece surface. However, it can be said from Figure 14 (a) and Figure 14 (b) that the effect of laser scanning speed on the exit area is more profound as compared to the entry area. Figure 14 (c) shows that the HAZ also lessens with the increase of scanning speed as the energy density decreases. Low energy density caused a lesser flow of heat along the surface; thus, the HAZ also decreased accordingly. The recast layer also generally decreased as the scanning speed increased because of a similar reason, as explained for the HAZ. However, for the highest laser incident power (15.5W), the recast layer was found to have a random relationship with the scanning speed. The reason might be at the highest level, the laser power is more prevalent over the scanning speed and resolidifies the molten material inconsistently with the scanning speed variation.

Effect of Loop Count

The effect of loop count on LBMM outputs such as entry area and recast layer was insignificant, as mentioned earlier in the study of the correlation coefficient Table 2. However, the exit area and the HAZ associated with the LBMMed holes increased with the loop count increase. As the thermal interaction between the material and the laser was increased with each pass. We also found from the experimental data that the laser scanning speed highly influenced the change. For a moderate scanning speed of 400 mm/s with 10.66W of laser incident power, the range of change of exit area and HAZ (with the variation of loop count) were 0.019mm^2 and 0.356mm^{2,} respectively. As the scanning speed was increased to 900 mm/s with the same

incident power, the above two parameters' range dropped to 0.000930463 mm^2 (~20 x) and 0.127 mm^2 (~3 x), respectively. The above finding indicates that laser scanning speed is a more dominant factor than the loop count. As for the laser power, we did not find any strong causality between the increase in the laser power and the rate of increase of exit area and HAZ with loop count.

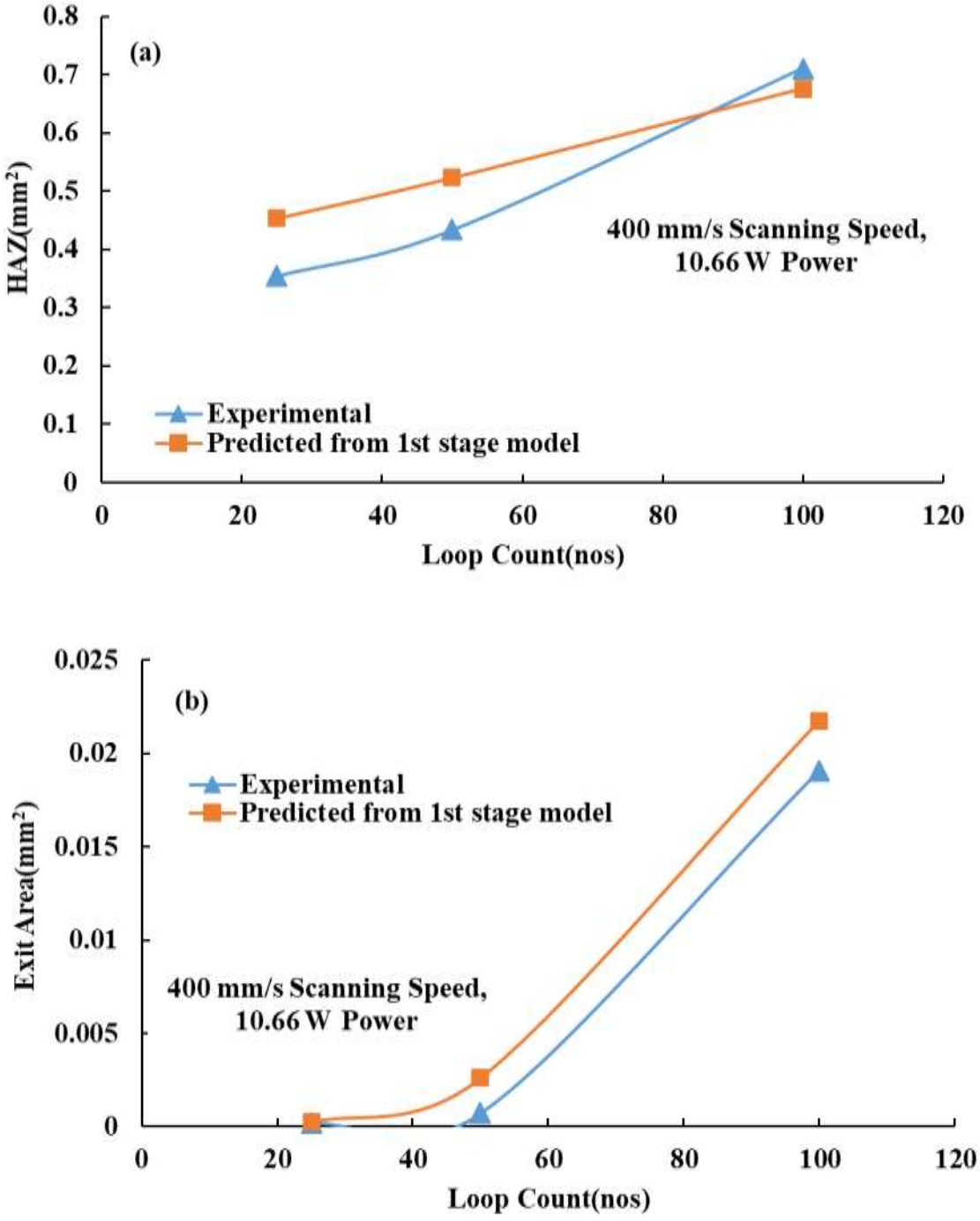

Figure 15: Effect of loop count on HAZ and exit area of the LBMMed holes. The graph's data is from experimental values and predicted values from the training data (a) effect of loop count on HAZ, and (b) effect of loop count on exit area of the holes.

Study of µEDM Finishing Operation

This section presents how various LBMM input parameters affect the outcome of subsequent µEDM finishing and thereby describes the sequential micromachining process's performance. After the LBMM method is applied to produce the pilot hole, the subsequent µEDM finishing improves the hole's overall quality. Figure 16 (a-f) shows the morphological comparison between the LBMMed hole, LBMMed hole subsequently finished by µEDM and pure EDMed hole. It can be inferred from Figure 16 (a-f) that the quality of the LBMM-µEDMed hole and pure µEDMed hole are of a similar level, and both of them are far better than pure LBMMed hole in terms of the circularity, edge sharpness, recast layer (Figure 16(a-c)). Moreover, the tilted view also confirms that the inner surface quality of the LBMMed hole is significantly more inferior compared to LBMM-µEDMed hole and pure µEDMed hole Figure 16 (d-f). Moreover,

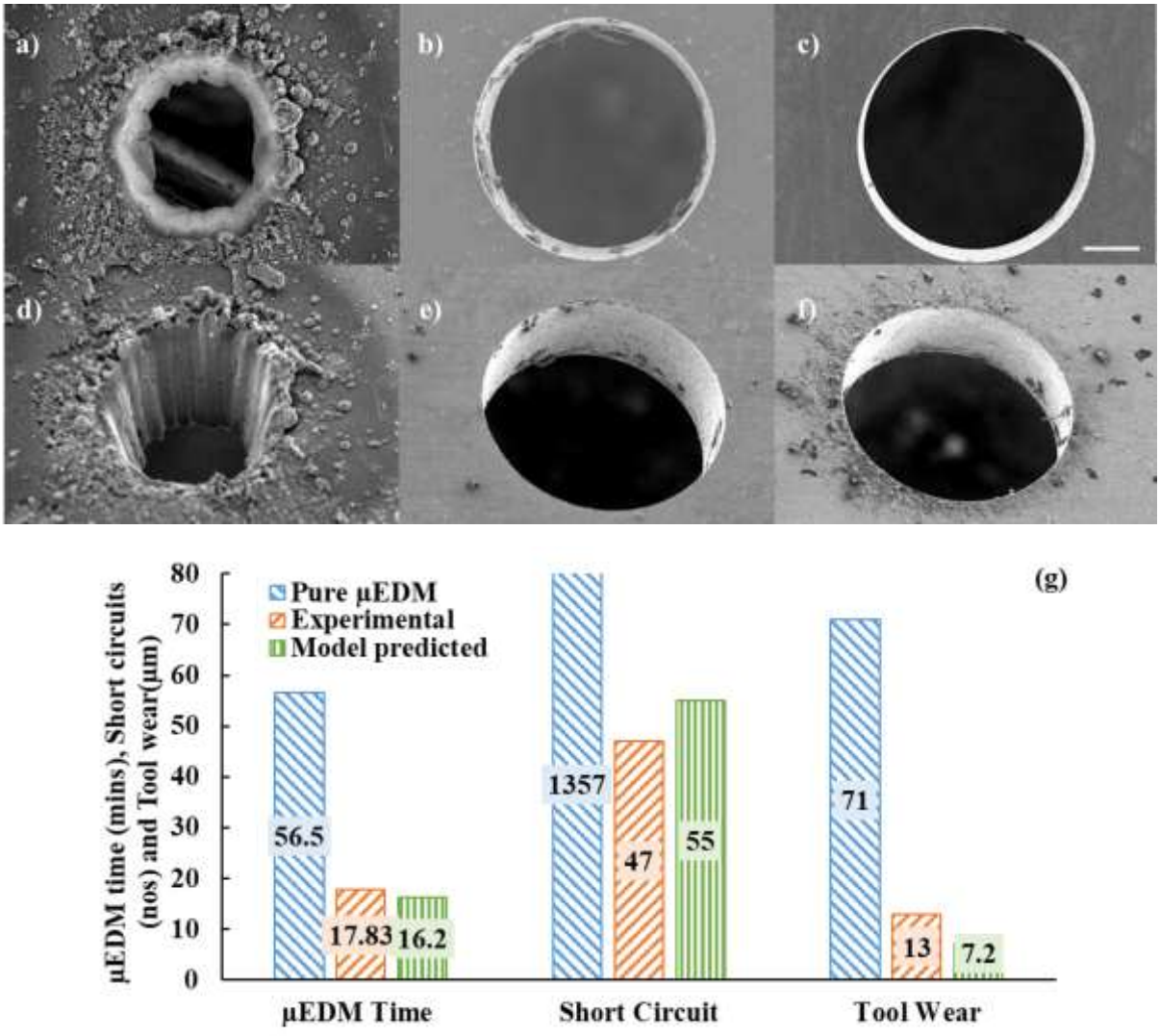

Figure 16: Morphological and performance comparison between LBMMed hole((a) and (d)), LBMM-µEDMed hole((b) and (e)), pure µEDMed hole((c) and (f)). Scale bar = 100µm, and (g) shows the µEDM performance comparison between pure µEDM and LBMM- µEDM process.

Figure 16 (g) also suggests that the sequential LBMM-μEDM can achieve a similar quality hole as compared to the μEDM process with a significantly reduced machining time (~ 3 x), short circuit count (~25 x), and tool wear (~5.5 x) both for experimental and predicted value.

Machining time for μEDM

The machining time by the μEDM process is one of the most crucial parameters, if not the most crucial parameters of the LBMM- μEDM process, as this primarily defines the overall production rate. Figure 17 (a-d) shows the combined effect of laser scanning time and incident power used to pre-machine the pilot holes on μEDM's final finishing time. It is to note that Figure 17 has been plotted using the experimental data, predicted data from the actual LBMMed holes parameters (entry area, exit area, HAZ, and recast layer) using the second stage model and estimated data from the dual-stage model (i.e. LBMM inputs were used to predict the LBMMed holes' parameters using 1st stage model and then this dataset was used to predict the μEDM machining time). Also, to note that the four pulse repetition rate data were averaged up for plotting Figure 17. It can be said from Figure 17 that generally, higher scanning speed used to carry out pilot hole machining by the LBMM process requires higher time to conduct the final finishing operation by μEDM. This trend can be explained from the analysis of Figure 14 (a-b), which shows that higher scanning speed causes lesser volume removed by the LBMM process; hence longer time is required to finish by μEDM. However, the scanning speed effect was less evident at a high power zone like 15.5W, as shown in Figure 17 (d). Figure 17 (a-d) also suggests that if laser scanning speed is as low as 50 mm/s (loop count is constant at 75), all incident power levels used for machining the LBMMed holes will require a comparable time for μEDM's finishing operation. The reason is that the volume removed by the LBMM process (indicated by the entry area and exit area of the holes) with 50 mm/s scanning speed is of a similar range for the full spectrum of the incident power (6.4W to 15.5W) for both experimental data and data predicted by the 1st stage model as can be referred to the supplementary data file. It can be reasonably said from Figure 17 that the proposed dual-stage ANN model for the sequential LBMM-μEDM process predicts that with a laser incident power of higher than 12.5W and scanning speed of less than 400 mm/s can be used for the LBMM process (with a constant loop count of 75) to achieve the μEDM finishing time within 20 minutes. Further, Figure 17 shows some discrepancies between the experimental value and the predicted value, which may be resulted from the uncertainty of the μEDM process due to its stochastic nature.

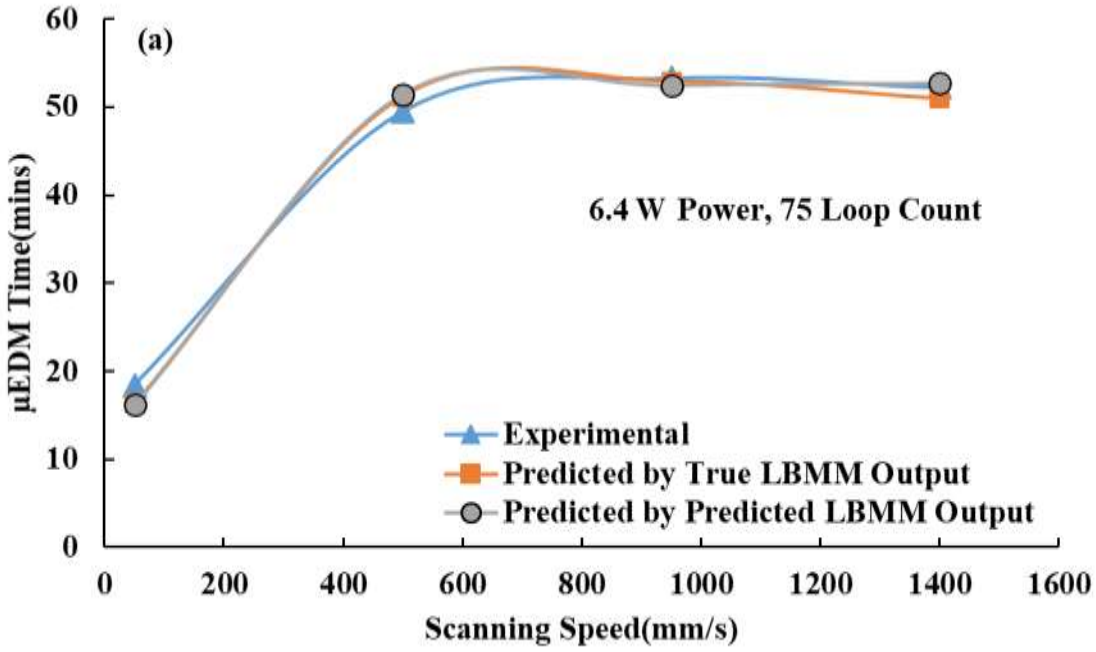
(a)
6.4 W Power, 75 Loop Count
μEDM Time(mins)
Scanning Speed(mm/s)
Experimental
Predicted by True LBMM Output
Predicted by Predicted LBMM Output
0
10
20
30
40
50
60
0
200
400
600
800
1000
1200
1400
1600

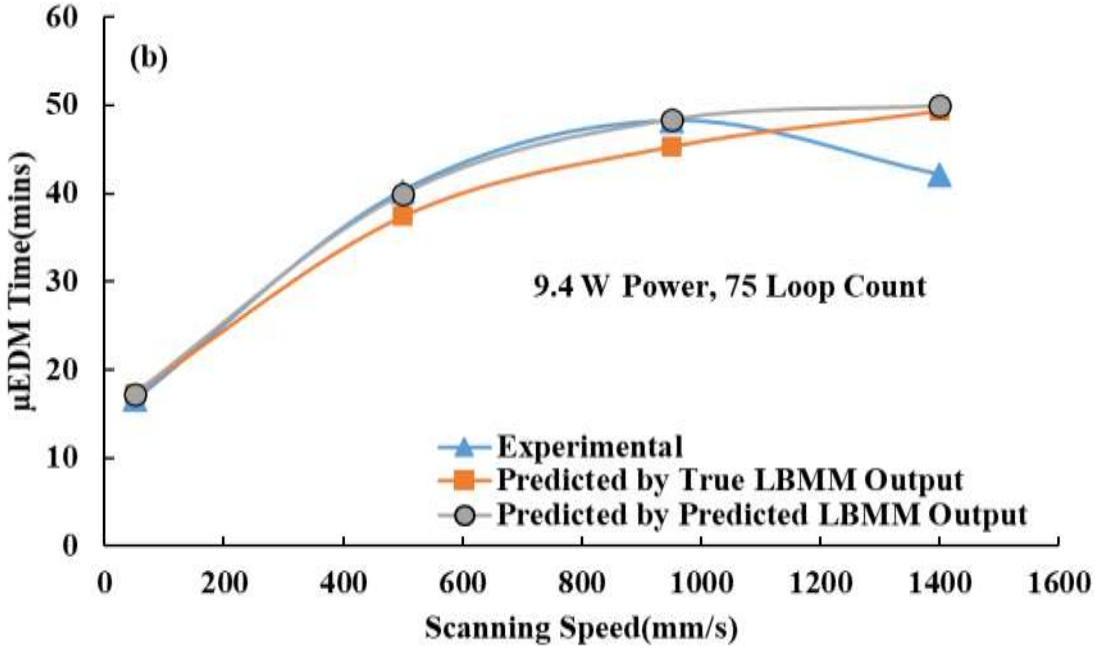
(b)
9.4 W Power, 75 Loop Count
μEDM Time(mins)
Scanning Speed(mm/s)
Experimental
Predicted by True LBMM Output
Predicted by Predicted LBMM Output
0
10
20
30
40
50
60
0
200
400
600
800
1000
1200
1400
1600

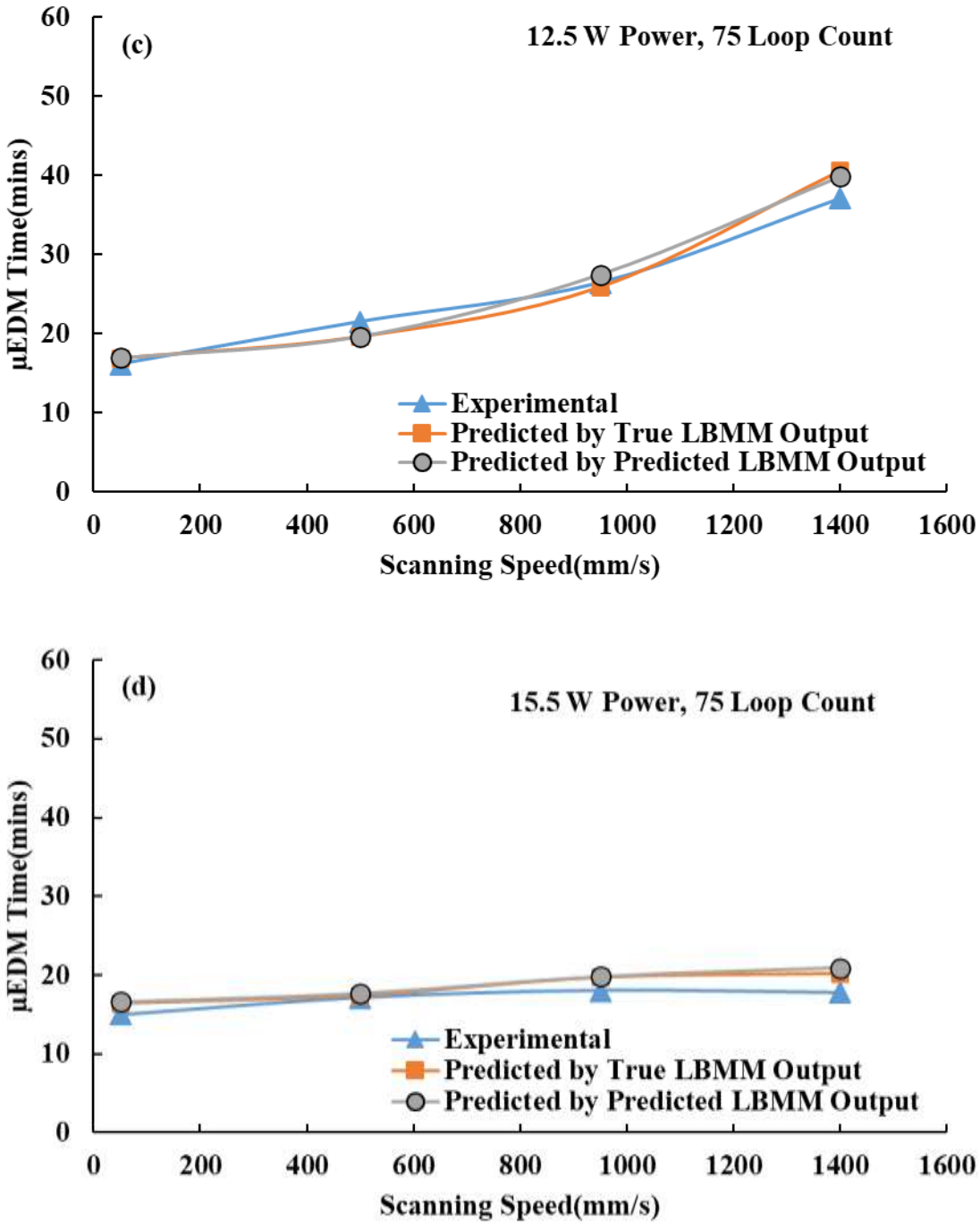

Figure 17: Variation of µEDM machining time with scanning speed used for LBBMed pre-machined holes at different laser power. The graph's data is from experimental values, predicted values from the actual LBMMed holes' parameters and estimated from predicted LBMMed holes' parameters. The holes were pre-machined at (a) 6.4 W laser power, (b) 9.4 W laser power, (c) 12.5 W laser power, and d) 15.5 W laser power.

The higher value of the loop count to carry out the LBMM process caused more material to be removed from the pre-machined holes (as described in Figure 15 (b)); hence the µEDM finishing time was found to be shorter for holes laser ablated with higher loop counts (as described in Figure 18) for a constant incident laser power (11.9W), scanning speed (400mm/s) and pulse repetition rate (10kHz).

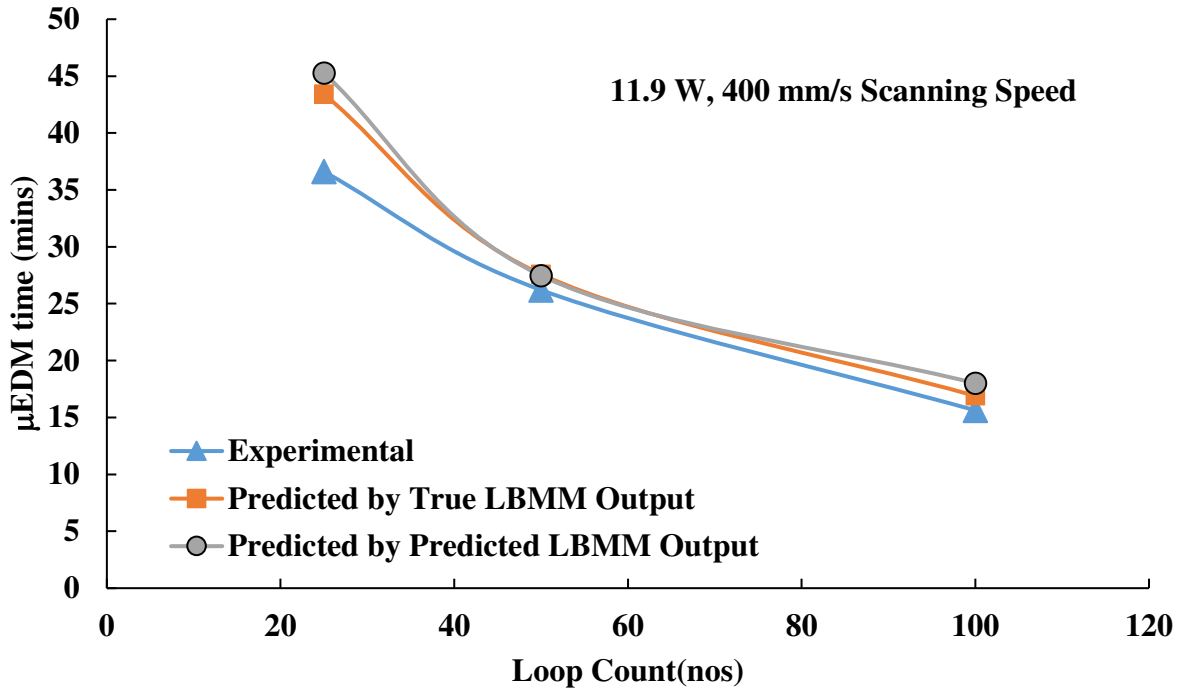

Figure 18: Variation of µEDM Machining Time with Loop Count for LBMMed pre-machined holes that were machined at 11.9W laser power, 400 mm/s scanning speed and 10kHz pulse repetition Rate. The graph's data is from experimental values, predicted values from the true LBMMed holes' parameters and estimated from predicted LBMMed holes' parameters.

Short circuit count and tool wear for µEDM

The short circuit is an intrinsic yet detrimental phenomenon associated with the µEDM finishing process as it causes no good spark to be generated. The cause of a short circuit is due to physical contact between the tool and debris or between the tool and workpiece at the machining zone. Like short circuit tool wear (considered vertical for the current study) is not desirable yet cannot be avoided due to the electrothermal erosion of the electrode during the µEDM operation. Both short circuit occurrence and vertical tool wear have higher chances to be increased if the µEDM machining time is increased, as shown in Figure 3. Figure 3 shows that both short circuit count and vertical tool wear are highly correlated to machining time with a correlation coefficient value of more than 0.9.

We observed that the LBMM input those were used to produce larger pilot holes and eventually the µEDM time was in a range of ~20 minutes also experienced total short circuits count ~< 100 nos and total vertical tool wear ~<15 µm (both for experimental and predicted value by the dual-stage ANN model). On the other hand, the short circuit count and vertical tool wear increased rapidly (short circuit count was ~ >1000 nos total vertical tool wear was ~>35 µm both for experimental and predicted value by the dual-stage ANN model) as the machining time of the finishing operation for LBMMed holes increased to ~>50 minutes., Figure 19 and Figure 20 were plotted to study the rate of short circuit occurrence and the rate of tool wear during the µEDM finishing operation. As before, the four pulse repetition rate data were averaged up for plotting Figure 19 and Figure 20. It can be reasonably inferred from Figure 19

that at lower scanning speed like 50mm/s (Figure 19 (a)); the short circuit occurrence rate is pretty consistent within the range of 5nos/min for the whole range of incident power because of the high volume of material being removed by the LBMM process which eases up the second stage μEDM operation. However, for scanning speed ranges from 500 mm/s and higher, a low level of laser power used during the LBMM process caused a very high rate of short circuit occurrence (during the secondary finishing operation) and drastically reduced as the laser power was increased(Figure 19 (b-d)). The output from the dual-stage model shows the average trend (Figure 19 (a-d)) instead of converging itself for each localized value; hence some discrepancies can be observed with the experimental values. Further, an experimental short circuit may sometimes provide a false signal due to the uncertainty of the short circuit detection circuit. During the μEDM, the tool wear rate follows a trend similar to the short circuit occurrence rate described in Figure 20 (a-d). If a higher scanning speed (≥ 500 mm/s) with low incident laser power (6.4W) is used during the LBMM process, the electrode will experience a tool wear rate of ~1μm/min during the finishing by the μEDM operation. However, if the LBMM process is conducted with high power (15.5W) with any scanning speed, the tool wear rate can be almost reduced by ~50% during the μEDM operation.

Figure 21 (a-b) shows the effect of loop count used for the LBMM process (at constant scanning speed and laser incident power) on the short circuit occurrence rate and tool wear rate during fine machining by μEDM. The rate for both the parameters steadily reduces as a higher loop count was used for LBMMed holes as it helped to remove more material from the ablated zone, which helped alleviate the μEDM process by reducing the short circuit occurrence rate and tool wear rate.

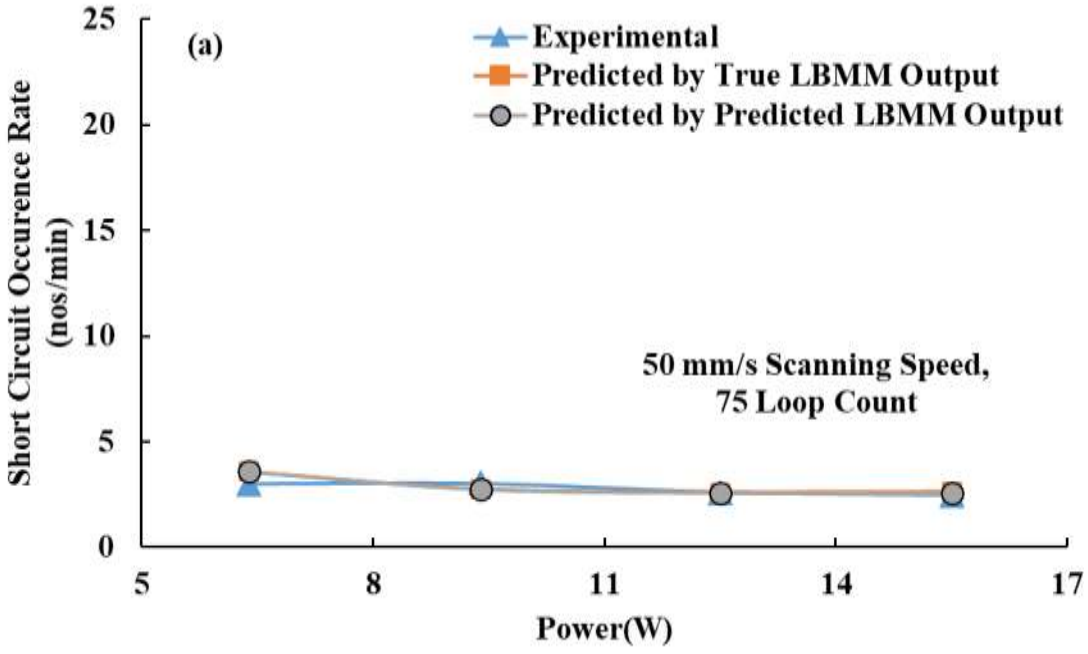

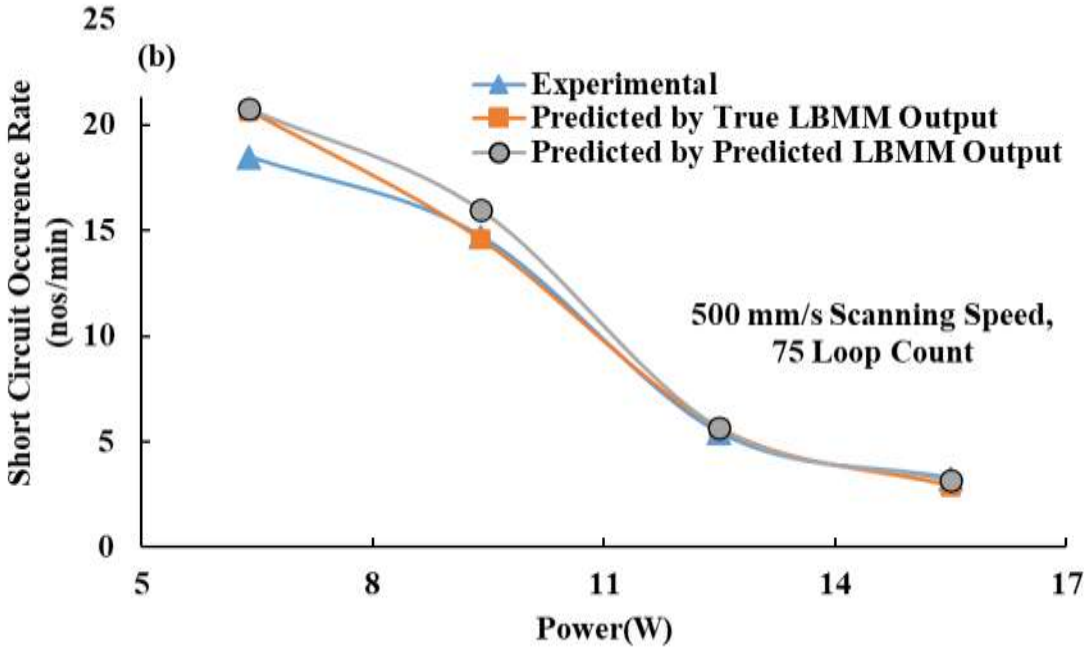
(b)
Experimental
Predicted by True LBMM Output
Predicted by Predicted LBMM Output
500 mm/s Scanning Speed,
75 Loop Count
Short Circuit Occurence Rate (nos/min)
Power(W)
0
5
10
15
20
25
5
8
11
14
17

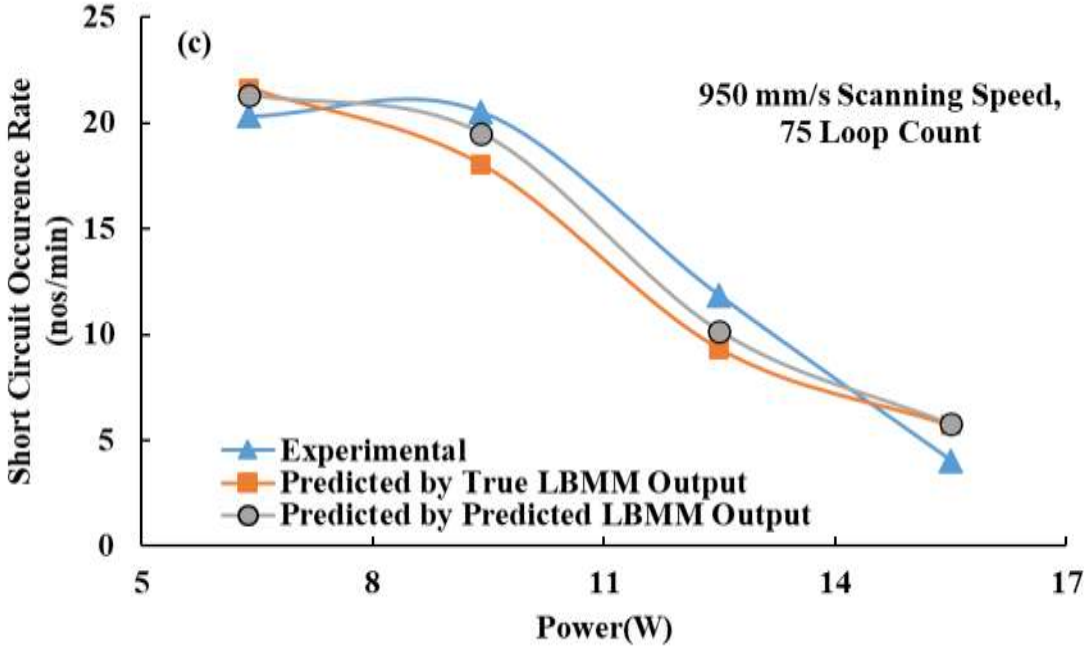
(c)
950 mm/s Scanning Speed,
75 Loop Count
Experimental
Predicted by True LBMM Output
Predicted by Predicted LBMM Output
Short Circuit Occurence Rate (nos/min)
Power(W)
0
5
10
15
20
25
5
8
11
14
17

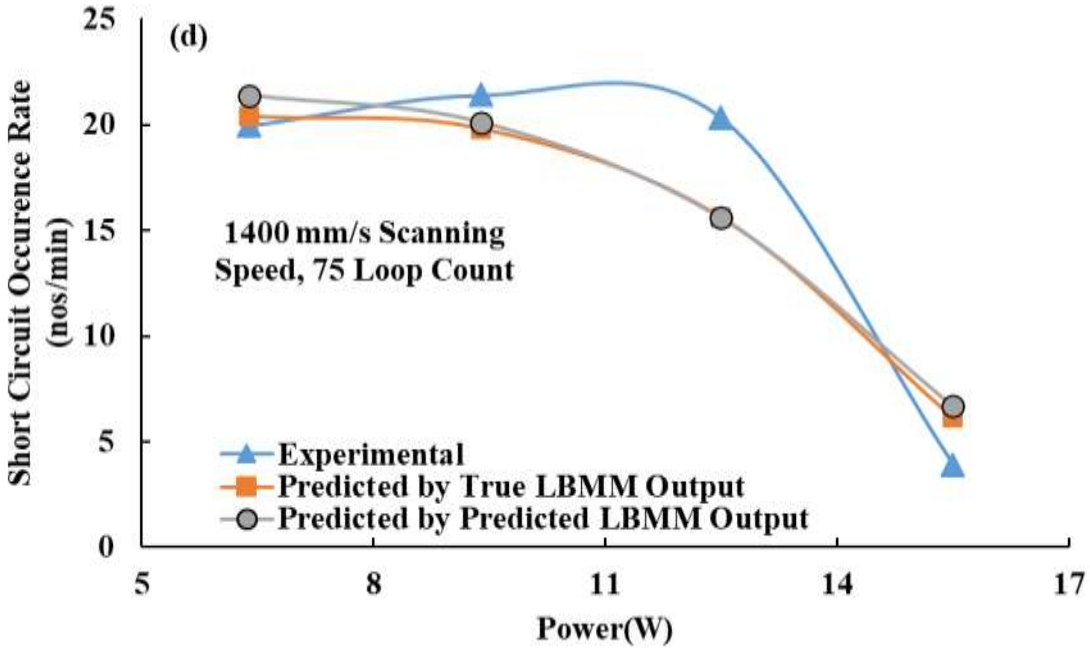

Figure 19: Effect of laser power on short circuit occurrence rate for LBMMed pre-machined holes at different scanning speed while loop count was kept constant at 75. The graph's data is from experimental values, predicted values from the true LBMMed holes' parameters and estimated from predicted LBMMed holes' parameters. The holes were pre-machined at (a) 50 mm/s scanning speed, (b) 500 mm/s scanning speed, (c) 950 mm/s scanning speed, and d) 1400 mm/s scanning speed.

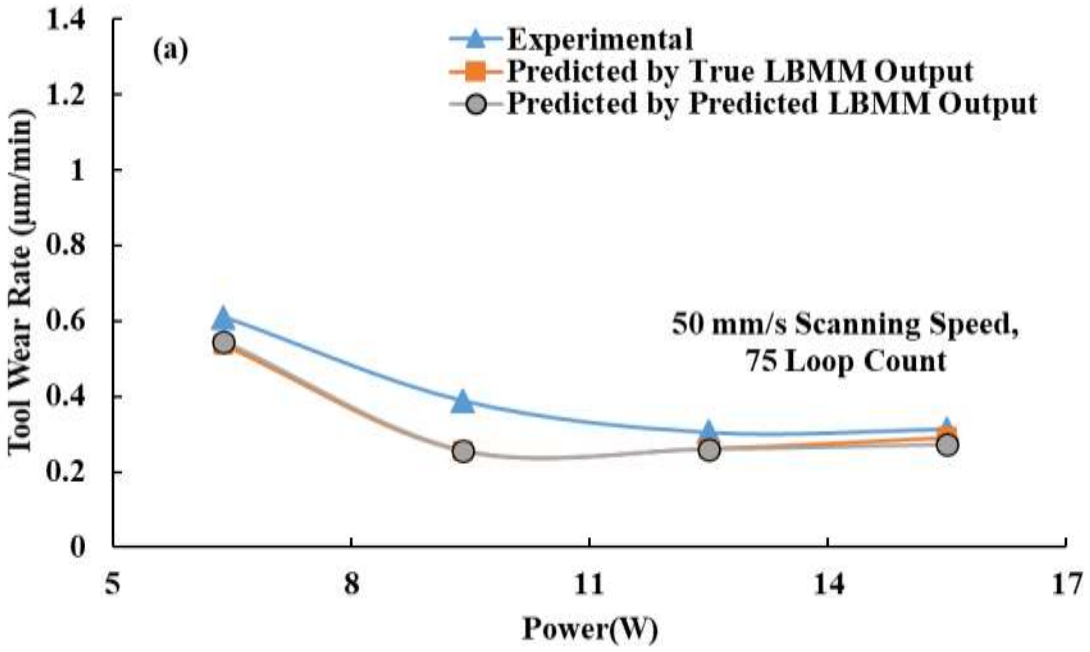

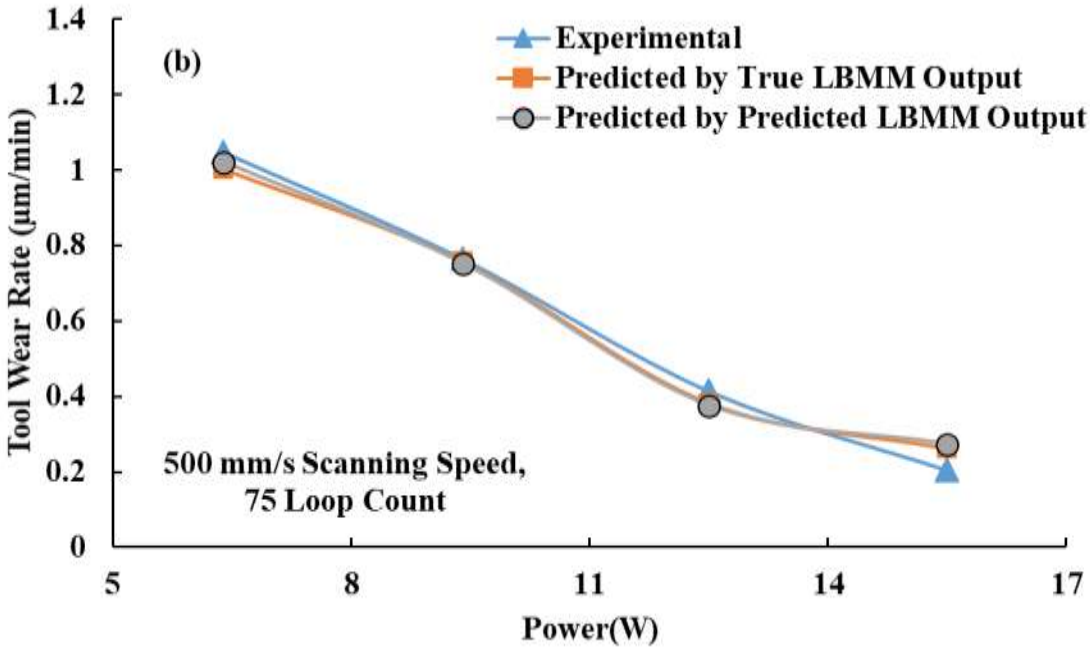
(b)
Experimental
Predicted by True LBMM Output
Predicted by Predicted LBMM Output
500 mm/s Scanning Speed,
75 Loop Count
Tool Wear Rate (µm/min)
Power(W)
1.4
1.2
1
0.8
0.6
0.4
0.2
0
5
8
11
14
17

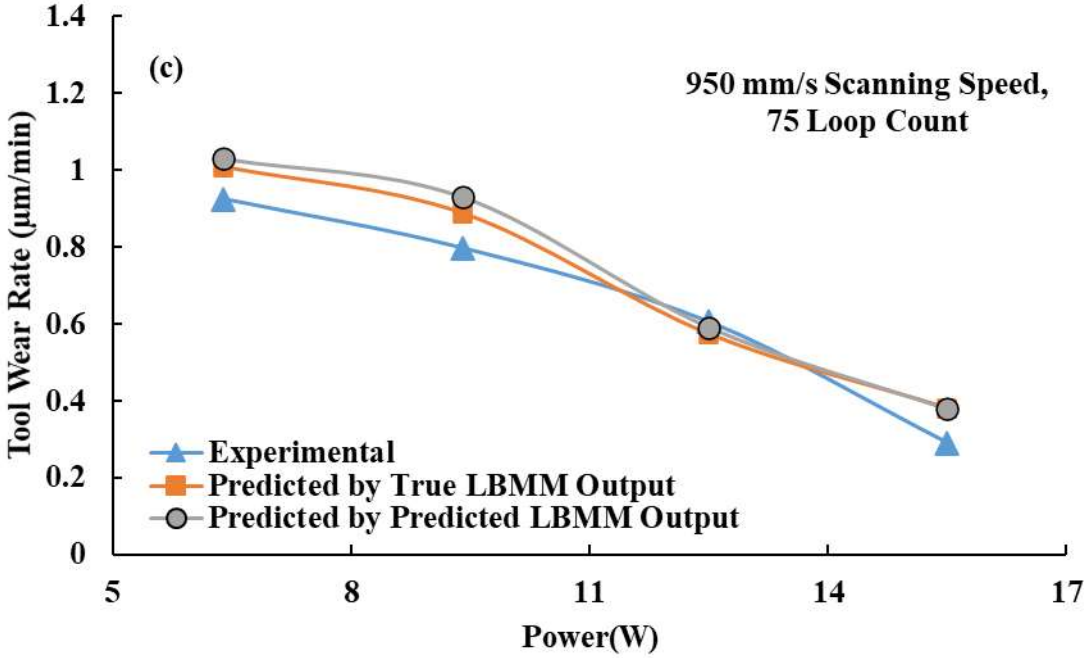
(c)
950 mm/s Scanning Speed,
75 Loop Count
Experimental
Predicted by True LBMM Output
Predicted by Predicted LBMM Output
Tool Wear Rate (µm/min)
Power(W)
1.4
1.2
1
0.8
0.6
0.4
0.2
0
5
8
11
14
17

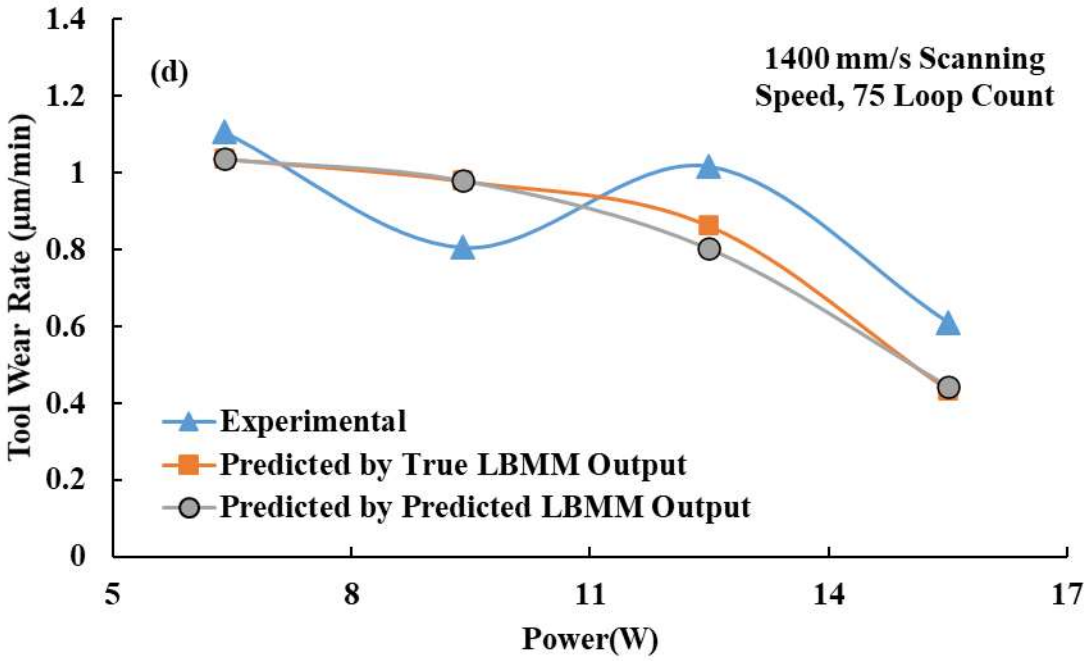

Figure 20: Effect of laser power on tool wear rate for LBMMed pre-machined holes at different Scanning Speed while loop count was kept constant at 75. The graph's data is from experimental values, predicted values from the true LBMMed holes' parameters and estimated from predicted LBMMed holes' parameters. The holes were pre-machined at (a) 50 mm/s Scanning Speed (b) 500 mm/s Scanning Speed (c) 950 mm/s Scanning Speed and d) 1400 mm/s Scanning Speed respectively.

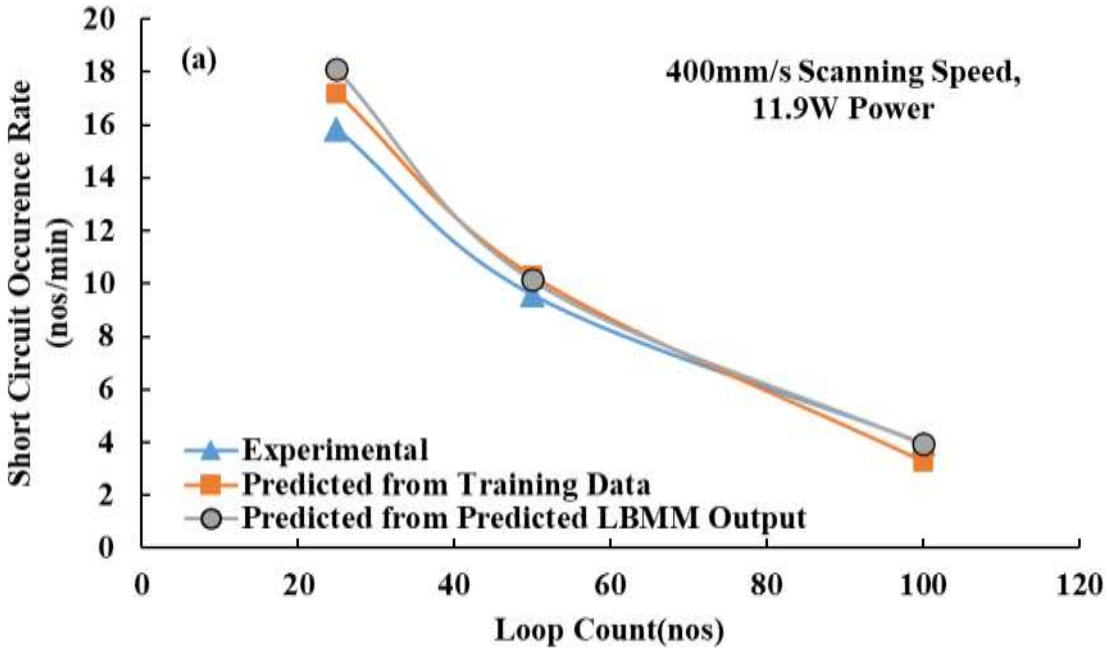

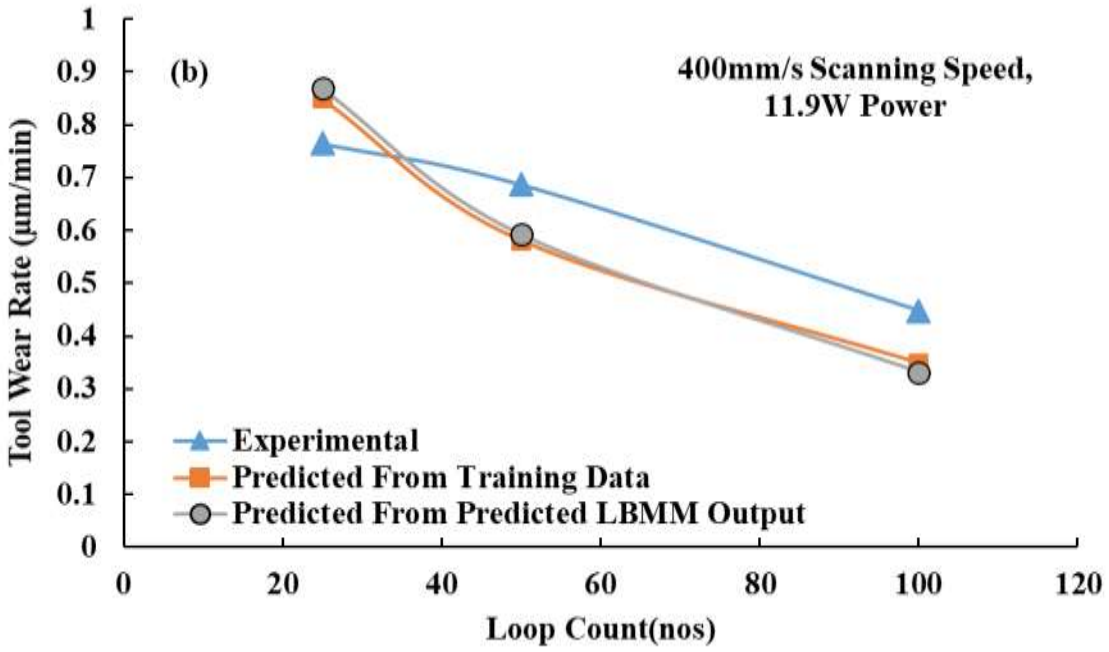

Figure 21: Effect of loop count on short circuit occurrence rate and tool wear rate for LBMMed pre-machined holes; pulse repetition rate was kept constant at 10kHz. The graph's data is from experimental values, predicted values from the true LBMMed holes' parameters and estimated from predicted LBMMed holes' parameters. The graphs illustrate the variation of (a) short circuit occurrence Rate and (b) tool wear rate of the holes pre-machined at 400mm/s scanning speed and 10.66W laser power.

Conclusion

This paper proposes a novel dual-stage ANN model for LBMM-µEDM based sequential micro-drilling of Stainless Steel(SS304). The model takes the various LBMM parameters such as incident laser power, scanning speed and pulse repetition rate as the input in the first stage to predict characteristic parameters of the LBMMed holes such as entry area, exit area, HAZ recast layer. These characteristics parameters are fed into the second stage of the model to estimate the finishing time by the µEDM method and the tool wear and short circuit count during the finishing process. The model's overall estimation accuracy was found to be ~87%, ~89% and ~90 % for µEDM machining time, short circuit count, and tool wear, respectively. From the parametric study, we found that the trained model tends to generalize the trend instead of converging locally, indicating that it is not overfitting the data. As per the model prediction, the µEDM finishing time can be maintained within ~ 20 minutes if the slowest scanning speed of 50mm/s is used for any range of incident laser power during the pilot hole machining LBMM. If the highest power of 15.5W is used with any scanning speed during the LBMM method, the µEDM finishing time is within ~ 20 minutes range. A higher loop count used for pre-machining by the LBMM process decreased the µEDM finishing time (both experimentally and by predicting the dual-stage ANN model). Like the µEDM machining time, the short circuit occurrence rate and tool wear rate were influenced by the input parameter of the preceding LBMM process experimentally and model prediction.

Declaration

Funding: This project was funded by the Ministry of Higher Education Malaysia (MOHE Grant No: FRGS/1/2018/TK03/UIAM/02/2) and Asian Office of Aerospace Research and Development (AOARD Grant No: BAA-AFRL-AFOSR-2016-0007). Mir Akmam Noor Rashid was paid as a graduate research assistant (GRA) from the MOHE grant and Wazed Ibne Noor was paid as a graduate research assistant from the AOARD grant.

Competing Interests: The authors declare that they have no financial interests.

Availability of data and materials: Uploaded as supplementary material.

Code availability: Can be made available upon request.

Authors' Contributions: Wazed Ibne Noor and Mir Akmam Noor Rashid are the graduate students involved in this project who actively carried out the experiments, characterizations, compilation and analysis of the data. Wazed Ibne Noor mainly contributed to drafting the article. Tanveer Saleh is the principal investigator of the projects who conceptualized whole research problems. He is the main supervisor of the above students and guided them during experimentation and data analysis. Azhar Bin Mohd Ibrahim is the co-supervisor of Wazed Ibne Noor, and he put his valuable feedback on the modelling approach. Mohamed Sultan Mohamed Ali is one of the research collaborators who provided crucial technical input on the manuscript.

Ethical Approval: This paper does not require any ethical approval as the study does not involve human participants or animals.

Consent to Participate: Not applicable as this work does not involve human subjects.

Consent to Publish: Not applicable as this work does not involve human subjects.

References

1. Masuzawa T (2000) State of the art of micromachining. CIRP Ann - Manuf Technol 49:473–488. https://doi.org/10.1016/S0007-8506(07)63451-9

2. Paul L, Babu J, Davim JP (2020) Non-conventional Micro-machining Processes. In: Materials Forming, Machining and Post Processing. Springer, pp 109–139

3. Dowding C, Borman A (2015) Laser-initiated ablation of materials. Laser Surf Eng Process Appl 523–546. https://doi.org/10.1016/B978-1-78242-074-3.00022-2

4. Li X, Guan Y (2020) Theoretical fundamentals of short pulse laser-metal interaction: A review. Nami Jishu yu Jingmi Gongcheng/Nanotechnology Precis Eng 3:105–125. https://doi.org/10.1016/j.npe.2020.08.001

5. Casalino G, Losacco AM, Arnesano A, et al (2017) Statistical Analysis and Modelling of an Yb: KGW Femtosecond Laser Micro-drilling Process. Procedia CIRP 62:275–280. https://doi.org/10.1016/j.procir.2016.06.111

6. Ultrafast lasers offer great promise as a unique manufacturing tool | Industrial Laser Solutions. https://www.industrial-lasers.com/home/article/16490420/ultrafast-lasers-offer-great-promise-as-a-unique-manufacturing-tool. Accessed 19 Jan 2021

7. Benton M, Hossan MR, Konari PR, Gamagedara S (2019) Effect of process parameters and material properties on laser micromachining of microchannels. Micromachines 10:. https://doi.org/10.3390/mi10020123

8. Teixidor D, Orozco F, Thepsonthi T, et al (2013) Effect of process parameters in nanosecond pulsed laser micromachining of PMMA-based microchannels at near-infrared and ultraviolet wavelengths. Int J Adv Manuf Technol 67:1651–1664. https://doi.org/10.1007/s00170-012-4598-x

9. Yang J, Sun S, Brandt M, Yan W (2010) Experimental investigation and 3D finite element prediction of the heat affected zone during laser assisted machining of Ti6Al4V alloy. J Mater Process Technol 210:2215–2222. https://doi.org/10.1016/j.jmatprotec.2010.08.007

10. Shivakoti I, Kibria G, Pradhan BB (2019) Predictive model and parametric analysis of laser marking process on gallium nitride material using diode pumped Nd:YAG laser. Opt Laser Technol 115:58–70. https://doi.org/10.1016/j.optlastec.2019.01.035

11. Tsai MJ, Li CH, Chen CC (2008) Optimal laser-cutting parameters for QFN packages by utilizing artificial neural networks and genetic algorithm. J Mater Process Technol 208:270–283. https://doi.org/10.1016/j.jmatprotec.2007.12.138

12. Vagheesan S, Govindarajalu J (2019) Hybrid neural network–particle swarm optimization algorithm and neural network–genetic algorithm for the optimization of quality characteristics during CO2 laser cutting of aluminium alloy. J Brazilian Soc Mech Sci Eng 41:328. https://doi.org/10.1007/s40430-019-1830-8

13. Norkey G, Dubey AK, Agrawal S (2014) Artificial intelligence based modeling and optimization of heat affected zone in Nd:YAG laser cutting of duralumin sheet. J Intell Fuzzy Syst 27:1545–1555. https://doi.org/10.3233/IFS-141121

14. Raju L, Hiremath SS (2016) A State-of-the-art Review on Micro Electro-discharge Machining. Procedia Technol 25:1281–1288. https://doi.org/10.1016/j.protcy.2016.08.222

15. Li L, Diver C, Atkinson J, et al (2006) Sequential laser and EDM micro-drilling for next generation fuel injection nozzle manufacture. CIRP Ann - Manuf Technol 55:179–182. https://doi.org/10.1016/S0007-8506(07)60393-X

16. Saleh T, Rasheed AN, Muthalif AGA (2015) Experimental study on improving μ-WEDM and μ-EDM of doped silicon by temporary metallic coating. Int J Adv Manuf Technol 78:1651–1663. https://doi.org/10.1007/s00170-014-6732-4

17. Tiwary AP, Pradhan BB, Bhattacharyya B (2014) Study on the influence of micro-EDM process parameters during machining of Ti–6Al–4V superalloy. Int J Adv Manuf Technol 76:151–160. https://doi.org/10.1007/s00170-013-5557-x

18. Mehfuz R, Ali MY (2009) Investigation of machining parameters for the multiple-response optimization of micro electrodischarge milling. Int J Adv Manuf Technol 43:264–275. https://doi.org/10.1007/s00170-008-1705-0

19. Yildiz Y (2016) Prediction of white layer thickness and material removal rate in electrical discharge machining by thermal analyses. J Manuf Process 23:47–53. https://doi.org/10.1016/j.jmapro.2016.05.018

20. D'Urso G, Maccarini G, Quarto M, et al (2016) Micro-electro discharge machining drilling of stainless steel with copper electrode: The influence of process parameters and electrode size. Adv Mech Eng 8:1–16. https://doi.org/10.1177/1687814016676425

21. Ming W, Ma J, Zhang Z, et al (2016) Soft computing models and intelligent optimization system in electro-discharge machining of SiC/Al composites. Int J Adv Manuf Technol 87:201–217. https://doi.org/10.1007/s00170-016-8455-1

22. Kumar S, Batish A, Singh R, Singh TP (2014) A hybrid Taguchi-artificial neural network approach to predict surface roughness during electric discharge machining of titanium alloys. J Mech Sci Technol 28:2831–2844. https://doi.org/10.1007/s12206-014-0637-x

23. Suganthi XH, Natarajan U, Sathiyamurthy S, Chidambaram K (2013) Prediction of quality responses in micro-EDM process using an adaptive neuro-fuzzy inference system (ANFIS) model. Int J Adv Manuf Technol 68:339–347. https://doi.org/10.1007/s00170-013-4731-5

24. P. M A, D C (2020) Prediction and analysis of process failures by ANN classification during wire-EDM of Inconel 718. Adv Manuf 8:519–536. https://doi.org/10.1007/s40436-020-00327-w

25. Moghaddam MA, Kolahan F (2020) Modeling and optimization of the electrical discharge machining process based on a combined arti cial neural network and particle swarm optimization algorithm. Sci Iran 27:1206–1217. https://doi.org/10.24200/SCI.2019.5152.1123

26. Chavoshi SZ, Luo X (2015) Hybrid micro-machining processes: A review. Precis Eng 41:1–23. https://doi.org/10.1016/j.precisioneng.2015.03.001

27. Rajurkar KP, Zhu D, McGeough JA, et al (1999) New developments in electro-chemical machining. CIRP Ann 48:567–579

28. Afiq Rashid M, Rahman M, Senthil Kumar A (2016) A study on compound micromachining using laser and Electric Discharge Machining (EDM). Adv Mater Process Technol 2:258–265. https://doi.org/10.1080/2374068X.2016.1164531

29. Al-Ahmari AMA, Rasheed MS, Mohammed MK, Saleh T (2015) A Hybrid Machining Process Combining Micro-EDM and Laser Beam Machining of Nickel–Titanium-Based Shape Memory Alloy. Mater Manuf Process 31:447–455. https://doi.org/10.1080/10426914.2015.1019102

30. Kim S, Kim BH, Chung DK, et al (2010) Hybrid micromachining using a nanosecond pulsed laser and micro EDM. J Micromechanics Microengineering 20:. https://doi.org/10.1088/0960-1317/20/1/015037

31. Pajak PT, De Silva AKM, McGeough JA, Harrison DK (2004) Modelling the aspects of precision and efficiency in laser-assisted jet electrochemical machining (LAJECM). J Mater Process Technol 149:512–518. https://doi.org/10.1016/j.jmatprotec.2003.10.055

32. Bhondwe KL, Yadava V, Kathiresan G (2006) Finite element prediction of material removal rate due to electro-chemical spark machining. Int J Mach Tools Manuf 46:1699–1706. https://doi.org/10.1016/j.ijmachtools.2005.12.005

33. Feng S, Huang C, Wang J, Zhu H (2017) Investigation and modelling of hybrid laser-waterjet micromachining of single crystal SiC wafers using response surface methodology. Mater Sci Semicond Process 68:199–212. https://doi.org/10.1016/j.mssp.2017.05.029

34. Parandoush P, Hossain A (2014) A review of modeling and simulation of laser beam machining. Int J Mach Tools Manuf 85:135–145. https://doi.org/10.1016/j.ijmachtools.2014.05.008

35. Yeo SH, Aligiri E, Tan PC, Zarepour H (2009) A new pulse discriminating system for Micro-EDM. Mater Manuf Process 24:1297–1305. https://doi.org/10.1080/10426910903130164

36. Singh AK, Patowari PK, Deshpande N V. (2017) Effect of tool wear on microrods fabrication using reverse μEDM. Mater Manuf Process 32:286–293. https://doi.org/10.1080/10426914.2016.1198015

37. Schneider CA, Rasband WS, Eliceiri KW (2012) NIH Image to ImageJ: 25 years of image analysis. Nat Methods 9:671

38. Burden F, Winkler D (2008) Bayesian regularization of neural networks. Artif neural networks 23–42

39. Miraoui I, Boujelbene M, Zaied M (2016) High-power laser cutting of steel plates: Heat affected zone analysis. Adv Mater Sci Eng 2016:. https://doi.org/10.1155/2016/1242565

40. Marimuthu S, Antar M, Chantzis D (2015) High Speed Quasi-CW Fibre Laser Drilling of Aerospace Alloys. In: Lasers in Manufacturing Conference 2015

41. Negarestani R, Li L (2012) Laser machining of fibre-reinforced polymeric composite materials. In: Machining Technology for Composite Materials. Elsevier, pp 288–308

Figures

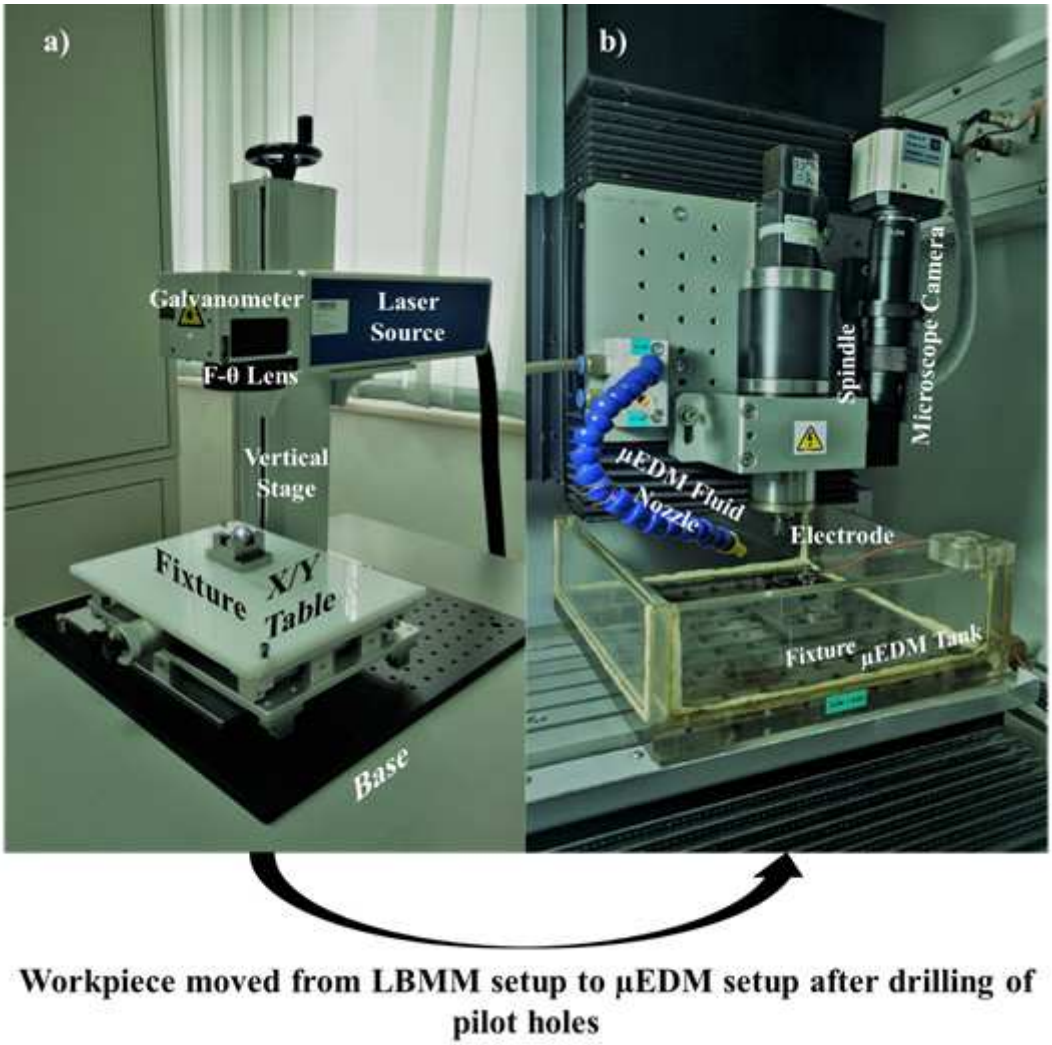

Figure 1

See the Manuscript Files section for the complete figure caption.

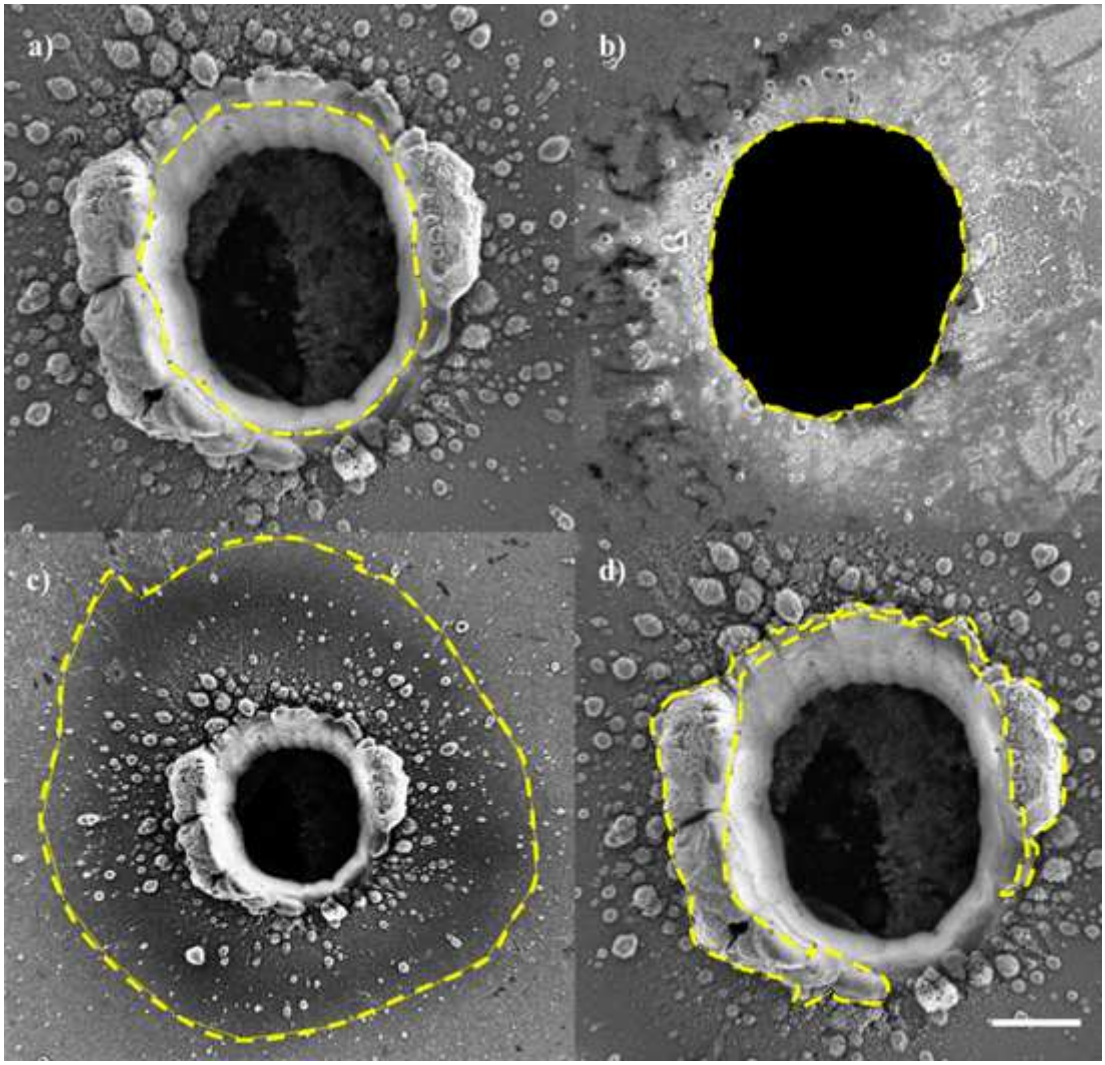

Figure 2

See the Manuscript Files section for the complete figure caption.

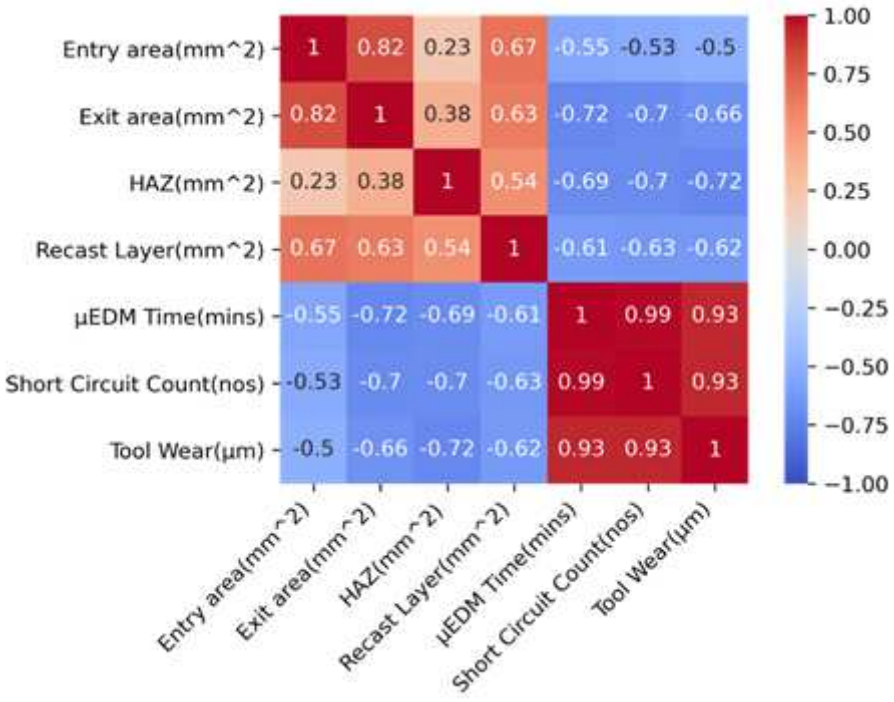

Figure 3

See the Manuscript Files section for the complete figure caption.

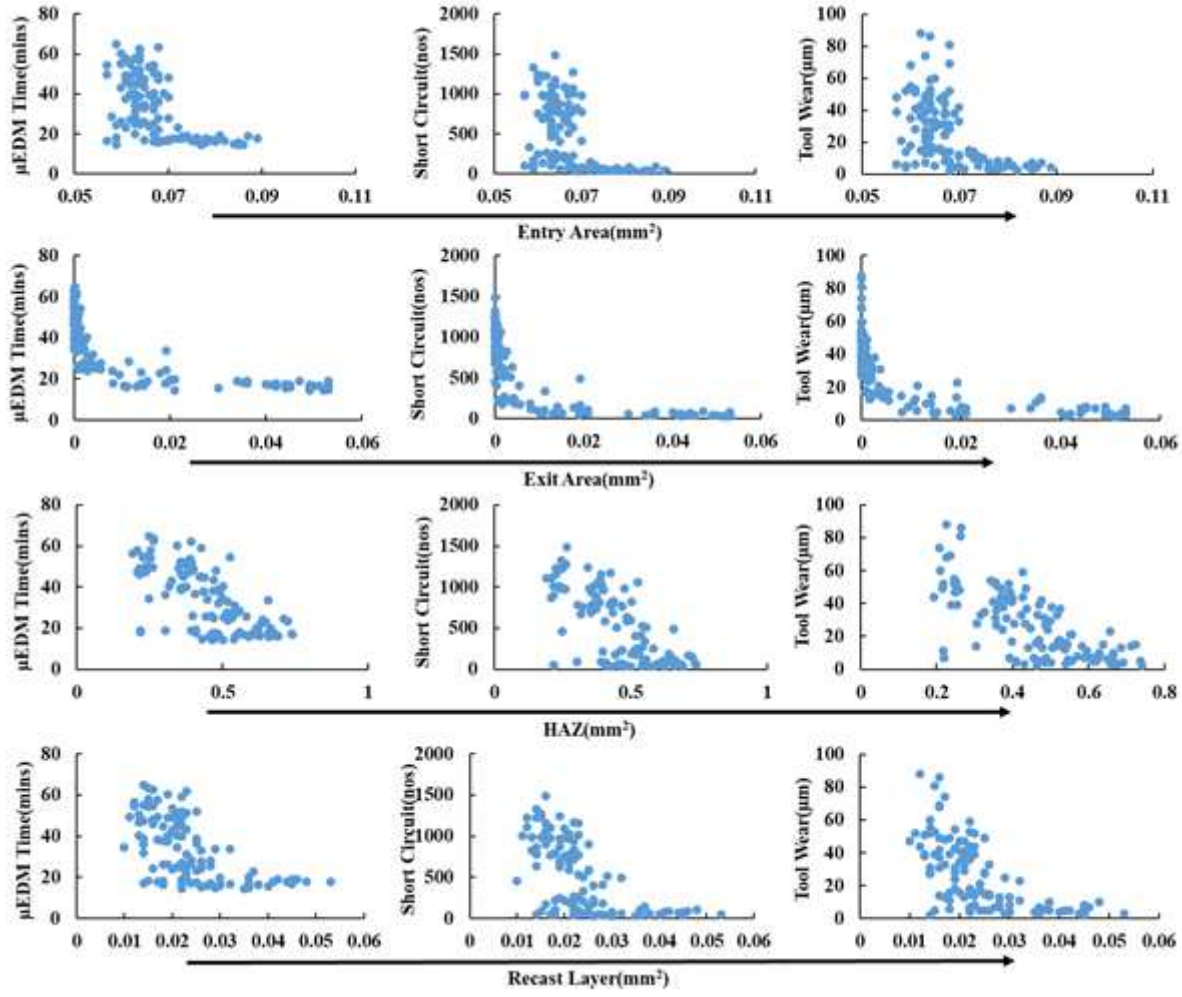

Figure 4

See the Manuscript Files section for the complete figure caption.

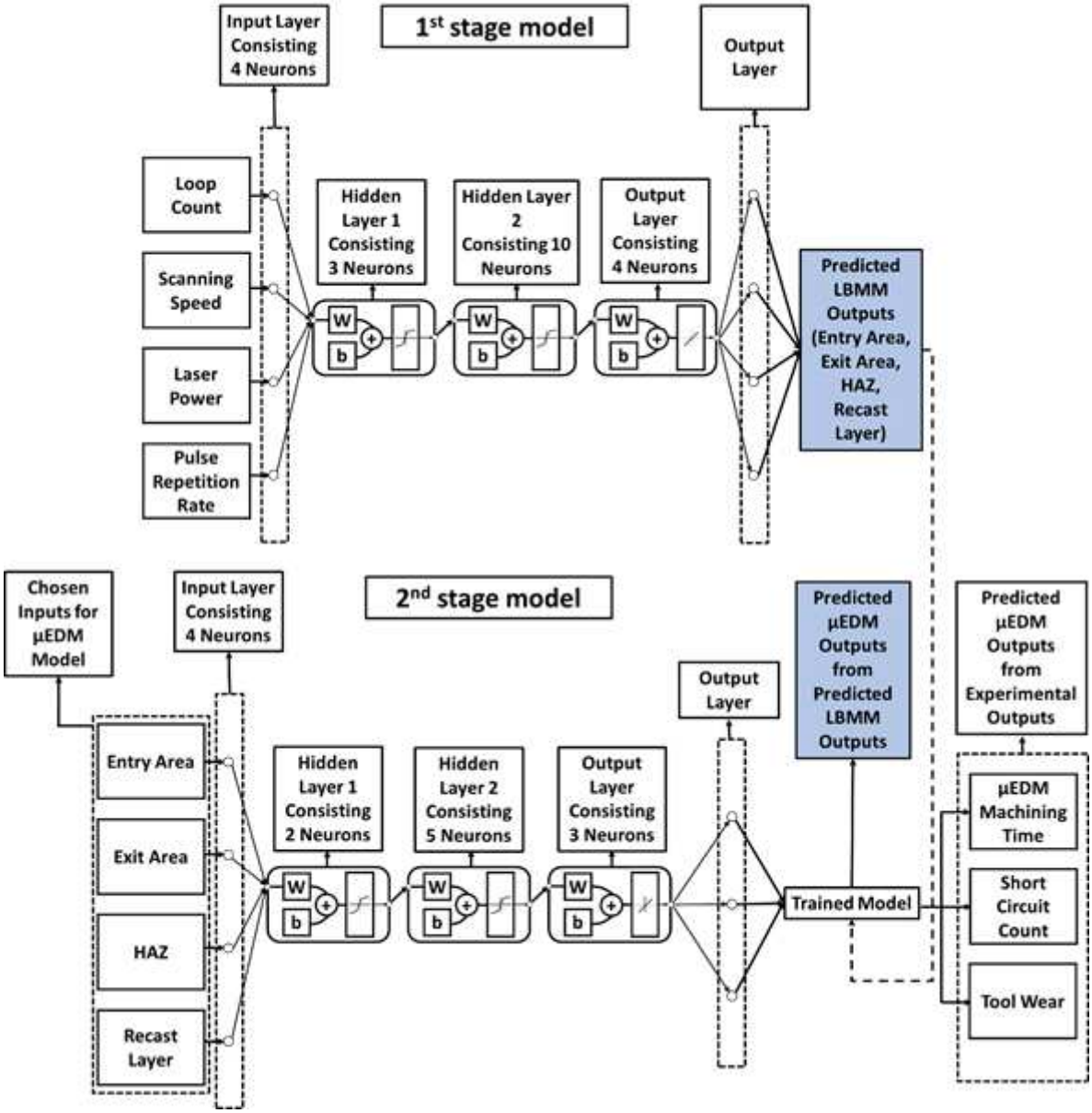

Figure 5

See the Manuscript Files section for the complete figure caption.

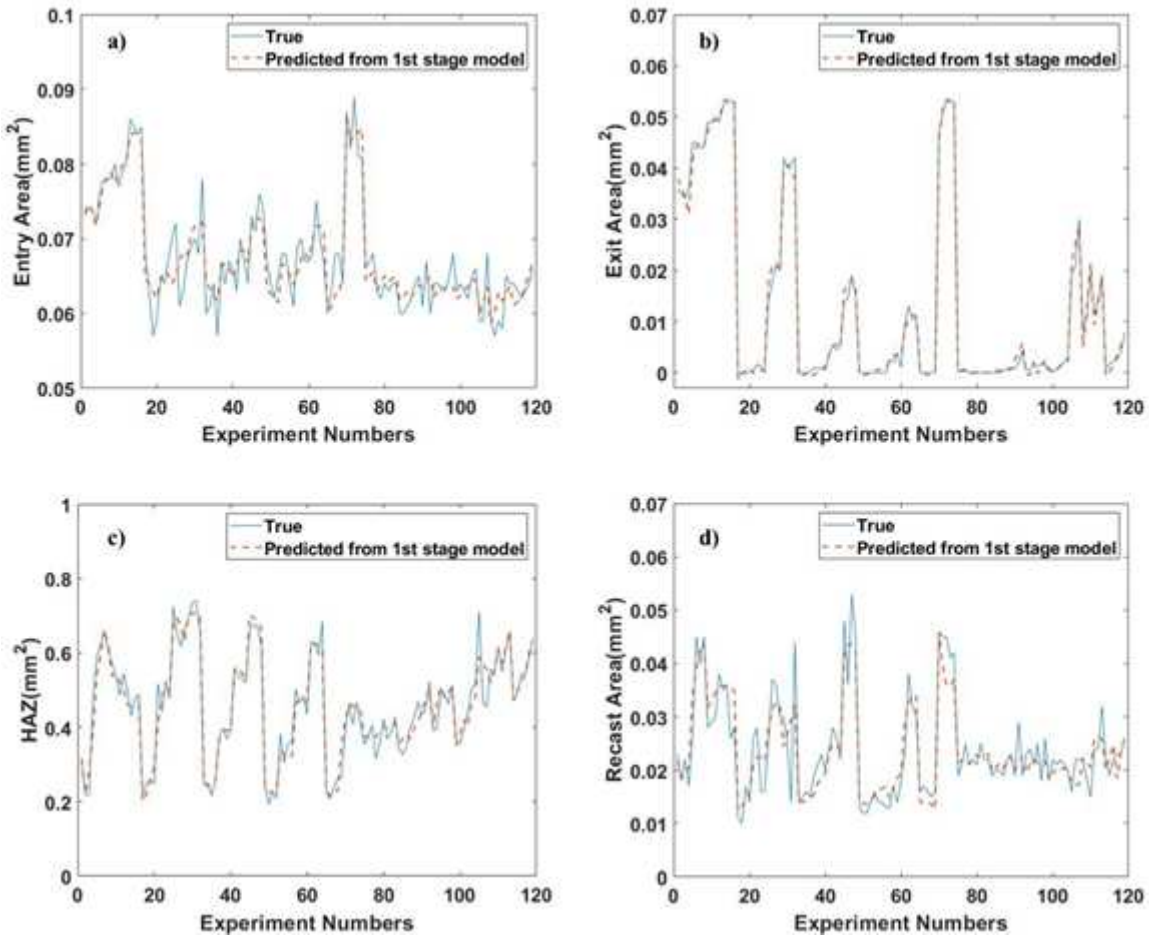

Figure 6

See the Manuscript Files section for the complete figure caption.

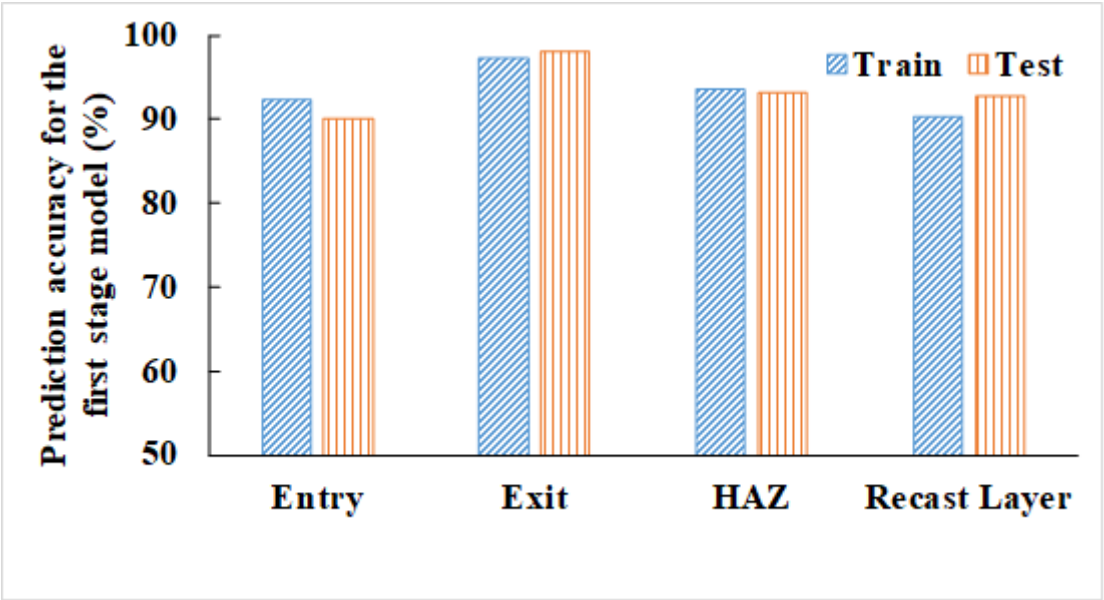

Figure 7

See the Manuscript Files section for the complete figure caption.

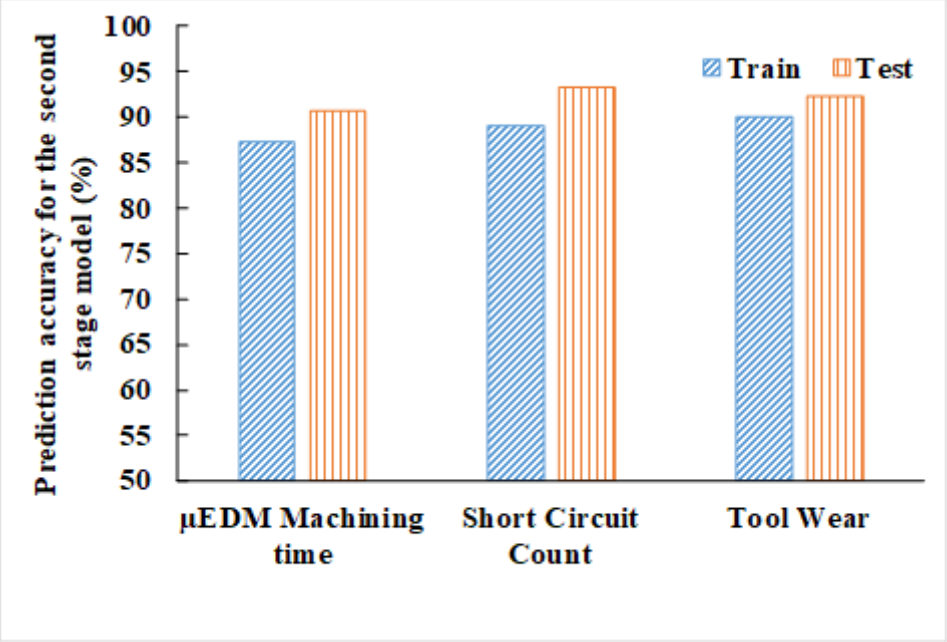

Figure 8

See the Manuscript Files section for the complete figure caption.

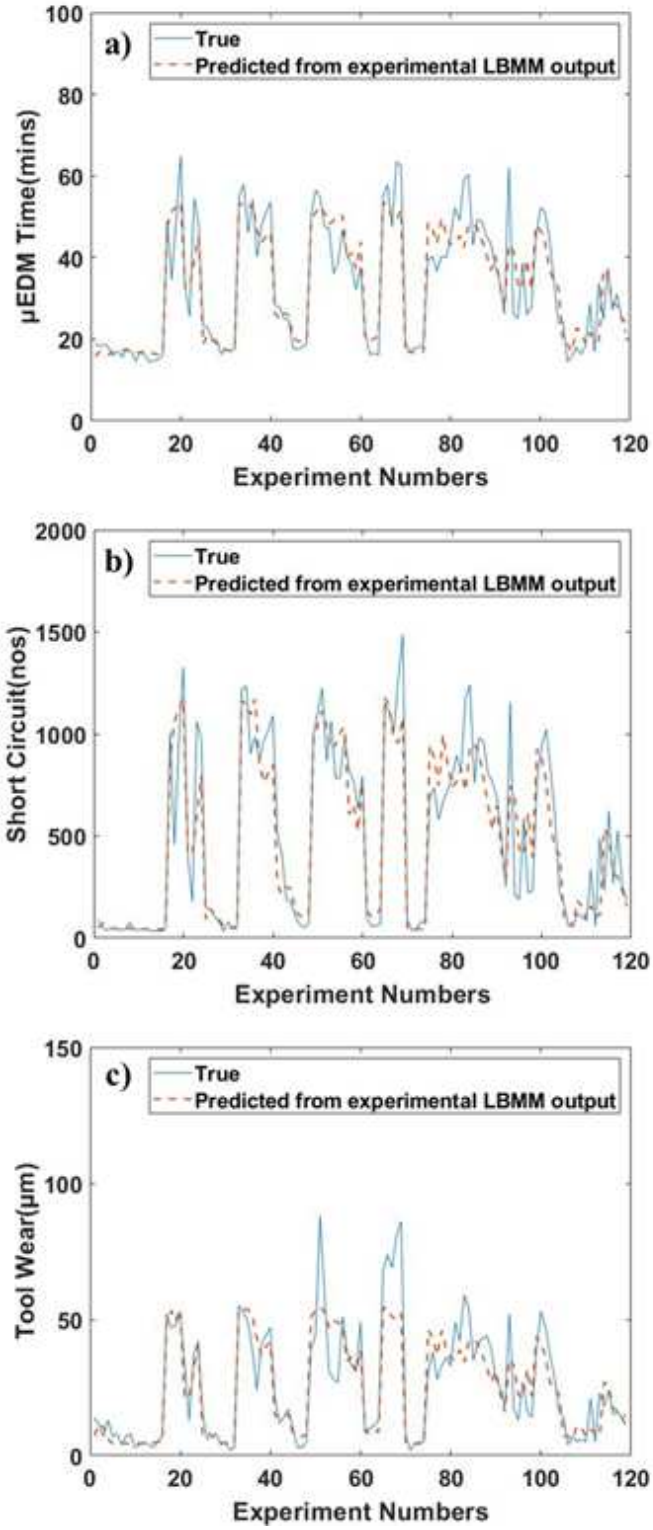

Figure 9

See the Manuscript Files section for the complete figure caption.

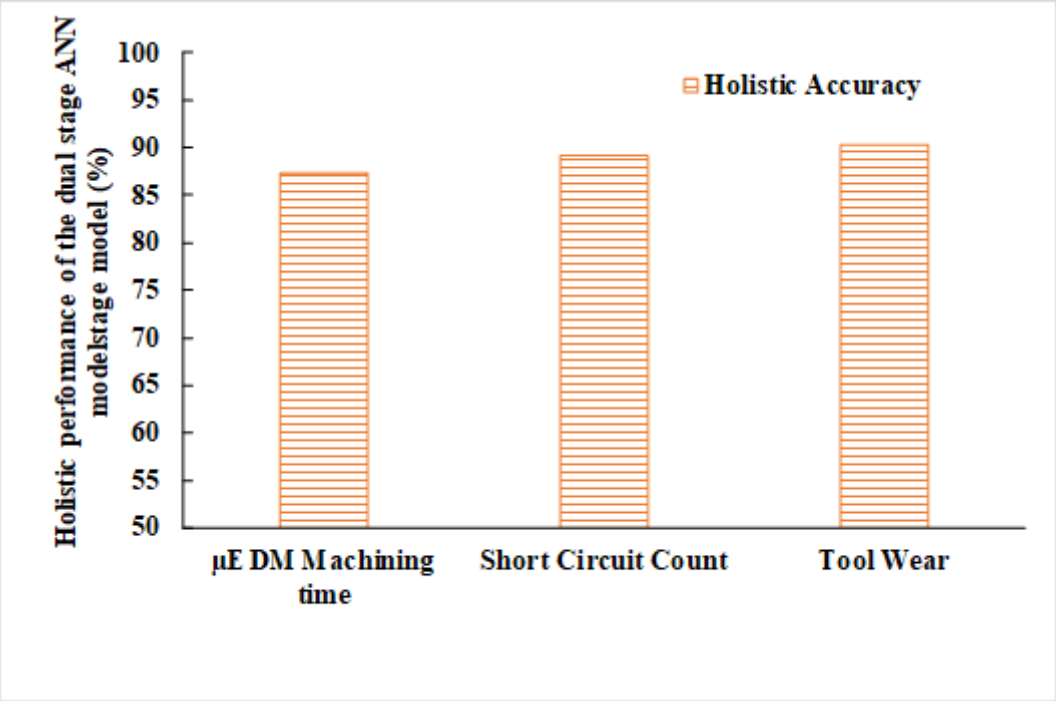

Figure 10

See the Manuscript Files section for the complete figure caption.

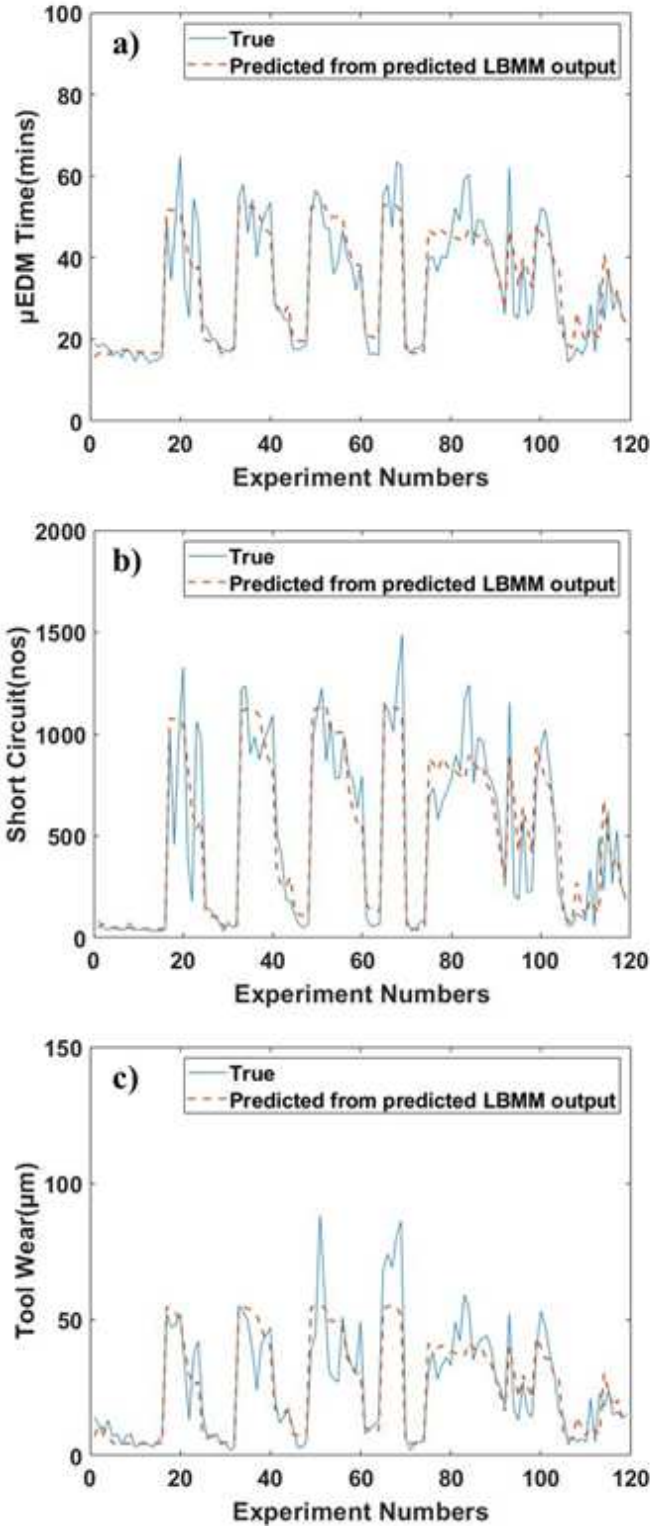

Figure 11

See the Manuscript Files section for the complete figure caption.

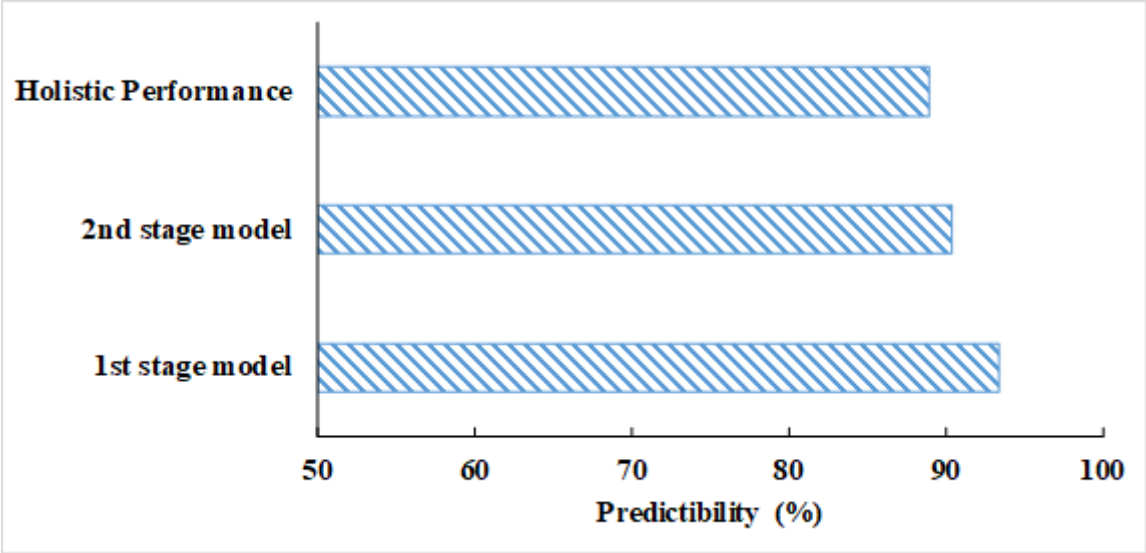

Figure 12

See the Manuscript Files section for the complete figure caption.

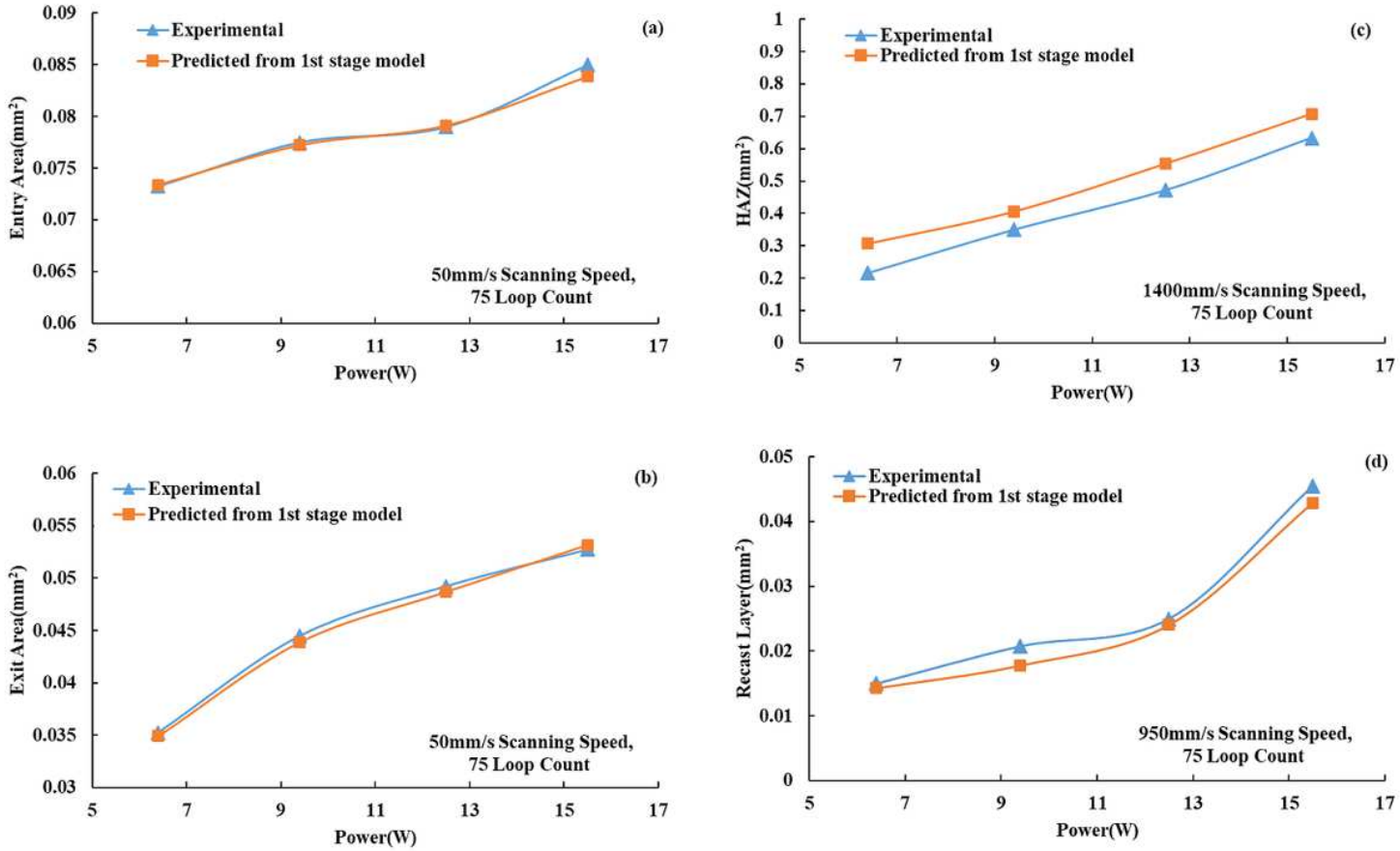

Figure 13

See the Manuscript Files section for the complete figure caption.

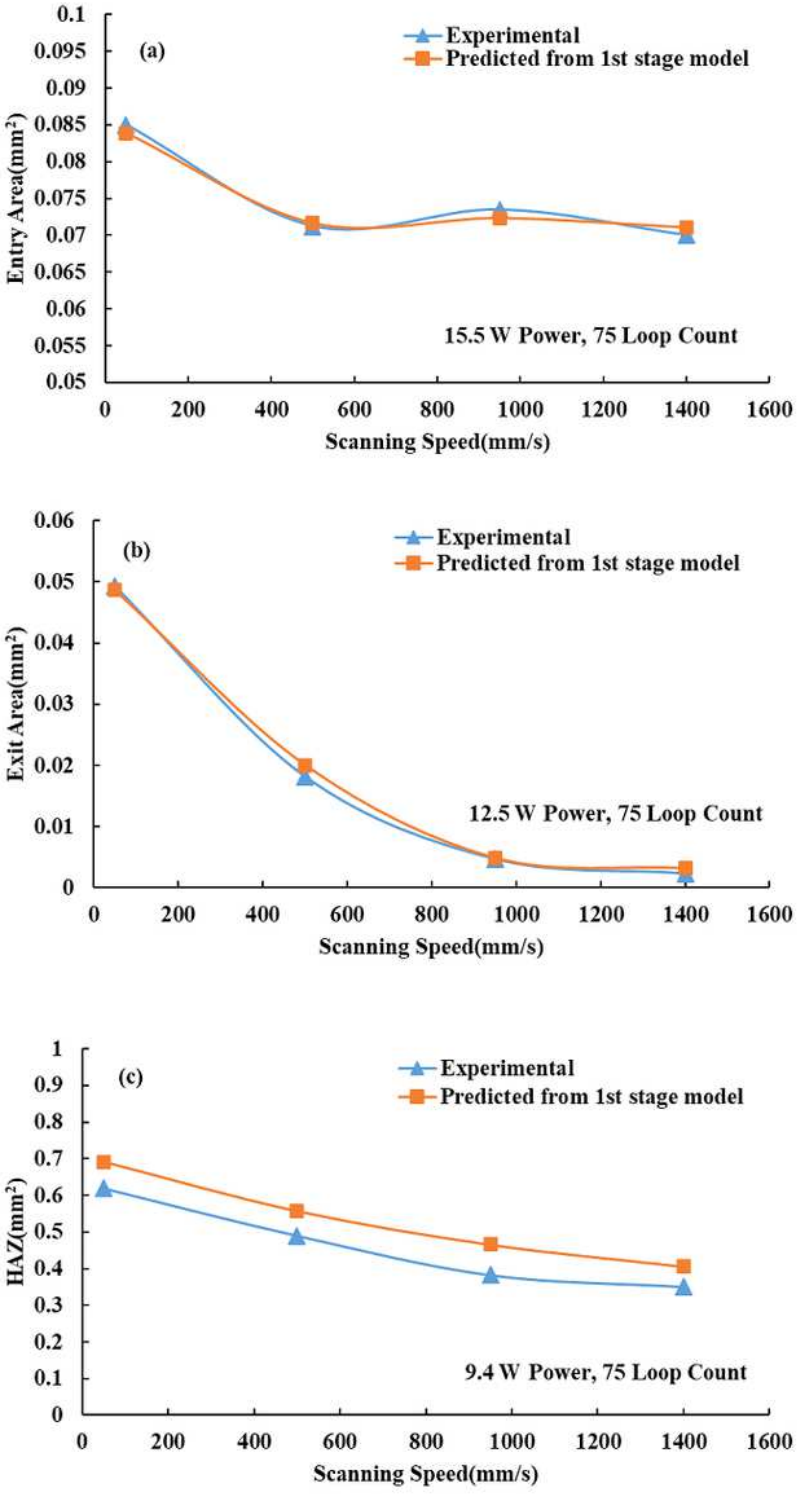

Figure 14

See the Manuscript Files section for the complete figure caption.

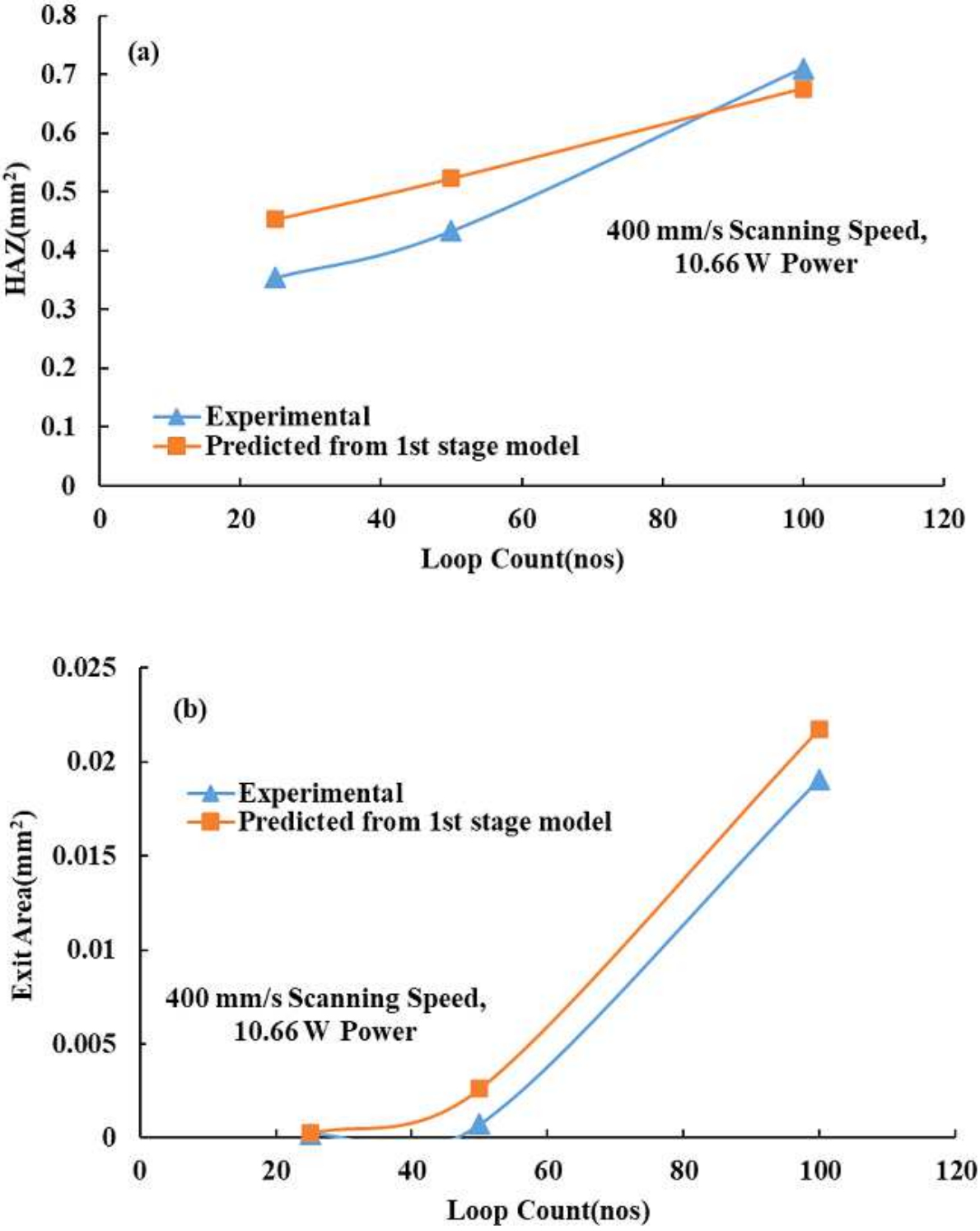

Figure 15

See the Manuscript Files section for the complete figure caption.

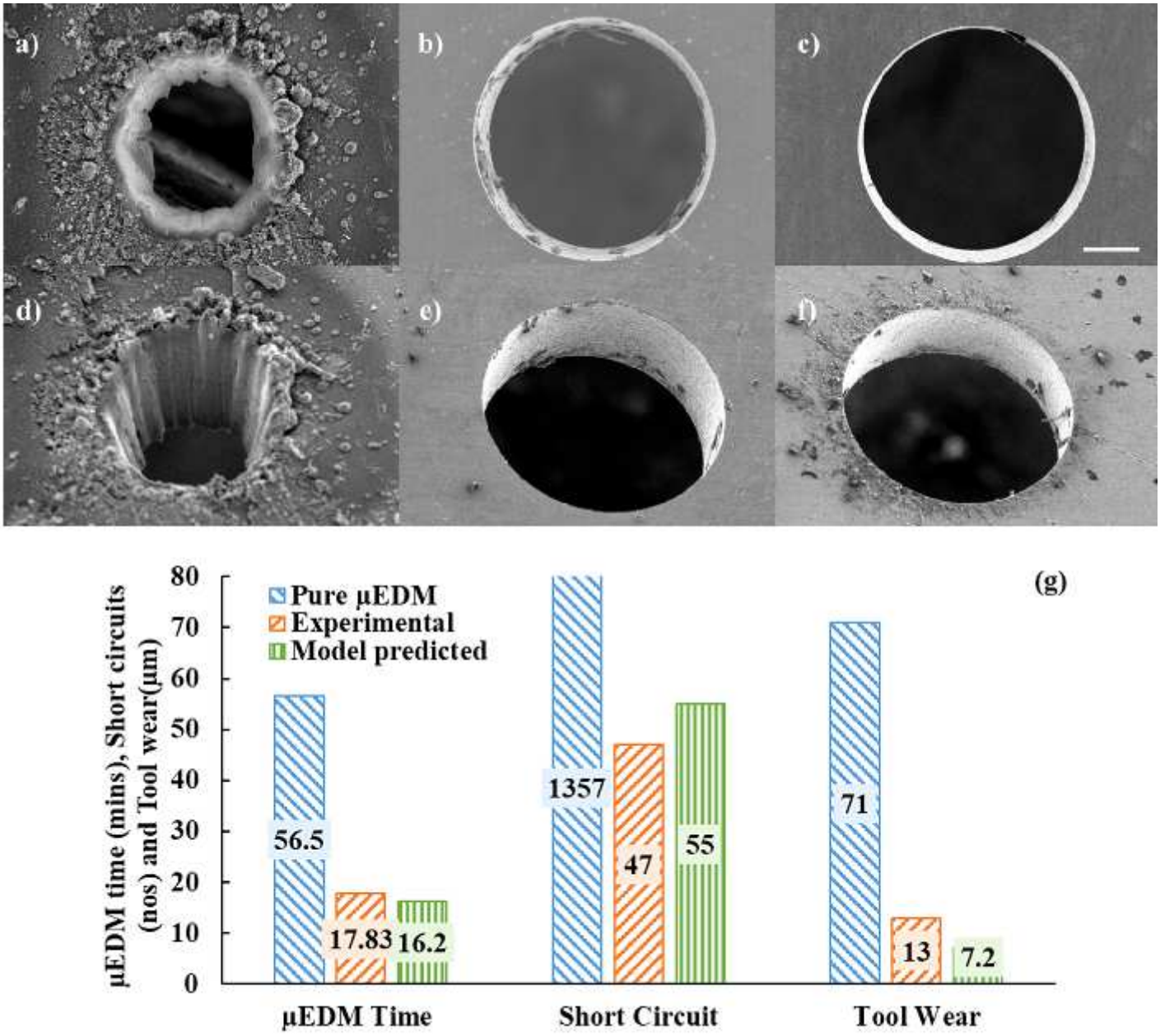

Figure 16

See the Manuscript Files section for the complete figure caption.

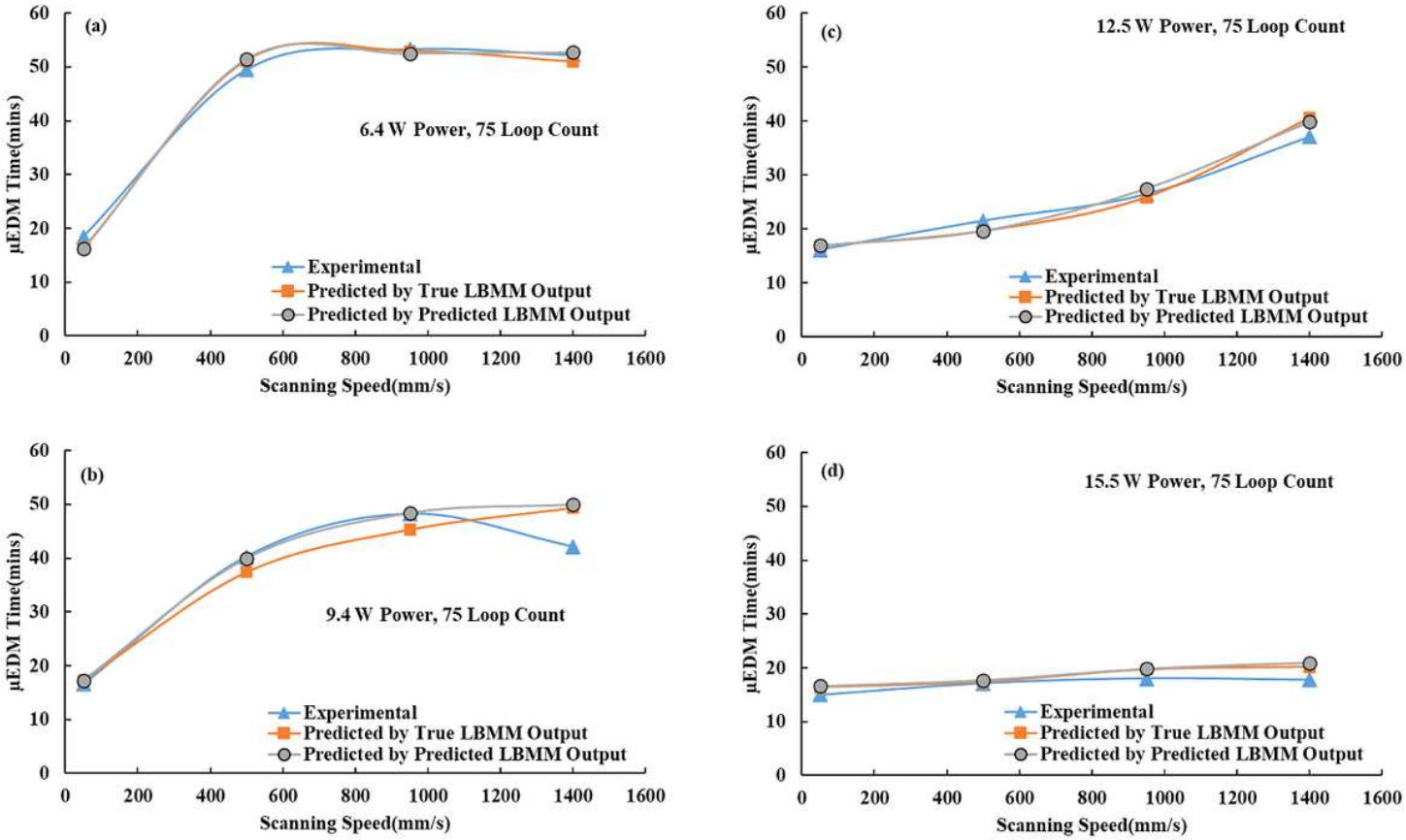

Figure 17

See the Manuscript Files section for the complete figure caption.

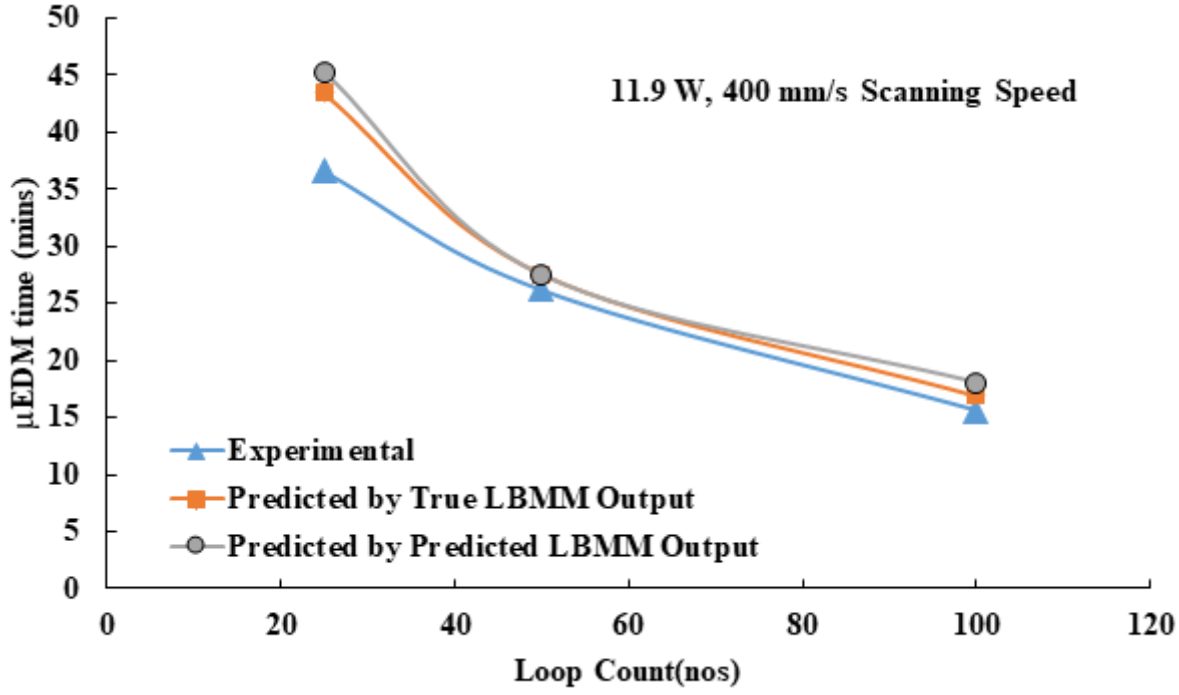

Figure 18

See the Manuscript Files section for the complete figure caption.

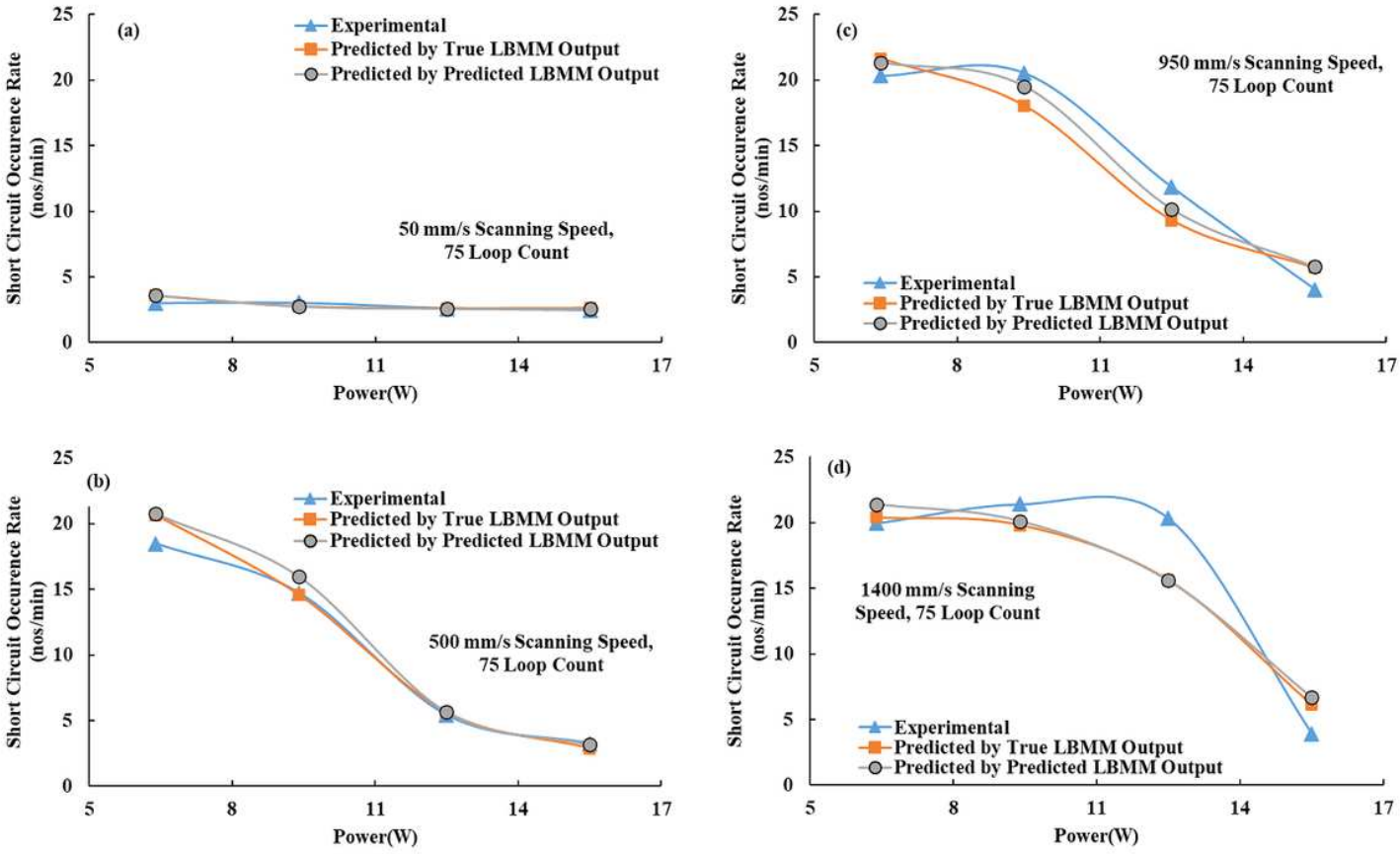

Figure 19

See the Manuscript Files section for the complete figure caption.

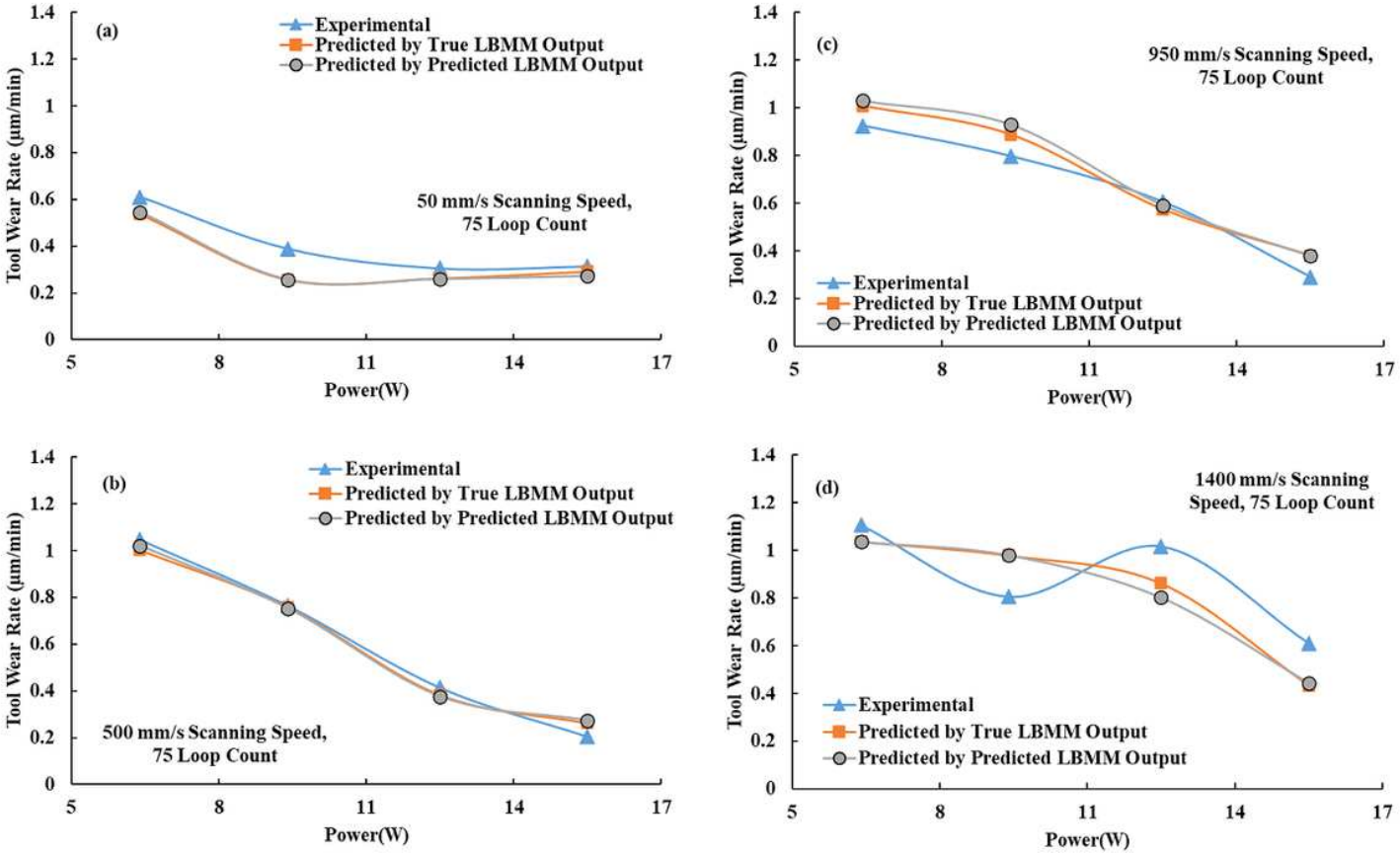

Figure 20

See the Manuscript Files section for the complete figure caption.

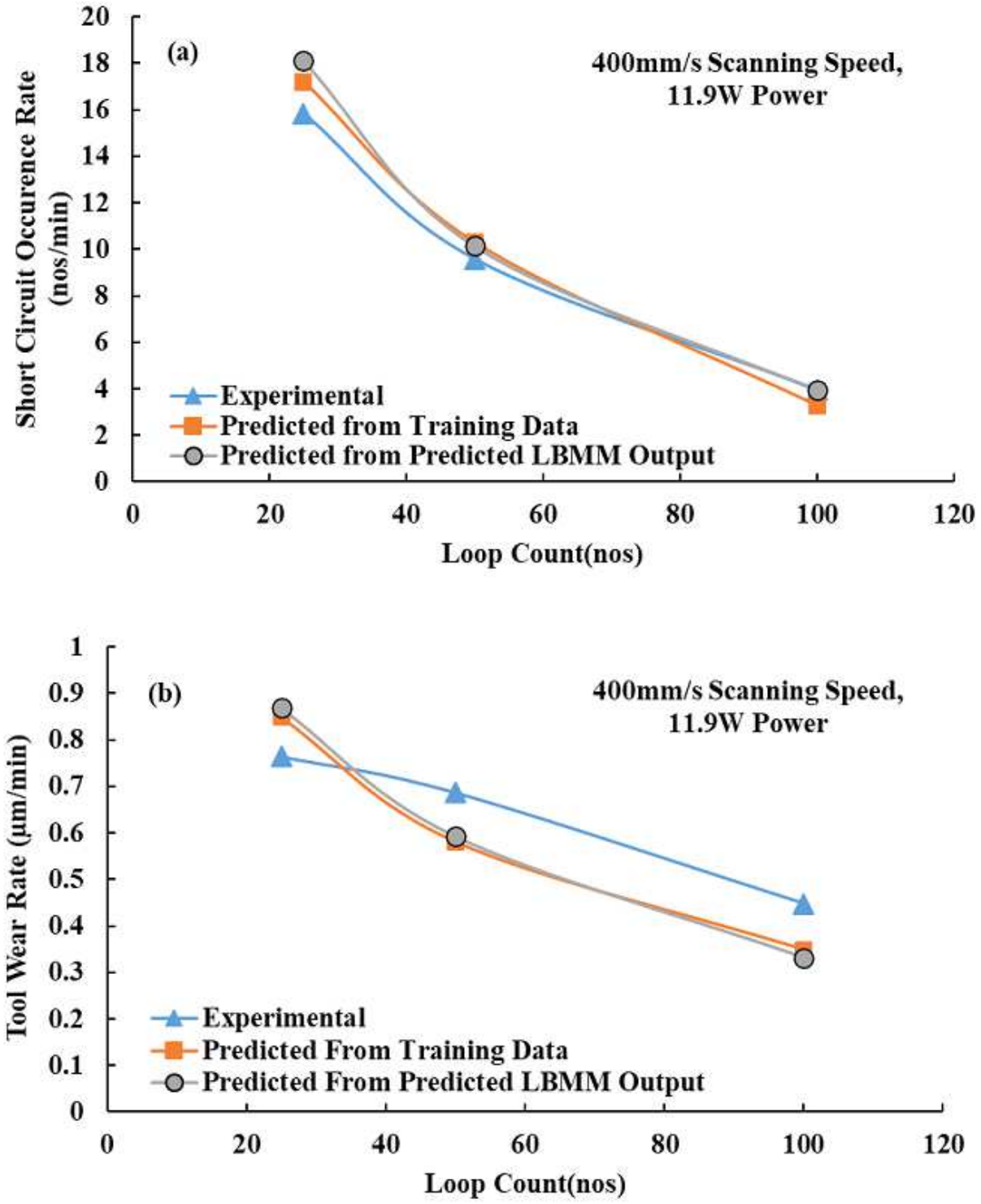

Figure 21

See the Manuscript Files section for the complete figure caption.

Supplementary Files

This is a list of supplementary files associated with this preprint. Click to download.

- Dataset1AIM.xlsx
- Dataset2AIM.xlsx
- Dataset3AIM.xlsx
- Dataset4AIM.xlsx
- Dataset5AIM.xlsx
- Dataset6AIM.xlsx